

1 LEVERAGING MULTI-MESSENGER ASTROPHYSICS FOR DARK MATTER SEARCHES

By

Daniel Nicholas Salazar-Gallegos

A DISSERTATION

Submitted to
Michigan State University
in partial fulfillment of the requirements
for the degree of

Physics—Doctor of Philosophy
Computational Mathematics in Science and Engineering—Dual Major

Today

ABSTRACT

3 I did Dark Matter with HAWC and IceCube. I also used Graph Neural Networks

⁴ Copyright by

⁵ DANIEL NICHOLAS SALAZAR-GALLEGOS

⁶ Today

ACKNOWLEDGMENTS

8 I love my friends. Thanks to everyone that helped me figure this out. Amazing thanks to the people
9 at LANL who supported me. Eames, etc Dinner Parties Jenny and her child Kaydince Kirsten, Pat,
10 Andrea Family. You're so far but so critical to my formation. Unconditional love. Roommate

TABLE OF CONTENTS

12	LIST OF TABLES	vii
13	LIST OF FIGURES	viii
14	LIST OF ABBREVIATIONS	xiv
15	CHAPTER 1 INTRODUCTION	1
16	CHAPTER 2 DARK MATTER IN THE COSMOS	2
17	2.1 Introduction	2
18	2.2 Dark Matter Basics	3
19	2.3 Evidence for Dark Matter	4
20	2.4 Searching for Dark Matter: Particle DM	11
21	2.5 Sources for Indirect Dark Matter Searches	16
22	2.6 Multi-Messenger Dark Matter	18
23	CHAPTER 3 MULTIMESSENGER ASTROPHYSICS: DETECTING HIGH EN-	
24	ERGY NEUTRAL MESSENGERS	21
25	3.1 Introduction	21
26	3.2 Charged Particles in a Medium	21
27	3.3 Photons (γ)	22
28	3.4 Neutrinos (ν)	22
29	3.5 Opportunities to Combine for Dark Matter	22
30	CHAPTER 4 HIGH ALTITUDE WATER CHERENKOV (HAWC) OBSERVATORY .	24
31	4.1 The Detector	24
32	4.2 Events Reconstruction and Data Acquisition	24
33	4.3 Remote Monitoring	24
34	CHAPTER 5 ICECUBE NEUTRINO OBSERVATORY	25
35	5.1 The Detector	25
36	5.2 Events Reconstruction and Data Acquisition	25
37	5.3 Northern Test Site	25
38	CHAPTER 6 GLORY DUCK: MULTI-WAVELENGTH SEARCH FOR DARK MATT-	
39	TER ANNIHILATION TOWARDS DWARF SPHEROIDAL GALAX-	
40	IES	26
41	6.1 Introduction	26
42	6.2 Dataset and Background	28
43	6.3 Analysis	29
44	6.4 Likelihood Methods	34
45	6.5 HAWC Results	40
46	6.6 Glory Duck Combined Results	43
47	6.7 HAWC Systematics	48

48	6.8 <i>J</i> -factor distributions	49
49	6.9 Discussion and Conclusions	55
50	CHAPTER 7 MULTITHREADING HAWC ANALYSES FOR DARK MATTER	
51	SEARCHES	59
52	7.1 Introduction	59
53	7.2 Dataset and Background	59
54	7.3 Analysis	60
55	7.4 Likelihood Methods	65
56	CHAPTER 8 HEAVY DARK MATTER ANNIHILATION SEARCH WITH ICE-CUBE'S NORTH SKY TRACK DATA	66
58	CHAPTER 9 NU DUCK	67
59	APPENDIX A MULTI-EXPERIMENT SUPPLEMENTARY FIGURES	68
60	APPENDIX B MULTITHREADING SUPPLEMENTARY FIGURES	69
61	BIBLIOGRAPHY	70

LIST OF TABLES

<p>63 Table 6.1 Summary of the relevant properties of the dSphs used in the present work. 64 Column 1 lists the dSphs. Columns 2 and 3 present their heliocentric distance 65 and galactic coordinates, respectively. Columns 4 and 5 report the J-factors of 66 each source given from the \mathcal{GS} and \mathcal{B} independent studies and their estimated 67 $\pm 1\sigma$ uncertainties. The values $\log_{10} J$ (\mathcal{GS} set) [45] correspond to the mean 68 J-factor values for a source extension truncated at the outermost observed star. 69 The values $\log_{10} J$ (\mathcal{B} set) [47] are provided for a source extension at the tidal 70 radius of each dSph. Bolded sources are within HAWC's field of view and 71 provided to the Glory Duck analysis.</p> 34
<p>72 Table 6.2 Summary of dSph observations by each experiment used in this work. A 73 ‘-’ indicates the experiment did not observe the dSph for this study. For 74 Fermi-LAT, the exposure at 1 GeV is given. For HAWC, $\Delta\theta$ is the absolute 75 difference between the source declination and HAWC latitude. HAWC is more 76 sensitive to sources with smaller $\Delta\theta$. For IACTs, we show the zenith angle 77 range, the total exposure, the energy range, the angular radius θ of the signal or 78 ON region, the ratio of exposures between the background-control (OFF) and 79 signal (ON) regions (τ), and the significance of gamma-ray excess in standard 80 deviations, σ.</p> 35
<p>81 Table 7.1 Summary of the relevant properties of the dSphs used in the present work. 82 Column 1 lists the dSphs. Columns 2 and 3 present their heliocentric distance 83 and galactic coordinates, respectively. Columns 4 reports the J-factors of 84 each source given from the \mathcal{LS} studies and estimated $\pm 1\sigma$ uncertainties. The 85 values $\log_{10} J$ (\mathcal{LS} set) [65] correspond to the mean J-factor values for a 86 source extension truncated at 0.5°.</p> 63
<p>87 Proof I know how to include</p>	

LIST OF FIGURES

89	Figure 2.1	Rotation curve fit to NGC 6503 from [7]. Dashed line is the contribution 90 from visible matter. Dotted curves are from gas. Dash-dot curves are from 91 dark matter (DM). Solid line is the composite contribution from all matter 92 and DM sources. Data are indicated with bold dots with error bars. Data 93 agree strongly with a matter + DM composite prediction.	5
94	Figure 2.2	Light from distant galaxy is bent in unique ways depending on the distribution 95 of mass between the galaxy and Earth. Yellow dashed lines indicate where 96 the light would have gone if the matter were not present [8].	7
97	Figure 2.3	(left) Optical image of galactic cluster 1E0657-558. (right) X-ray image of the 98 cluster with redder meaning hotter and higher baryon density. (both) Green 99 contours are reconstruction of gravity contours from weak lensing. White 100 rings are the best fit mass maxima at 68.3%, 95.5%, and 99.7% confidence. 101 The matter maxima of the clusters are clearly separated from x-ray maxima. [9]	8
102	Figure 2.4	Plank CMB sky. Sky map features small variations in temperature in primor- 103 dial light. These anisotropies are used to make inferences about the universe's 104 energy budget and developmental history. [10]	9
105	Figure 2.5	Observed Cosmic Microwave Background power spectrum as a function of 106 multipole moment from Plank [10]. Blue line is best fit model from Λ CDM. 107 Red points and lines are data and error, respectively.	10
108	Figure 2.6	Predicted power spectra of CMB for different $\Omega_m h^2$ values for fixed baryon 109 density from [11]. (left) Low $\Omega_m h^2$ increases the prominence of first and 110 second peaks. (middle) $\Omega_m h^2$ is most similar to the observed power spectrum. 111 The second and third peaks are similar in height. (right) $\Omega_m h^2$ is large which 112 suppresses the first peak and raises the prominence of the third peak.	10
113	Figure 2.7	The Standard Model (SM) of particle physics. Figure taken from http://www.quantumdiaries.org/2014/03/14/the-standard-model-a-beautiful-but-flawed-theory/	12
116	Figure 2.8	Simplified Feynman diagram demonstrating with different ways DM can 117 interact with SM particles. The 'X's refer to the DM particles whereas the 118 SM refer to fundamental particles in the SM. The large circle in the center 119 indicates the vertex of interaction and is purposely left vague. The colored 120 arrows refer to different directions of time as well as their respective labels. 121 The arrows indicate the initial and final state of the DM -SM interaction in time.	13

122	Figure 2.9 A single jet event in ATLAS detector from 2017 [16]. Jet momentum was 123 observed to be 1.9 TeV. Missing transverse momentum was observed to be 124 1.9 TeV compared to the initial transverse momentum of the event was 0. 125 Implied MET is traced by a red dashed line in event display.	14
126	Figure 2.10 More detailed pseudo-Feynman diagram of particle cascade from dark matter 127 annihilation into 2 quarks. The quarks hadronize and down to stable particles 128 like γ or the anti-proton (p^-). Diagram pulled from ICRC 2021 presentation 129 on DM annihilation search [17].	15
130	Figure 2.11 Dark Matter (DM) decay spectrum for $b\bar{b}$ initial state and γ final state. Redder 131 spectra are for larger DM masses. Bluer spectra are light DM masses. x is a 132 unitless factor defined as the ratio of the mass of DM, m_χ , and the final state 133 particle energy E_γ . Figure from [19].	17
134	Figure 2.12 Different dark matter density profiles compared. Some models produce ex- 135 ceptionally large densities at small r [20].	18
136	Figure 2.13 The Milky Way Galaxy in photons (γ) and neutrinos (ν) [22]. The Galactic 137 center is at $l=0^\circ$ and is the brightest region in all panels. (top) An Optical 138 color image of the Milky Way galaxy seen from Earth. Clouds of gas and dust 139 obscure some light from stars. (2nd down) Integrated flux of γ -rays observed 140 by the Fermi-LAT telescope [23]. (middle) Expected neutrino emission 141 that corresponds with Fermi-LAT observations. (2nd up) Expected neutrino 142 emission profile after considering detector systematics of IceCube. (bottom) 143 Observed neutrino emission from region of the galactic plane. Substantial 144 neutrino emission was detected.	19
145	Figure 2.14 Dark Matter annihilation spectra for different final state particle and standard 146 model annihilation channels [24]. Photons (red), e^\pm (green), \bar{p} (blue), ν (black).	20
147	Figure 3.1 TODO: Show a nuclear reactor with cherenkov radiation[NEEDS A SOURCE][FACT 148 CHECK THIS]	22
149	Figure 3.2 TODO: absorption spectrum of liquid and solid water[NEEDS A SOURCE][FACT 150 CHECK THIS]	23

151	Figure 6.1	Sensitivities of five gamma-ray experiments compared to percentages of the 152 Crab nebula's emission and dark matter annihilation. Solid lines present 153 estimated sensitivities to power law spectra [FACT CHECK THIS]for each 154 experiment. Green lines are Fermi-LAT sensitivities where lighter green is 155 the sensitivity to the galactic center and dark green is its sensitivity to higher 156 declinations. Orange, red, and purple solid lines represent the MAGIC, HESS, 157 and VERITAS 50 hour sensitivities respectively. The maroon and brown lines 158 are the HAWC 1 year and 5 year sensitivities. Across four decades of gamma- 159 ray energy, these experiments have similar sensitivities on the order 10^{-12} 160 erg cm $^{-2}$ s $^{-1}$. The dotted lines are estimated dark matter fluxes assuming 161 $m_\chi = 5$ TeV DM annihilating to bottom quarks (red), tau leptons (blue), 162 and W bosons (green). Faded gray lines outline percentage flux of the Crab 163 nebula. Figure is an augmented version of [25]	27
164	Figure 6.2	Effect of Electroweak (EW) corrections on expected DM annihilation spec- 165 trum for $\chi\chi \rightarrow W^-W^+$. Solid lines are spectral models that consider EW 166 corrections. Dash-dot lines are spectral models without EW corrections. Red 167 lines are models for $M_\chi = 1$ TeV. Blue lines represent models for $M_\chi = 100$ 168 TeV. All models are sourced from the PPPC4DMID [44].	31
169	Figure 6.3	$\frac{dJ}{d\Omega}$ maps for Segue1 (top) and Coma Berenices (bottom). Origin is centered 170 on the specific dwarf spheroidal galaxies (dSph). X and Y axes are the 171 angular separation from the center of the dwarf. Plots of the remaining 11 172 dSph HAWC studied are linked in Fig. A.1.	33
173	Figure 6.4	Illustration of the combination technique showing a comparison between 174 $-2 \ln \lambda$ provided by four instruments (colored lines) from the observation 175 of the same dSph without any J nuisance and their sum, <i>i.e.</i> the resulting 176 combined likelihood (thin black line). According to the test statistics of 177 Equation (6.6), the intersection of the likelihood profiles with the line $-2 \ln \lambda$ 178 = 2.71 indicates the 95% C.L. upper limit on $\langle \sigma v \rangle$. The combined likelihood 179 (thin black line) shows a smaller value of upper limit on $\langle \sigma v \rangle$ than those 180 derived by individual instruments. We also show how the uncertainties on 181 the J factor effects the combined likelihood and degrade the upper limit on 182 $\langle \sigma v \rangle$ (thick black line). All likelihood profiles are normalized so that the global 183 minimum $\widehat{\langle \sigma v \rangle}$ is 0. We note that each profile depends on the observational 184 conditions in which a target object was observed. The sensitivity of a given 185 instrument can be degraded and the upper limits less constraining if the 186 observations are performed in non-optimal conditions such as a high zenith 187 angle or a short exposure time.	38
188	Figure 6.5	HAWC upper limits at 95% confidence level on $\langle \sigma v \rangle$ versus DM mass for 189 seven annihilation channels, using the set of J -factors from Ref. [53] The 190 solid line represents the observed combined limit. Dashed lines represent 191 limits from individual dSphs.	41

192	Figure 6.6 HAWC TS values for best fit $\langle\sigma v\rangle$ versus m_χ for seven SM annihilation channels with J factors from \mathcal{GS} . The solid black line shows the combined best fit TS values. The colored, dashed lines are the TS values for each of the 13 sources HAWC studied.	42
196	Figure 6.7 HAWC Brazil bands at 95% confidence level on $\langle\sigma v\rangle$ versus DM mass for seven annihilation channels with J -factors from \mathcal{GS} [53]. The solid line represents the combined limit from 13 dSphs. The dashed line is the expected limit. The green band is the 68% containment. The yellow band is the 95% containment.	43
201	Figure 6.8 Upper limits at 95% confidence level on $\langle\sigma v\rangle$ in function of the DM mass for eight annihilation channels, using the set of J factors from Ref. [53] (\mathcal{GS} set in Table 6.1). The black solid line represents the observed combined limit, the black dashed line is the median of the null hypothesis corresponding to the expected limit, while the green and yellow bands show the 68% and 95% containment bands. Combined upper limits for each individual detector are also indicated as solid, colored lines. The value of the thermal relic cross-section in function of the DM mass is given as the red dotted-dashed line [54].	44
210	Figure 6.9 Same as Fig. 6.8, using the set of J factors from Ref. [47, 55] (\mathcal{B} set in Table 6.1).	45
211	Figure 6.10 Comparisons of the combined limits at 95% confidence level for each of the eight annihilation channels when using the J factors from Ref. [53] (\mathcal{GS} set in Table 6.1), plain lines, and the J factor from Ref. [47, 55] (\mathcal{B} set in Table 6.1), dashed lines. The cross-section given by the thermal relic is also indicated [54].	47
215	Figure 6.11 Comparisons of the combined limits at 95% confidence level for a point source analysis and extended source using [53] \mathcal{GS} J-factor distributions and PPPC [44] annihilation spectra. Shown are the limits for Segue1 which will have the most significant impact on the combined limit. 6 of the 7 DM annihilation channels are shown. Solid lines are extended source studies. Dashed lines are point source studies. Overall, the extended source analysis improves the limit by a factor of 2.	49
222	Figure 6.12 Same as Fig. 6.11 on Coma Berenices. This dSph also contributes significantly to the limit. The limits are identical in this case.	50
224	Figure 6.13 Comparison of combined limits when correcting for HAWC's pointing systematic. All DM annihilation channels are shown. The solid black line is the ratio between published limit to the declination corrected limit. The blue solid line or "Combined_og" represented the limits computed for Glory Duck. The solid orange line or "Combined_ad" represented the limits computed after correcting for the pointing systematic.	51

230	Figure 6.14 Differential map of dJ/Ω from model built in Section 6.8.1 and profiles provided directly from authors. (Top) Differential from Segue1. (bottom) Differential from Coma Berenices. Note that their scales are not the same. Segue1 shows the deepest discrepancies which is congruent with its large uncertainties. Both models show anuli where unique models become apparent.	52
235	Figure 6.15 HAWC limits for Coma Berenices (top) and Segue1 (bottom) for two different map sets. Blue lines are limits calculated on maps with poor model representation. Orange lines are limits calculated on spatial profiles provided by the authors of [45]. Black line is the ratio of the poor spatial model limits to the corrected spatial models. The left y-axis measures $\langle\sigma v\rangle$ for the blue and orange lines. The right y-axis measures the ratio and is unitless.	53
241	Figure 6.16 Comparisons between the J -factors versus the angular radius for the computation of J factors from Ref. [53] (\mathcal{GS} set in Table 6.1) in blue and for the computation from Ref. [47, 55] (\mathcal{B} set in Tab. 6.1) in orange. The solid lines represent the central value of the J -factors while the shaded regions correspond to the 1σ standard deviation.	56
246	Figure 6.17 Comparisons between the J -factors versus the angular radius for the computation of J factors from Ref. [53] (\mathcal{GS} set in Tab. 6.1) in blue and for the computation from Ref. [47, 55] (\mathcal{B} set in Tab. 6.1) in orange. The solid lines represent the central value of the J -factors while the shaded regions correspond to the 1σ standard deviation.	57
251	Figure 7.1 Difference between spectral hypotheses from PPPC [44] and HDM [64]. Shown is the expected DM annihilation spectrum for $\chi\chi \rightarrow W^-W^+$. Solid lines are spectral models with EW corrections from the PPPC. Dash-dot lines are spectral models from HDM. Red lines are models for $M_\chi = 1$ TeV. Blue lines represent models for $M_\chi = 100$ TeV.	62
256	Figure 7.2 Photon spectra for $\chi\chi \rightarrow \gamma\gamma$ (left) and $\chi\chi \rightarrow ZZ$ (right) after gaussian convolution of line features. Both spectra have δ -features at photon energies equal to the DM mass. Bluer lines are annihilation spectra with lower DM mass. Redder lines are spectra from larger DM mass. All Spectral models are sourced from the Heavy Dark Matter models [64].	63
261	Figure 7.3 $\frac{dJ}{d\Omega}$ maps for Coma Berenices, Draco, Segue1, and Sextans. Columns are divided for the $\pm 1\sigma$ uncertainties in $dJ/d\Omega$ around the median value from \mathcal{LS} [65]. Origin is centered on the specific dwarf spheroidal galaxies (dSph). θ and ϕ axes are the angular separation from the center of the dwarf. Axes are drawn roughly according to the energy sensitivity of HAWC.	64
266	Figure A.1 Sister figure to Figure 6.3. Sources in the first row from left to right: Bootes I, Canes Venatici I, II. In second row: Draco, Hercules, Leo I. In the first row: Leo II, Leo IV, Sextans. In the final row: Ursa Major I, Ursa Major II.	68

LIST OF ABBREVIATIONS

- 274 **MSU** Michigan State University
275 **LANL** Los Alamos National Laboratory
276 **DM** Dark Matter
277 **SM** Standard Model
278 **HAWC** High Altitude Water Cherenkov Observatory

279

CHAPTER 1

INTRODUCTION

280 Is the text not rendering right? Ah ok it knows im basically drafting the doc still

CHAPTER 2

281

DARK MATTER IN THE COSMOS

282 **2.1 Introduction**

283 The dark matter problem can be summarized in part by the following thought experiment.

284 Let us say you are the teacher for an elementary school classroom. You take them on a field
285 trip to your local science museum and among the exhibits is one for mass and weight. The exhibit
286 has a gigantic scale, and you come up with a fun problem for your class.

287 You ask your class, "What is the total weight of the classroom? Give your best estimation to
288 me in 30 minutes, and then we'll check your guess on the scale. If your guess is within 10% of the
289 right answer, we will stop for ice cream on the way back."

290 The students are ecstatic to hear this, and they get to work. The solution is some variation of
291 the following strategy. The students should give each other their weight or best guess if they do
292 not know. Then, all they must do is add each student's weight and get a grand total for the class.
293 The measurement on the giant scale should show the true weight of the class. When comparing
294 the measured weight to your estimation, multiply the measurement by 1.0 ± 0.1 to get the $\pm 10\%$
295 tolerances for your estimation.

296 Two of your students, Sandra and Mario, return to you with a solution.

297 They say, "We weren't sure of everyone's weight. We used 65 lbs. for the people we didn't
298 know and added everyone who does know. There are 30 of us, and we got 2,000 lbs.! That's a ton!"

299 You estimated 1,900 lbs. assuming the average weight of a student in your class was 60 lbs.
300 So, you are pleased with Sandra's and Mario's answer. You instruct your students to all gather on
301 the giant scale and read off the weight together. To all your surprise, the scale reads *10,000 lbs.*!
302 10,000 is significantly more than a 10% error from 2,000. In fact, it is approximately 5 times more
303 massive than either your or your students' estimates. You think to yourself and conclude there
304 must be something wrong with the scale. You ask an employee to check the scale and verify it is
305 well calibrated. They confirm that the scale is in working order. You weigh a couple of students
306 individually to assess that the scale is well calibrated. Sandra weighs 59 lbs., and Mario weighs

307 62 lbs., typical weights for their age. You then weigh each student individually and see that their
308 weights individually do not deviate greatly from 60 lbs. So, where does all the extra weight come
309 from?

310 This thought experiment serves as an analogy to the Dark Matter problem. The important
311 substitution to make however is to replace the students with stars and the classroom with a galaxy,
312 say the Milky Way. Individually the mass of stars is well measured and defined with the Sun as our
313 nearest test case. However, when we set out to measure the mass of a collection of stars as large as
314 galaxies, our well-motivated estimation is wildly incorrect. There simply is no way to account for
315 this discrepancy except without some unseen, or dark, contribution to mass and matter in galaxies.
316 I set out in my thesis to narrow the possibilities of what this Dark Matter could be.

317 This chapter is organized like the following... **TODO: Text should look like ... Chapter x has**
318 **blah blah blah.**

319 2.2 Dark Matter Basics

320 Presently, a more compelling theory of cosmology that includes Dark Matter (DM) in order
321 to explain a variety of observations is Λ Cold Dark Matter, or Λ CDM. I present the evidence
322 supporting Λ CDM in Section 2.3 yet discuss the conclusions of the Λ CDM model here. According
323 to Λ CDM fit to observations on the Cosmic Microwave Background (CMB), DM is 26.8% of the
324 universe's current energy budget. Baryonic matter, stuff like atoms, gas, and stars, contributes to
325 4.9% of the universe's current energy budget [1, 2, 3].

326 DM is dark; it does not interact readily with light at any wavelength. DM also does not interact
327 noticeably with the other standard model forces (Strong and Weak) at a rate that is readily observed
328 [3]. DM is cold, which is to say that the average velocity of DM is below relativistic speeds [1].
329 'Hot' DM would not likely manifest the dense structures we observe like galaxies, and instead
330 would produce much more diffuse galaxies than what is observed [3, 1]. DM is old; it played a
331 critical role in the formation of the universe and the structures within it [1, 2].

332 Observations of DM have so far been only gravitational. The parameter space available to what
333 DM could be therefore is extremely broad. The broad DM parameter space is iteratively tested in

334 DM searches by supposing a hypothesis that has not yet been ruled out and performing observations
335 to test them. When the observations yield a null result, the parameter space is constrained further.
336 I present some approaches for DM searches in Section 2.4.

337 **2.3 Evidence for Dark Matter**

338 Dark Matter (DM) has been a looming problem in physics for almost 100 years. Anomalies
339 have been observed by astrophysicists in galactic dynamics as early as 1933 when Fritz Zwicky
340 noticed unusually large velocity dispersion in the Coma cluster. Zwicky's measurement was the
341 first recorded to use the Virial theorem to measure the mass fraction of visible and invisible matter
342 in celestial bodies [4]. From Zwicky in [5], "*If this would be confirmed, we would get the surprising*
343 *result that dark matter is present in much greater amount than luminous matter.*" Zwicky's and
344 others' observation did not instigate a crisis in astrophysics because the measurements did not
345 entirely conflict with their understanding of galaxies [4]. In 1978, Rubin, Ford, and Norbert
346 measured rotation curves for ten spiral galaxies [6]. Rubin et al.'s 1978 publication presented a
347 major challenge to the conventional understanding of galaxies that could no longer be dismissed by
348 measurement uncertainties. Evidence has been mounting ever since for this exotic form of matter.
349 The following subsections provide three compelling pieces of evidence in support of the existence
350 of DM.

351 **2.3.1 First Clues: Stellar Velocities**

352 Zwicky, and later Rubin, measured the stellar velocities of various galaxies to estimate their
353 virial mass. The Virial Theorem upon which these observations are interpreted is written as

$$2T + V = 0. \quad (2.1)$$

354 Where T is the kinetic energy and V is the potential energy in a self-gravitating system. The
355 classical Newton's law of gravity from stars and gas was used for gravitational potential modeled in
356 the observed galaxies:

$$V = -\frac{1}{2} \sum_i \sum_{j \neq i} \frac{m_i m_j}{r_{ij}}. \quad (2.2)$$

357 Zwicky et al. measured just the velocities of stars apparent in optical wavelengths [5]. Rubin et al.
 358 added by measuring the velocity of the hydrogen gas via the 21 cm emission line of Hydrogen [6].
 359 The velocities of the stars and gas are used to infer the total mass of galaxies and galaxy clusters
 360 via Equation (2.1). An inferred mass is obtained from the luminosity of the selected sources. The
 361 two inferences are compared to each other as a luminosity to mass ratio which typically yielded [1]

$$\frac{M}{L} \sim 400 \frac{M_{\odot}}{L_{\odot}} \quad (2.3)$$

362 M_{\odot} and L_{\odot} referring to stellar mass and stellar luminosity, respectively. These ratios clearly indicate
 363 a discrepancy in apparent light and mass from stars and gas and their velocities.

364 Rubin et al. [6] demonstrated that the discrepancy was unlikely to be an underestimation of
 365 the mass of the stars and gas. The inferred "dark" mass was up to 5 times more than the luminous
 366 mass. This dark mass also needed to extend well beyond the extent of the luminous matter.

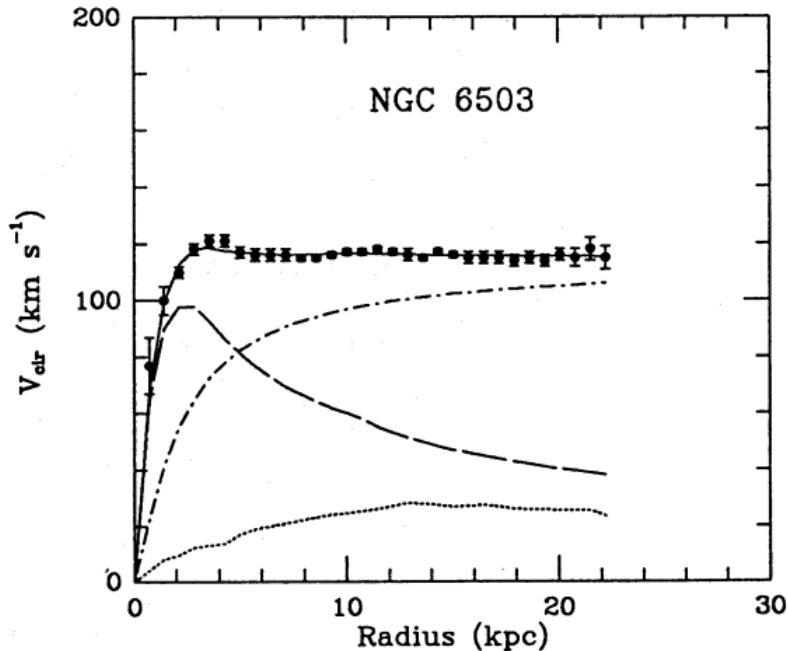


Figure 2.1 Rotation curve fit to NGC 6503 from [7]. Dashed line is the contribution from visible matter. Dotted curves are from gas. Dash-dot curves are from dark matter (DM). Solid line is the composite contribution from all matter and DM sources. Data are indicated with bold dots with error bars. Data agree strongly with a matter + DM composite prediction.

367 Figure 2.1 features one of many rotation curves plotted from the stellar velocities within galaxies.

368 The measured rotation curves mostly feature a flattening of velocities at higher radius which is not
369 expected if the gravity was only coming from gas and luminous matter. The extension of the
370 flat velocity region also indicates that the DM is distributed far from the center of the galaxy.
371 Modern velocity measurements include significantly larger objects, galactic clusters, and smaller
372 objects, dwarf galaxies. Yet, measurements along this regime are leveraging the Virial theorem
373 with Newtonian potential energies. We know Newtonian gravity is not a comprehensive description
374 of gravity. New observational techniques have been developed since 1978, and those are discussed
375 in the following sections.

376 **2.3.2 Evidence for Dark Matter: Gravitational Lensing**

377 Modern evidence for dark matter comes from new avenues beyond stellar velocities. Grav-
378 itational lensing from DM is a new channel from general relativity. General relativity predicts
379 aberrations in light caused by massive objects. In recent decades we have been able to measure the
380 lensing effects from compact objects and DM halos. Figure 2.2 shows how different massive ob-
381 jects change the final image of a faraway galaxy resulting from gravitational lensing. Gravitational
382 lensing developed our understanding of dark matter in two important ways.

383 Gravitational lensing provides additional compelling evidence for DM. The observation of two
384 merging galactic clusters in 2006, shown in Figure 2.3, provided a compelling argument for DM
385 outside the Standard Model. These clusters merged recently in astrophysical time scales. Galaxies
386 and star cluster have mostly passed by each other as the likelihood of their collision is low. Therefore,
387 these massive objects will mostly track the highest mass, dark and/or baryonic, density. Yet, the
388 intergalactic gas is responsible for the majority of the baryonic mass in the systems [4]. These gas
389 bodies will not phase through and will heat up as they collide together. The hot gas is located via
390 x-ray emission from the cluster. Two observations of the clusters were performed independently of
391 each other.

392 The first was the lensing of light around the galaxies due to their gravitational influences.
393 When celestial bodies are large enough, the gravity they exert bends space and time itself. The
394 warped space-time lenses light and will deflect in an analogous way to how glass lenses will bend

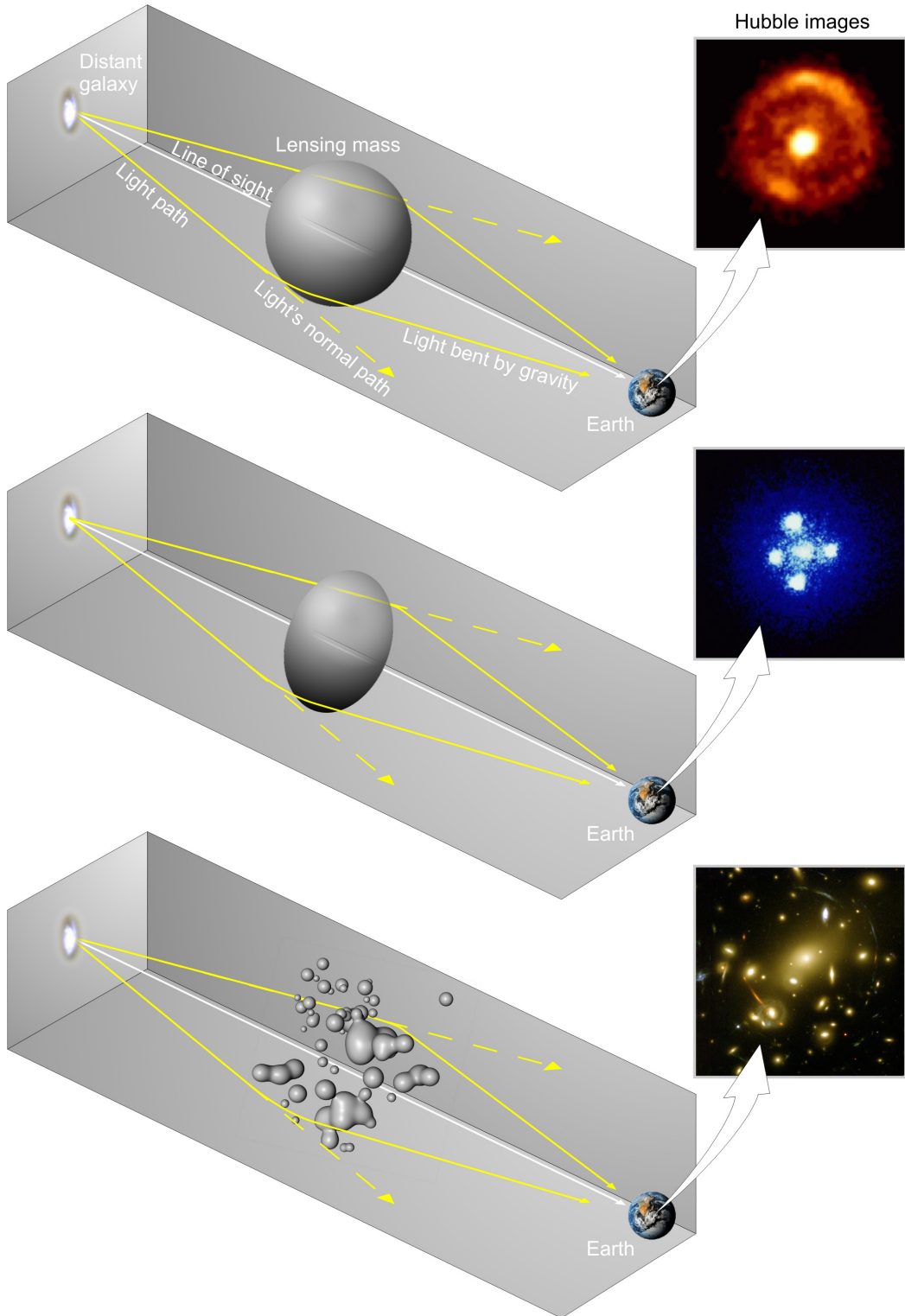


Figure 2.2 Light from distant galaxy is bent in unique ways depending on the distribution of mass between the galaxy and Earth. Yellow dashed lines indicate where the light would have gone if the matter were not present [8].

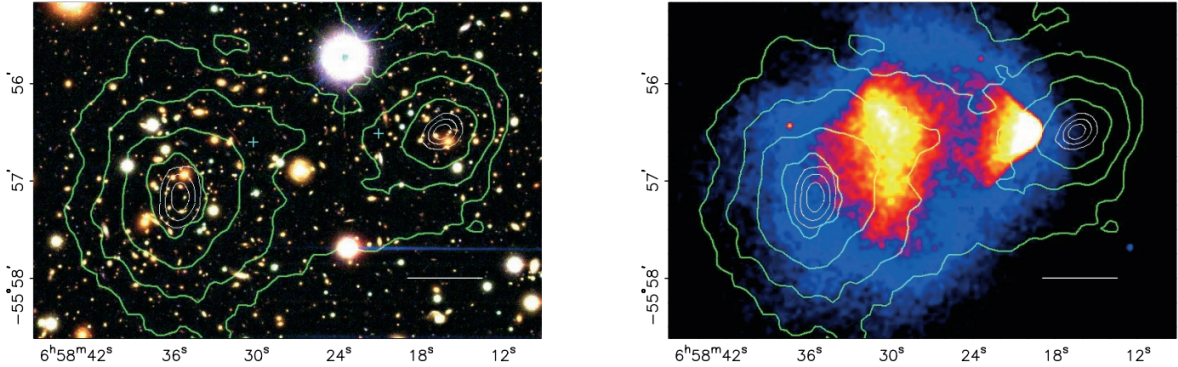


Figure 2.3 (left) Optical image of galactic cluster 1E0657-558. (right) X-ray image of the cluster with redder meaning hotter and higher baryon density. (both) Green contours are reconstruction of gravity contours from weak lensing. White rings are the best fit mass maxima at 68.3%, 95.5%, and 99.7% confidence. The matter maxima of the clusters are clearly separated from x-ray maxima. [9]

395 light, see Figure 2.2. With a sufficient understanding of light sources behind a massive object, we
 396 can reconstruct the contours of the gravitational lenses. The gradient of the contours shown in
 397 Figure 2.3 then indicates how dense the matter is and where it is.

398 The x-ray emission can then be observed from the clusters. Since these galaxies are mostly gas
 399 and are merging, then the gas should be getting hotter. If they are merging, the x-ray emissions
 400 should be the strongest where the gas is mostly moving through each other. Hence, X-ray emission
 401 maps out where the gas is in the merging galaxy cluster.

402 The lensing and x-ray observations were done on the Bullet cluster featured on Figure 2.3.
 403 The x-ray emissions do not align with the gravitational contours from lensing. The incongruence
 404 in mass density and baryon density suggests that there is a lot of matter somewhere that does
 405 not interact with light. Moreover, this dark matter cannot be baryonic [9]. The Bullet Cluster
 406 measurement did not really tell us what DM is exactly, but it did give the clue that DM also does
 407 not interact with itself very strongly. If DM did interact strongly with itself, then it would have been
 408 more aligned with the x-ray emission [9]. There have been follow-up studies of galaxy clusters with
 409 similar results. The Bullet Cluster and others like it provide a persuasive case against something
 410 possibly amiss in our gravitational theories.

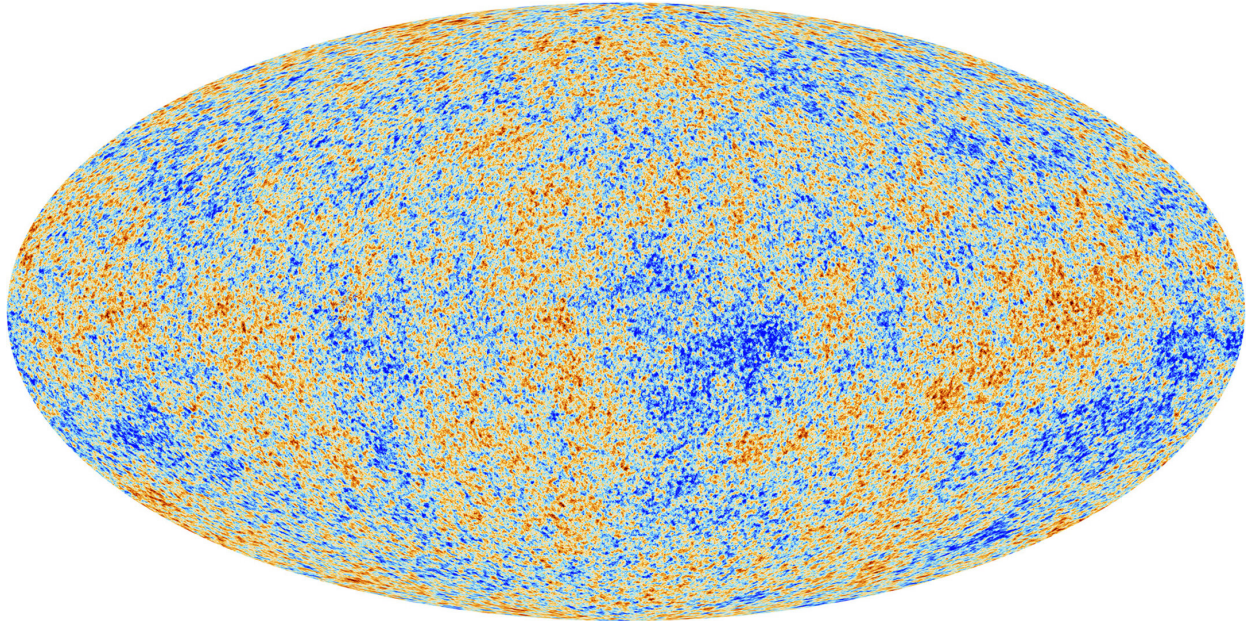


Figure 2.4 Plank CMB sky. Sky map features small variations in temperature in primordial light. These anisotropies are used to make inferences about the universe’s energy budget and developmental history. [10]

411 **2.3.3 Evidence for Dark Matter: Cosmic Microwave Background**

412 The Cosmic Microwave Background (CMB) is the primordial light from the early universe
413 when Hydrogen atoms formed from the free electron and proton soup in the early universe. The
414 CMB is the earliest light we can observe; released when the universe was about 380,000 years old.
415 Then we look at how the simulated universes look like compared to what we see. Figure 2.4 is the
416 most recent CMB image from the Plank satellite after subtracting the average value and masking the
417 galactic plane [10]. Redder regions indicate a slightly hotter region in the CMB, and blue indicates
418 colder. The intensity variations are on the order of 1 in 1000 with respect to the average value.

419 The Cosmic Microwave Background shows that the universe had DM in it from an incredibly
420 early stage. To measure the DM, Dark Energy, and matter fractions of the universe from the CMB,
421 the image is analyzed into a power spectrum, which shows the amplitude of the fluctuations as
422 a function of spherical multipole moments. Λ CDM provides the best fit to the power spectra of
423 the CMB as shown in Figure 2.5. The CMB power spectrum is quite sensitive to the fraction
424 of each energy contribution in the early universe. Low l modes are dominated by variations
425 in gravitational potential. Intermediate l emerge from oscillations in photon-baryon fluid from

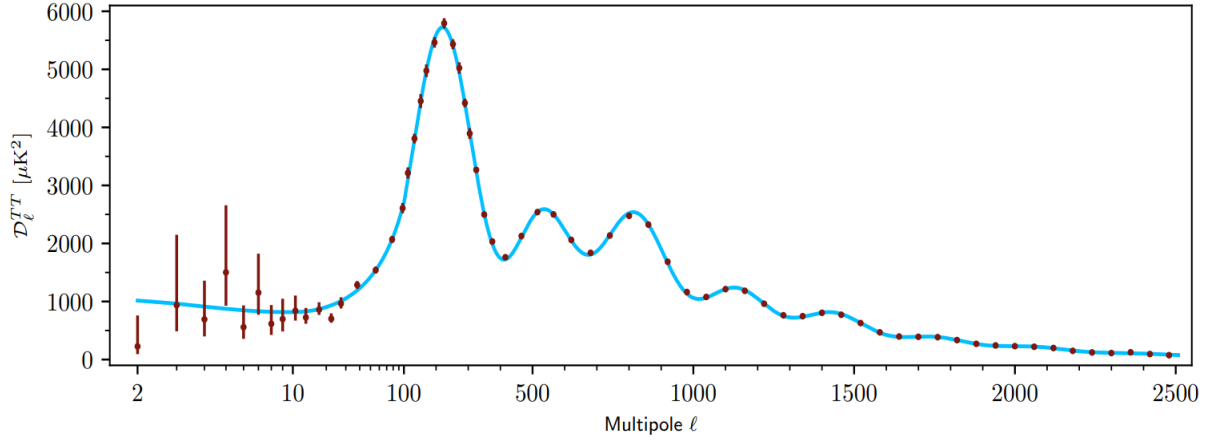


Figure 2.5 Observed Cosmic Microwave Background power spectrum as a function of multipole moment from Plank [10]. Blue line is best fit model from Λ CDM. Red points and lines are data and error, respectively.

426 competing baryon pressures and gravity. High l is a damped region from the diffusion of photons
 427 during electron-proton recombination. [1]

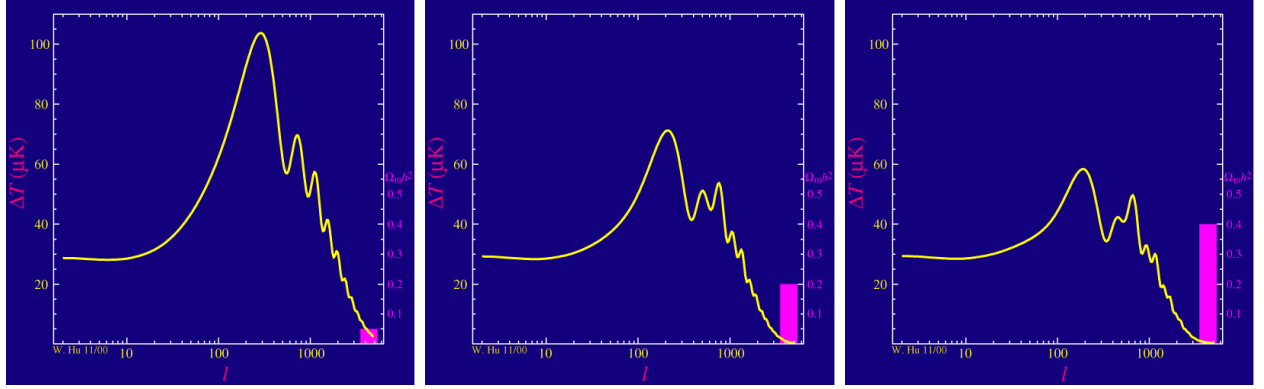


Figure 2.6 Predicted power spectra of CMB for different $\Omega_m h^2$ values for fixed baryon density from [11]. (left) Low $\Omega_m h^2$ increases the prominence of first and second peaks. (middle) $\Omega_m h^2$ is most similar to the observed power spectrum. The second and third peaks are similar in height. (right) $\Omega_m h^2$ is large which suppresses the first peak and raises the prominence of the third peak.

428 The harmonics would look quite different for a universe with less DM. Figure 2.6 demonstrates
 429 the effect $\Omega_m h^2$ has on the expected power spectrum for fixed baryon matter density. [11] Sweeping
 430 $\Omega_m h^2$ in this way clearly shows the effect dark matter has on the CMB power spectrum. The
 431 observations fit well with the Λ CDM model, and the derived fractions are as follows. The matter
 432 fraction: $\Omega_m = 0.3153$; and the baryon fraction: $\Omega_b = 0.04936$ [10]. Plank's observations also
 433 provide a measure of the Hubble constant, H_0 . H_0 especially has seen a growing tension in the

434 past decade that continues to deepened with observations from instruments like the James Webb
435 Telescope [12, 13]. As Hubble tensions deepen, we may find that perhaps Λ **CDM**, despite its
436 successes, is missing some critical physics.

437 Overall, the Newtonian motion of stars in galaxies, weak lensing from galactic clusters, and
438 power spectra from primordial light form a compelling body of research in favor of dark matter.
439 It takes another leap of theory and experimentation to make observations of DM that are non-
440 gravitational in nature. In Section 2.3, the evidence for DM implies strongly that the DM is matter
441 and not a lost parameter in the gravitational fields between massive objects. Finally, if we take one
442 axiom: that this matter has quantum behavior, such as being described by some Bohr wavelength
443 and abiding by some fermion or boson statistics; then we arrive at particle dark matter. One particle
444 DM hypothesis is the Weakly Interacting Massive Particle (WIMP). This DM candidate theory is
445 discussed further in the next section and is the focus of this thesis.

446 2.4 Searching for Dark Matter: Particle DM

447 Section 2.4 shows the Standard Model of particle physics and is currently the most accurate
448 model for the dynamics of fundamental particles like electrons and photons. The current status
449 of the SM does not have a viable DM candidate. When looking at the standard model, we can
450 immediately exclude any charged particle because charged particles interact strongly with light.
451 Specifically, this will rule out the following charged, fundamental particles: $e, \mu, \tau, W, u, d, s, c, t, b$
452 and their corresponding antiparticles. Recalling from Section 2.2 that DM must be long-lived and
453 stable over the age of the universe which excludes all SM particles with decay half-lives at or shorter
454 than the age of the universe. The lifetime constraint additionally eliminates the Z and H bosons.
455 Finally, the candidate DM needs to be somewhat massive. Recall from Section 2.2 that DM is cold
456 or not relativistic through the universe. This eliminates the remaining SM particles: $\nu_{e,\mu,\tau}, g, \gamma$ as
457 DM candidates. Because there are no DM candidates within the SM, the DM problem strongly
458 hints to physics beyond the SM (BSM).

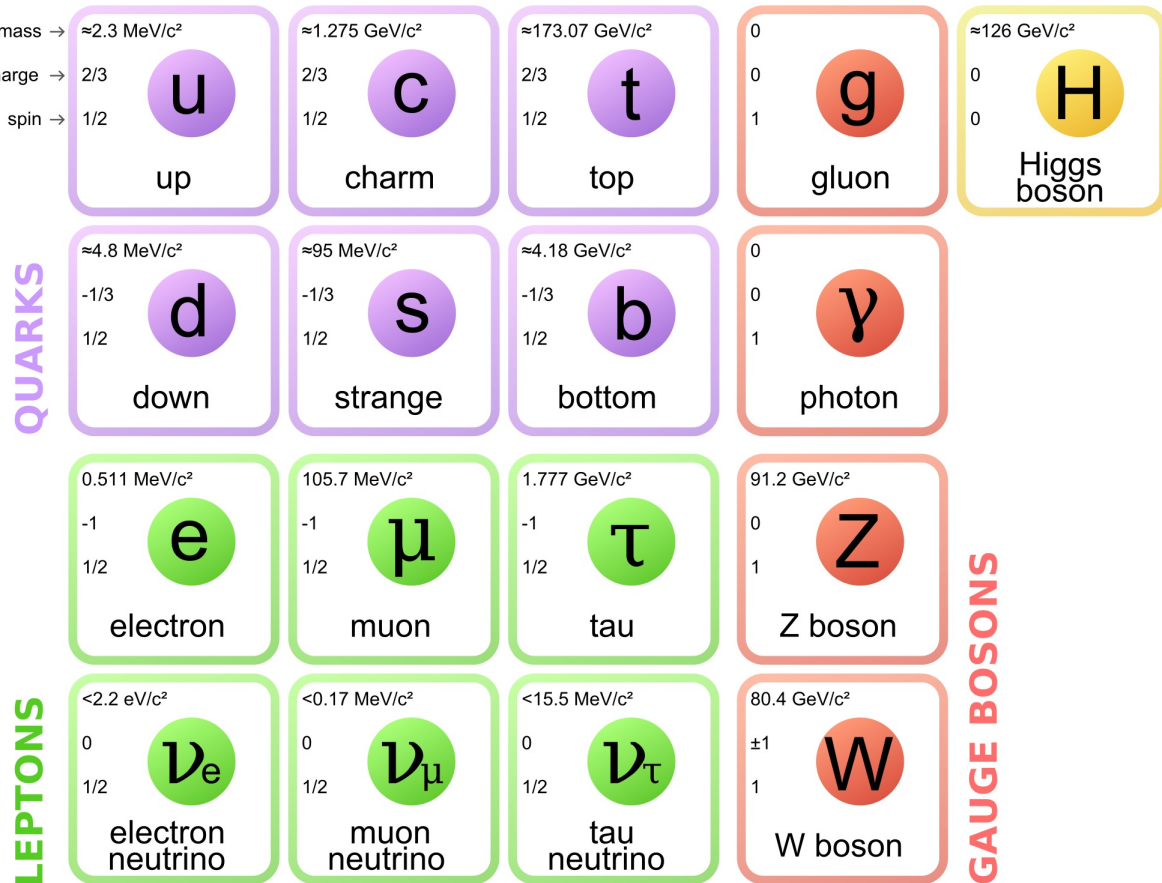


Figure 2.7 The Standard Model (SM) of particle physics. Figure taken from <http://www.quantumdiaries.org/2014/03/14/the-standard-model-a-beautiful-but-flawed-theory/>

459 2.4.1 Shake it, Break it, Make it

460 When considering DM that couples in some way with the SM, the interactions are roughly
 461 demonstrated by interaction demonstrated in Figure 2.8. The figure is a simplified Feynman
 462 diagram where the arrow of time represents the interaction modes of: **Shake it, Break it, Make it**.

463 **Shake it** refers to the direct detection of dark matter. Direct detection interactions start with
 464 a free DM particle and an SM particle. The DM and SM interact via elastic or inelastic collision
 465 and recoil away from each other. The DM remains in the dark sector and imparts some momentum
 466 onto the SM particle. The hope is that the momentum imparted onto the SM particle is sufficiently
 467 high enough to pick up with extremely sensitive instruments. Because we cannot create the DM in
 468 the lab, a direct detection experiment must wait until DM is incident on the detector. Most direct
 469 detection experiments are therefore placed in low-background environments with inert detection

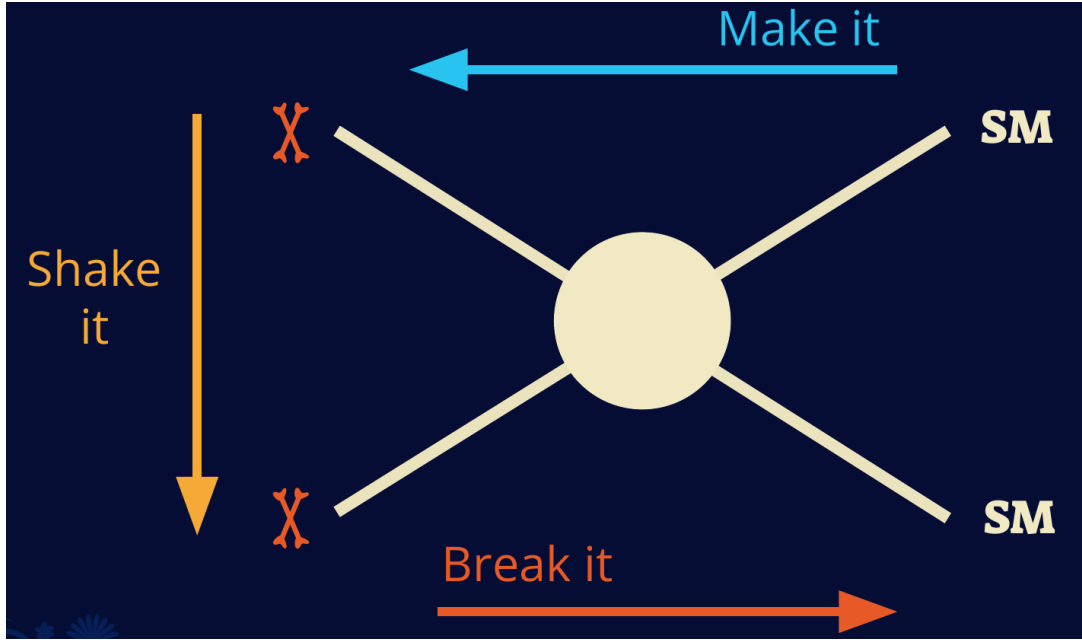


Figure 2.8 Simplified Feynman diagram demonstrating different ways DM can interact with SM particles. The 'X's refer to the DM particles whereas the SM refer to fundamental particles in the SM. The large circle in the center indicates the vertex of interaction and is purposely left vague. The colored arrows refer to different directions of time as well as their respective labels. The arrows indicate the initial and final state of the DM -SM interaction in time.

⁴⁷⁰ media like the noble gas Xenon. [14]

⁴⁷¹ **Make it** refers to the production of DM from SM initial states. The experiment starts with
⁴⁷² particles in the SM. These SM particles are accelerated to incredibly high energies and then collide
⁴⁷³ with each other. In the confluence of energy, DM hopefully emerges as a byproduct of the SM
⁴⁷⁴ annihilation. Often it is the collider experiments that are energetic enough to hypothetically produce
⁴⁷⁵ DM. These experiments include the world-wide collaborations ATLAS and CMS at CERN where
⁴⁷⁶ proton collide together at extreme energies. The DM searches, however, are complex. DM likely
⁴⁷⁷ does not interact with the detectors and lives long enough to escape the detection apparatus of
⁴⁷⁸ CERN's colliders. This means any DM production experiment searches for an excess of events
⁴⁷⁹ with missing momentum or energy in the events. An example event with missing transverse
⁴⁸⁰ momentum is shown in Figure 2.9. The missing momentum with no particle tracks implies a
⁴⁸¹ neutral particle carried the energy out of the detector. However, there are other neutral particles
⁴⁸² in the SM, like neutrons or neutrinos, so any analysis has to account for SM signatures of missing

483 momentum. [15]

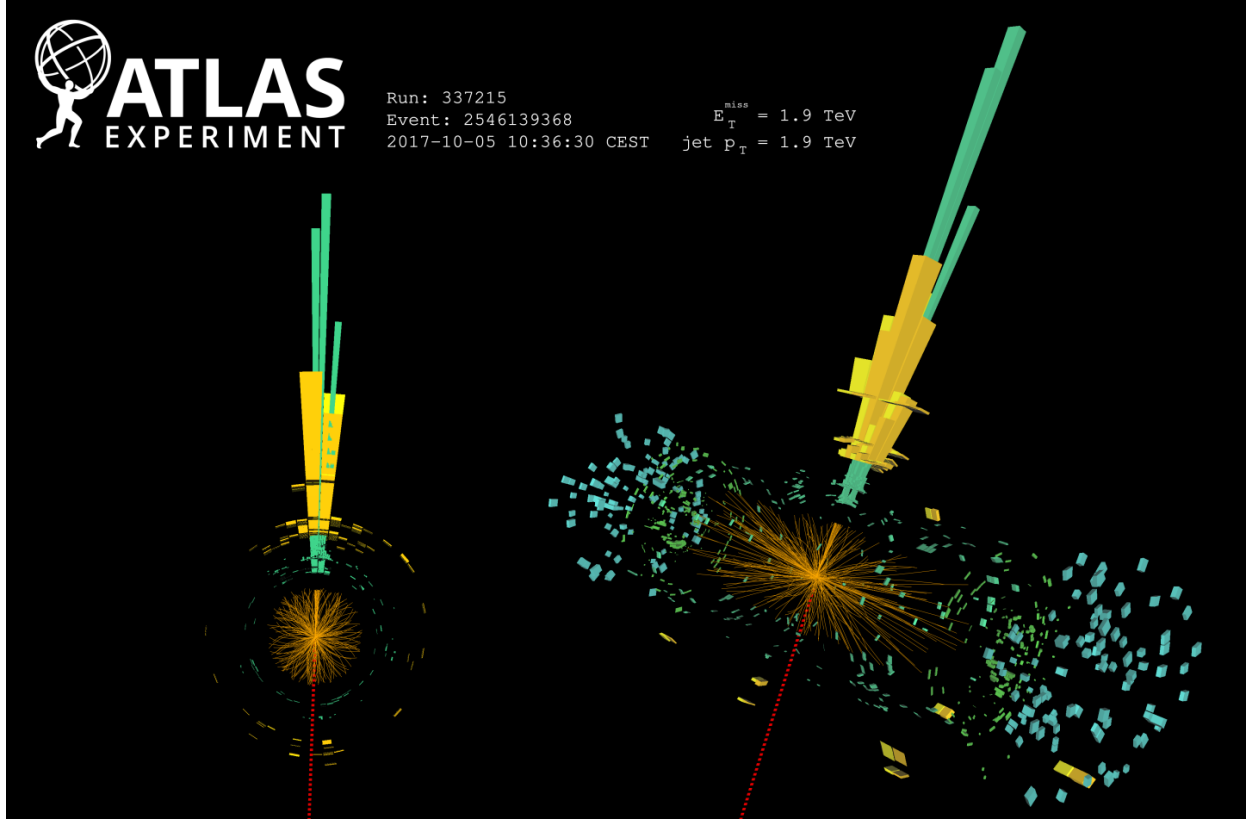


Figure 2.9 A single jet event in ATLAS detector from 2017 [16]. Jet momentum was observed to be 1.9 TeV. Missing transverse momentum was observed to be 1.9 TeV compared to the initial transverse momentum of the event was 0. Implied MET is traced by a red dashed line in event display.

484 2.4.2 Break it: Standard Model Signatures of Dark Matter through Indirect Searches

485 **Break it** refers to the creation of SM particles from the dark sector, and it is the primary focus
486 of this thesis. The interaction begins with DM or in the dark sector. The hypothesis is that this
487 DM will either annihilate with itself or decay and produce an SM byproduct. This method is
488 often referred to as the Indirect Detection of DM because we have no lab to directly control or
489 manipulate the DM. Therefore, most indirect DM searches are performed using observations of
490 known DM densities among the astrophysical sources. The strength is that we have the whole of the
491 universe and its 13.6-billion-year lifespan to use as a detector and particle accelerator. Additionally,
492 locations of dark matter are well cataloged since it was astrophysical observations that presented

493 the problem of DM in the first place.

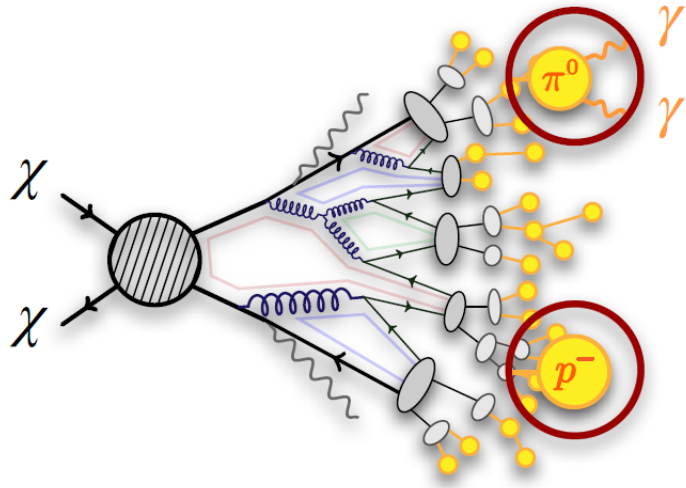


Figure 2.10 More detailed pseudo-Feynman diagram of particle cascade from dark matter annihilation into 2 quarks. The quarks hadronize and down to stable particles like γ or the anti-proton (p^-). Diagram pulled from ICRC 2021 presentation on DM annihilation search [17].

494 However, anything can happen in the universe. There are many difficult to deconvolve back-
495 grounds when searching for DM. One prominent example is the galactic center. We know the
496 galactic center has a large DM content because of stellar kinematics in our Milky Way and DM halo
497 simulations. Yet, any signal from the galactic center is challenging to parse apart from the extreme
498 environment of our supermassive black hole, unresolved sources, and diffuse emission from the
499 interstellar medium [18]. Despite the challenges, any DM model that yields evidence in the other
500 two observation methods, **Shake it or Make it** must be corroborated with indirect observations of
501 the known DM sources. Without corroborating evidence, DM observation in the lab is hard-pressed
502 to demonstrate that it is the model contributing to the DM seen at the universal scale.

503 In the case of WIMP DM, signals are described in terms of primary SM particles produced
504 from DM decay or annihilation. The SM initial state particles are then simulated down to stable
505 final states such as the γ , ν , p , or e which can traverse galactic lengths to reach Earth.

506 Figure 2.10 shows the quagmire of SM particles that emerges from SM initial states that are not
507 stable [17]. There are many SM particles with varying energies that can be produced in such an

508 interaction. For any arbitrary DM source and stable SM particle, the SM flux from DM annihilating
 509 to a neutral particle in the SM, ϕ , from a region in the sky is described by the following.

$$\frac{d\Phi_\phi}{dE_\phi} = \frac{\langle\sigma v\rangle}{8\pi m_\chi^2} \frac{dN_\phi}{dE_\phi} \times \int_{\text{source}} d\Omega \int_{l.o.s} \rho_\chi^2 dl(r, \theta') \quad (2.4)$$

510 In Equation (6.1), $\langle\sigma v\rangle$ is the velocity-weighted annihilation cross-section of DM to the SM. m_χ
 511 refers to the mass of DM, noted with Greek letter χ . $\frac{dN_\phi}{dE_\phi}$ is the N particle flux weighted by the
 512 particle energy. An example is provided in Figure 2.11 for the γ final state. The integrated terms
 513 are performed over the solid angle, $d\Omega$, and line of sight, l.o.s. ρ is the density of DM for a
 514 location (r, θ') in the sky. The terms left of the '×' are often referred to as the particle physics
 515 component. The terms on the right are referred to as the astrophysical component. For decaying
 516 DM, the equation changes to...

$$\frac{d\Phi_\phi}{dE_\phi} = \frac{1}{4\pi\tau m_\chi} \frac{dN_\phi}{dE_\phi} \times \int_{\text{source}} d\Omega \int_{l.o.s} \rho_\chi dl(r, \theta') \quad (2.5)$$

517 In Equation (7.1), τ is the decay lifetime of the DM. Just as in Equation (6.1), the left and right
 518 terms are the particle physics and the astrophysical components respectively. The integrated
 519 astrophysical component of Equation (6.1) is often called the J-Factor. Whereas the integrated
 520 astrophysical component of Equation (7.1) is often called the D-Factor.

521 Exact DM $\text{DM} \rightarrow \text{SM SM}$ branching ratios are not known, so it is usually assumed to go 100%
 522 into an SM particle/anti-particle. Additionally, when a DM annihilation or decay produces one of
 523 the neutral, long-lived SM particles (ν or γ), the particle is traced back to a DM source. For DM
 524 above GeV energies, there are very few SM processes that can produce particles with such a high
 525 energy. Seeing such a signal would almost certainly be an indication of the presence of dark matter.
 526 Fortunately, the universe provides us with the largest volume and lifetime ever for a particle physics
 527 experiment.

528 2.5 Sources for Indirect Dark Matter Searches

529 The first detection of DM relied on optical observations. Since then, we have developed new
 530 techniques to find DM dense regions. As described in Section 2.3.1, many DM dense regions were
 531 through observing galactic rotation curves. Our Milky Way galaxy is among DM dense regions

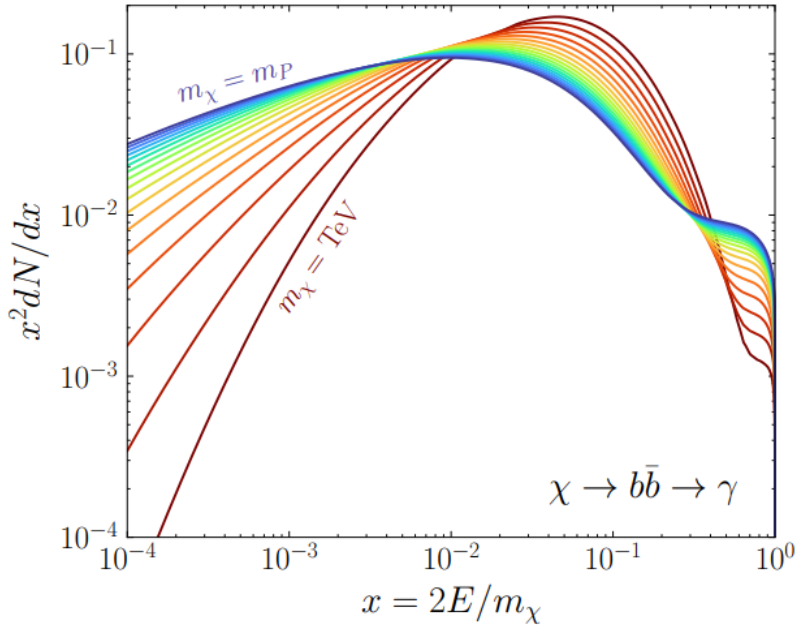


Figure 2.11 Dark Matter (DM) decay spectrum for $b\bar{b}$ initial state and γ final state. Redder spectra are for larger DM masses. Bluer spectra are light DM masses. x is a unitless factor defined as the ratio of the mass of DM, m_χ , and the final state particle energy E_γ . Figure from [19].

discovered, and it is the largest nearby DM dense region to look at. Additionally, the DM halo surrounding the Milky Way is clumpy [18]. There are regions in the DM halo of the Milky Way that have more DM than others that have captured gas over time. These sub-halos were dense enough collapse gas and form stars. These apparent sub galaxies are known as dwarf spheroidal galaxies and are the main sources studied in this thesis. Each source type comes with different trade-offs. Galactic Center studies will be very sensitive to the assumed distribution of DM. The central DM density can vary substantially as demonstrated in Figure 2.12. At distances close to the center of the galaxy, or small r , the differences in DM densities can be 3-4 orders of magnitude. Searches toward the galactic center will therefore be quite sensitive to the assumed DM distribution.

Searches toward Dwarf Spheroidal Galaxies (dSph's) suffer from uncertainties in the DM density less than the galactic center studies. This is mostly from their diminutive size being smaller than the angular resolution of most γ -ray observatories [18]. The DM content dSph's are typically determined with the Virial theorem, Equation (2.1), and are usually majority DM [18] in mass. DSph's tend to be ideal sources to look at for DM searches. Their environments are quiet with little

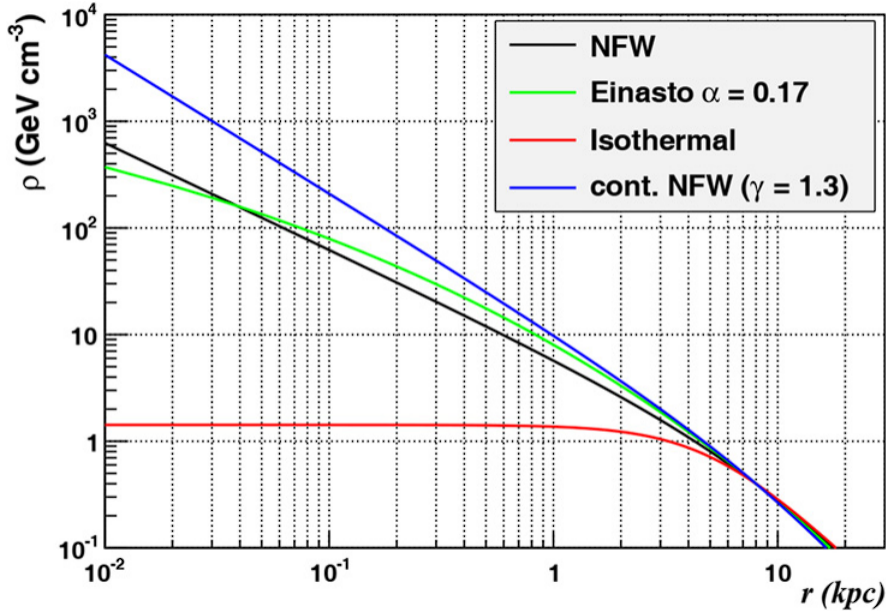


Figure 2.12 Different dark matter density profiles compared. Some models produce exceptionally large densities at small r [20].

546 astrophysical background. Unlike the galactic center, the most active components of dSph's are the
 547 stars within them versus a violent accretion disc around a black hole. All this together means that
 548 dSph's are among the best sources to look at for indirect DM searches. dSph's are the targets of
 549 focus for this thesis.

550 2.6 Multi-Messenger Dark Matter

551 Astrophysics entered a new phase in the past few decades that leverages our increasing sensitivity
 552 to SM channels and general relativity (GR). Up until the 21st century, astrophysical observations
 553 were performed with photons (γ) only. Astrophysics with this 'messenger' is fairly mature now.
 554 Novel observations of the universe have since only adjusted the sensitivity of the wavelength of
 555 light that is observed except at MeV energies. Gems like the CMB [10], and more have ultimately
 556 been observations of different wavelengths of light. Multi-messenger astrophysics proposes using
 557 other SM particles such the $p^{+/-}$, or ν or gravitation waves predicted by general relativity.

558 The experiment LIGO had a revolutionary discovery in 2016 with the first detection of a binary
 559 black hole merger [21]. This opened the collective imagination to observing the universe through
 560 gravitational waves. There has also been a surge of interest in the neutrino (ν) sector. IceCube

561 demonstrated that we are sensitive to neutrinos in regions that correlate with significant photon
 562 emission like the galactic plane [22]. Neutrinos, like gravitational waves and light, travel mostly
 563 unimpeded from their source to our observatories. This makes pointing to the originating source
 564 of these messengers much easier than it is for cosmic rays which are deflected from their source by
 565 magnetic fields.

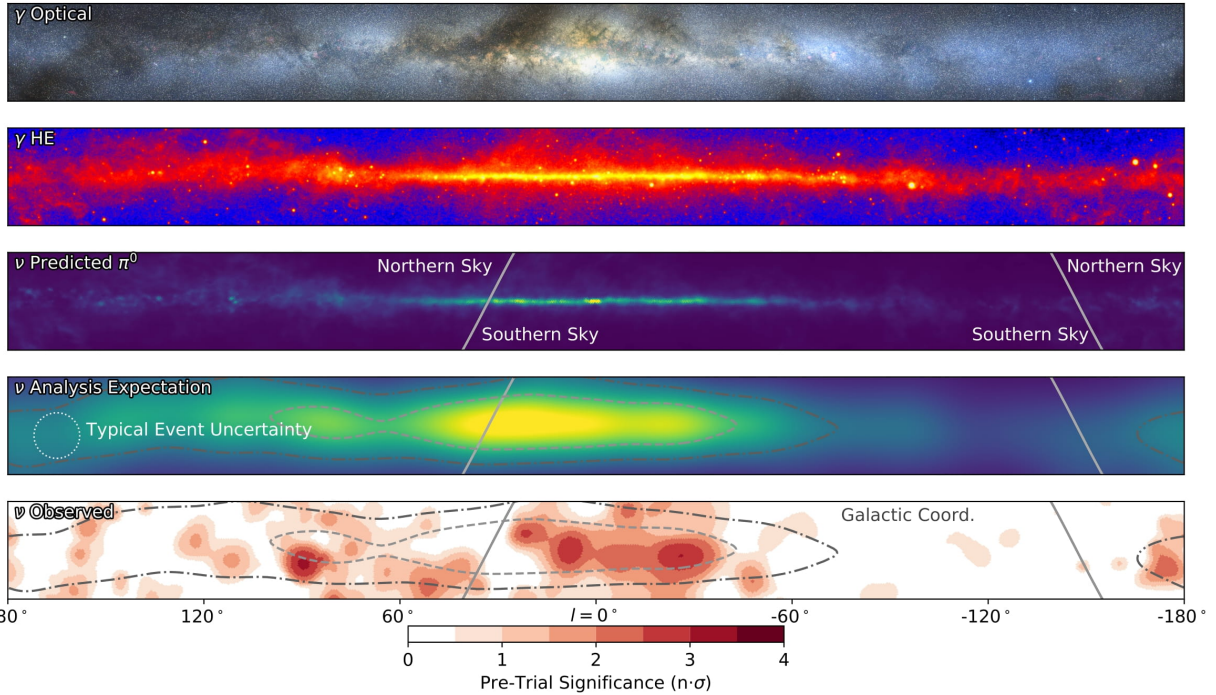


Figure 2.13 The Milky Way Galaxy in photons (γ) and neutrinos (ν) [22]. The Galactic center is at $l=0^\circ$ and is the brightest region in all panels. (top) An Optical color image of the Milky Way galaxy seen from Earth. Clouds of gas and dust obscure some light from stars. (2nd down) Integrated flux of γ -rays observed by the Fermi-LAT telescope [23]. (middle) Expected neutrino emission that corresponds with Fermi-LAT observations. (2nd up) Expected neutrino emission profile after considering detector systematics of IceCube. (bottom) Observed neutrino emission from region of the galactic plane. Substantial neutrino emission was detected.

566 The IceCube collaboration recently published a groundbreaking result of the Milky Way in
 567 neutrinos. The recent result from IceCube, shown in Figure 2.13, proves that we can make
 568 observations under different messenger regimes. The top two panels show the appearance of the
 569 galactic plane to different wavelengths of light. Some sources are more apparent in some panels,
 570 while others are not. This new channel is powerful because neutrinos are readily able to penetrate
 571 through gas and dust in the Milky Way. This new image also refines our understanding of how high

572 energy particles are produced. For example, the fit to IceCube data prefers neutrino production
 573 from the decay of π^0 [22].

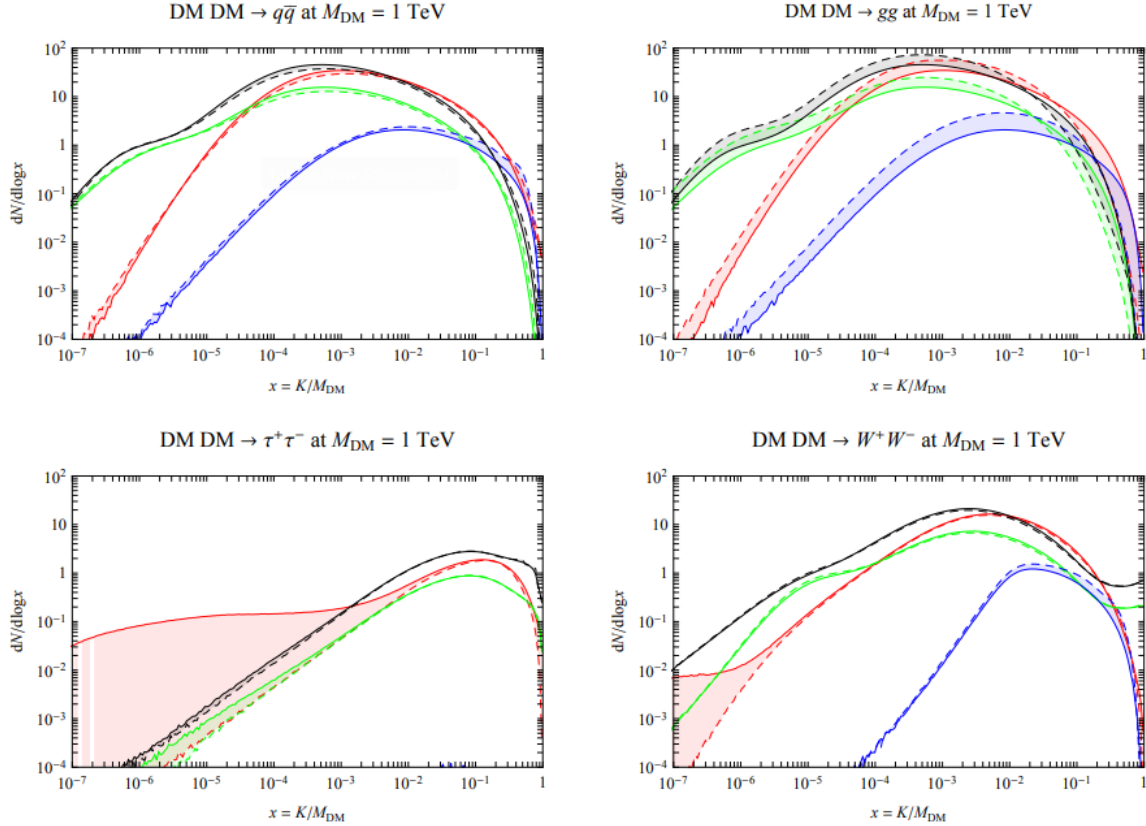


Figure 2.14 Dark Matter annihilation spectra for different final state particle and standard model annihilation channels [24]. Photons (red), e^\pm (green), \bar{p} (blue), ν (black).

574 Exposing our observations to more cosmic messengers greatly increases our sensitivity to
 575 rare processes. In the case of DM, Figure 2.14, there are many SM particles produced in DM
 576 annihilation. Among the final state fluxes are gammas and neutrinos. Charged particles are also
 577 produced however they would not likely make it to Earth since they will be deflected by magnetic
 578 fields between the source and Earth. This means observatories that can see the neutral messengers
 579 are especially good for DM searches and for combining data for a multi-messenger DM search.

CHAPTER 3

580 MULTIMESSENGER ASTROPHYSICS: DETECTING HIGH ENERGY NEUTRAL 581 MESSENGERS

582 3.1 Introduction

583 Before the 20th century, all asttrophysics observations were optical in nature. We litterly only
584 saw things with highly magnified optical observations. Then we discovered cosmic rays. cosmic
585 rays are charged particles, typically naked protons or H+. This was seen by Victor Hess in 19??.
586 Around the same time we discovered neutrinos from beta decay. Sometime around 1950 we started
587 to build neutrino detectors which were mostly sensitive to neutrinos from the sun. Finally, it was
588 theorized that compact objects like black holes and neutron stars would create waves in space-time
589 when they experience mergers or collisions.

590 In the 21st century, we have developed new observation techniques and detectors that are no only
591 sensitive to these four messengers - photons (TODO: photon), neutrinos (TODO: nu), Cosmic
592 Rays (CR), and Gravitational Wave (WV) - we're collect high energy versions of these events.
593 For the standad model particles, we're now sensitive to all messengers above the MeV eneryg
594 range. Additionally, the GW's were sensitive to are in the stellar mass black hole region and above
595 within our galactic neighborhood. This means were becoming sensitive to the fundamental physics
596 occuring within the universe and we can rely on the universe as a TeV+ particle accelerator. We
597 also have the abaility to correlate high energy events across messengers and gain new insights on
598 the processes that occur in our universe.

599 This thesis focuses on very high energy (VHE) gamma rays and neutrinos. These can both be
600 observed through the water cherenkov detection technique altho not exclusively. Methods on how
601 to detect and observe these neutral messengers are discussed Section 3.3 and Section 3.4

602 3.2 Charged Particles in a Medium

603 For high enery gamma-rays and neutrinos, we can exploit the same effect that charged particles
604 have with water. This effect is known as Cherenkov radiation. Cherenkov Radiation occurs when a
605 charged particle, usually electrons (e) or muons (μ), traverse a medium, like water, faster than the

606 speed of light in that medium. This is similar to sonic boom where an object moves through air
607 faster than the speed of sound in air. Cherenkov radiation can therefore be thought of as an 'optic
608 boom'. Many astro-particle physics experiments will use water as the medium as because water
609 has a unique set of properties ideal for charged particle tracking.



Figure 3.1 TODO: Show a nuclear reactor with cherenkov radiation[NEEDS A SOURCE][FACT CHECK THIS]

610 The frequency of light emitted due to cherenkov radiation follows the equation:

$$INSERT\ Cherenkov\ wavelength\ calc\ HERE. \quad (3.1)$$

611 The absorption spectra is shown in the following figure:

612 **3.3 Photons (γ)**

613 **3.4 Neutrinos (ν)**

614 **3.5 Opportunities to Combine for Dark Matter**



Figure 3.2 TODO: absorption spectrum of liquid and solid water[NEEDS A SOURCE][FACT CHECK THIS]

CHAPTER 4

615 **HIGH ALTITUDE WATER CHERENKOV (HAWC) OBSERVATORY**

616 **4.1 The Detector**

617 **4.2 Events Reconstruction and Data Acquisition**

618 **4.2.1 G/H Discrimination**

619 **4.2.2 Angle**

620 **4.2.3 Energy**

621 **4.3 Remote Monitoring**

622 **4.3.1 ATHENA Database**

623 **4.3.2 HOMER**

624

CHAPTER 5

ICECUBE NEUTRINO OBSERVATORY

625 **5.1 The Detector**

626 **5.2 Events Reconstruction and Data Acquisition**

627 **5.2.1 Angle**

628 **5.2.2 Energy**

629 **5.3 Northern Test Site**

630 **5.3.1 PIgeon remote dark rate testing**

631 **5.3.2 Bulkhead Construction**

CHAPTER 6

GLORY DUCK: MULTI-WAVELENGTH SEARCH FOR DARK MATTER ANNIHILATION TOWARDS DWARF SPHEROIDAL GALAXIES

6.1 Introduction

The field of astrophysics now has several instruments and observatories sensitive to high energy gamma-rays. The energy sensitivity for the modern gamma-ray program spans many orders of magnitude. Figure 6.1 demonstrates these similar sensitivities across energies for the five experiments: Fermi-LAT, HAWC, HESS, MAGIC, and VERITAS.

Each of the five experiments featured in Figure 6.1 have independently searched for DM annihilation from dwarf spheroidal galaxies (dSph) and set limits. Intriguingly, there are regions of substantial overlap in their energy sensitivities. This clearly motivates an analysis that combines data from these five. Each experiment has unique gamma-ray detection methods and their weaknesses and strengths can be leveraged with each other. The HAWC gamma-ray observatory is extensively introduced in chapter 4, so it is not introduced here. A brief description of the remaining experiments are in the following paragraphs.

The Large Area Telescope (LAT) is a pair conversion telescope mounted on the NASA Fermi satellite in orbit \sim 550 km above the Earth [26]. LAT's field of view covers about 20% of the whole sky, and it sweeps the whole sky approximately every 3 hours. LAT's gamma-ray energy sensitivity ranges from 20 MeV up to 1 TeV. Previous DM searches towards dSphs using Fermi-LAT are published in [27] and [28]

The High Energy Spectroscopic System (HESS), Major Atmospheric Gamma Imaging Cherenkov (MAGIC), and Very Energetic Radiation Imaging Telescope Array System (VERITAS) are arrays of Imaging Atmospheric Cherenkov Telescopes (IACT). These telescopes observe the Cherenkov light emitted from gamma-ray showers in the Earth's atmosphere. The field of view for these telescopes is no larger than 5° with energy sensitivities ranging from 30 GeV up to 100 TeV [29, 30, 31]. IACTs are able to make precise observations in selected regions of the sky, however can only be operated in ideal dark conditions. HESS's observations of the dwarves

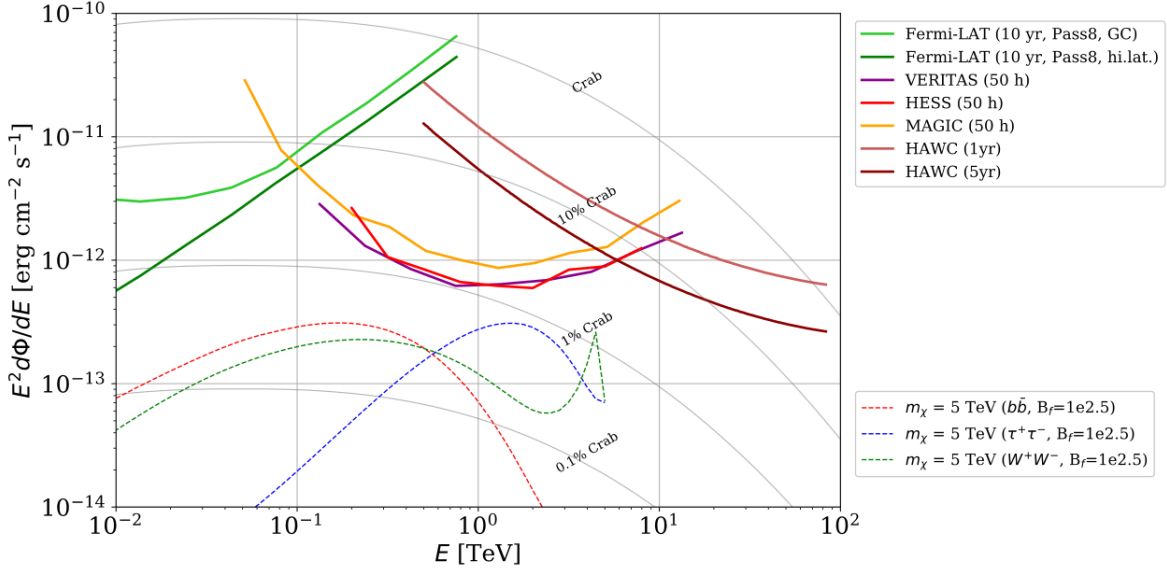


Figure 6.1 Sensitivities of five gamma-ray experiments compared to percentages of the Crab nebula’s emission and dark matter annihilation. Solid lines present estimated sensitivities to power law spectra [FACT CHECK THIS] for each experiment. Green lines are Fermi-LAT sensitivities where lighter green is the sensitivity to the galactic center and dark green is its sensitivity to higher declinations. Orange, red, and purple solid lines represent the MAGIC, HESS, and VERITAS 50 hour sensitivities respectively. The maroon and brown lines are the HAWC 1 year and 5 year sensitivities. Across four decades of gamma-ray energy, these experiments have similar sensitivities on the order 10^{-12} erg $\text{cm}^{-2}\text{s}^{-1}$. The dotted lines are estimated dark matter fluxes assuming $m_\chi = 5$ TeV DM annihilating to bottom quarks (red), tau leptons (blue), and W bosons (green). Faded gray lines outline percentage flux of the Crab nebula. Figure is an augmented version of [25]

658 Sculptor and Carina were between January 2008 and December 2009. HESS’s observations of
 659 Coma Berenices were from 2010 to 2013, and Fornax was observed in 2010 [32, 33, 34]. MAGIC
 660 provided deep observations of Segue1 between 2011 and 2013 [35]. MAGIC also provides data
 661 for three dwarves: Coma Berenices, Draco, and Ursa Major II where observations were made
 662 in: January - June 2019 [36], March - September 2018 [36], and 2014 - 2016 [37] respectively.
 663 VERITAS provided data for Boötes I, Draco, Segue 1, and Ursa Minor from 2009 to 2016 [38].

664 This chapter presents the Glory Duck analysis, the name given for the search for dark matter
 665 annihilation from dSph by combining data from the five gamma-ray observatories: Fermi-LAT,
 666 HAWC, HESS, MAGIC, and VERITAS. Specifically, the methods in analysis and modeling are
 667 presented for the HAWC gamma-ray observatory. This work was published to the Journal of
 668 Cosmology and Astroparticle Physics and presented at the International Cosmic Ray Conference

669 in 2019, 2021, and 2023 [39, 40, 41] and others.

670 **6.2 Dataset and Background**

671 This section enumerates the data and background methods used for HAWC's study of dSphs.

672 Section 6.2.1 and Section 6.2.2 are most useful for fellow HAWC collaborators looking to replicate

673 the Glory Duck analysis.

674 **6.2.1 Itemized HAWC files**

675 • Detector Resolution: `response_aerie_svn_27754_systematics_best_mc_test_no`
676 `broadpulse_10pctlogchargesmearing_0.63qe_25kHzNoise_run5481_curvatu`
677 `re0_index3.root`

678 • Data Map: `maps-20180119/liff/maptree_1024.root`

679 • Spectral Dictionary: `DM_CirrelliSpectrum_dict_gammas.npy`

680 • Analysis wiki: https://private.hawc-observatory.org/wiki/index.php/Glory_Duck_Multi-Experiment_Dark_Matter_Search

682 **6.2.2 Software Tools and Development**

683 This analysis was performed using HAL and 3ML [42, 43] in Python version 2. I built software
684 to implement the *A Poor Particle Physicist Cookbook for Dark Matter Indirect Detection* (PPPC)
685 [44] DM spectral model and dSphs spatial model from [45] for HAWC analysis. A NumPy version
686 of this dictionary was made for both Py2 and Py3. The code base for creating this dictionary is
687 linked on my GitLab sandbox:

688 • Py2: [Dictionary Generator \(Deprecated\)](#)

689 • Py3: [PPPC2Dict](#)

690 The analysis was performed using the f_{hit} framework performed in the HAWC Crab paper
691 [42]. The Python2 NumPy dictionary file for gamma-ray final states is `dmCirSpecDict.npy`. The
692 corresponding Python3 file is `DM_CirrelliSpectrum_dict_gammas.npy`. These files can also

693 be used for decay channels and the PPPC describes how [44]. All other software used for data
694 analysis, DM profile generation, and job submission to SLURM are also kept in my sandbox for
695 [the Glory Duck](#) project.

696 **6.2.3 Data Set and Background Description**

697 The HAWC data maps used for this analysis contain 1017 days of data between runs 2104
698 (2014-11-26) and 7476 (2017-12-20). They were generated from pass 4.0 reconstruction. The
699 analysis is performed using the f_{hit} energy binning scheme with bins (1-9) similar to what was done
700 for the Crab and previous HAWC dSph analysis [42, 46]. Bin 0 was excluded as it has substantial
701 hadronic contamination and poor angular resolution.

702 This analysis was done on dSphs because of their large DM mass content relative to baryonic
703 mass. We consider the following to estimate the background to this study.

- 704 • The dSphs are small in HAWC’s field of view, so the analysis is not sensitive to large or small
705 scale anisotropies.
- 706 • The dSphs used in this analysis are off the galactic plane.
- 707 • The dSphs are baryonically faint relative to their expected dark matter content and are not
708 expected to contain high energy gamma-ray sources.

709 Therefor we make no additional assumptions on the background from our sources and use
710 HAWC’s standard direct integration method for background estimation [42]. It is possible for
711 gamma rays from DM annihilation to scatter in transit to HAWC via Inverse Compton Scattering
712 (ICS). This was investigated and its impact on the flux is basically zero. Supporting information
713 on this is in Section 6.7.1

714 **6.3 Analysis**

715 The expected differential photon flux from DM-DM annihilation to standard model particles,
716 $d\Phi_\gamma/dE_\gamma$, over solid angle, Ω is described by the familiar equation.

$$\frac{d\Phi_\gamma}{dE_\gamma} = \frac{\langle\sigma v\rangle}{8\pi m_\chi^2} \frac{dN_\gamma}{dE_\gamma} \times \int_{\text{source}} d\Omega \int_{l.o.s} \rho_\chi^2 dl(r, \theta') \quad (6.1)$$

717 Where $\langle \sigma v \rangle$ is the velocity weighted annihilation cross-section. $\frac{dN}{dE}$ is the expected differential
 718 number of photons produced at each energy per annihilation. m_χ is the rest mass of the supposed
 719 DM particle. ρ_χ is the DM density. J is the astrophysical J-factor and is defined as

$$J = \int d\Omega \int_{l.o.s} dl \rho_\chi^2(r, \theta') \quad (6.2)$$

720 l is the distance to the source from Earth. r is the radial distance from the center of the source. θ' is
 721 the half angle defining a cone containing the DM source. How each component is synthesized and
 722 considered for HAWC's analysis is presented in the following sections. Section 6.3.1 presents the
 723 particle physics model for DM annihilation. Section 6.3.2 presents the spatial distributions built
 724 for each dSph.

725 6.3.1 $\frac{dN_\gamma}{dE_\gamma}$ - Particle Physics Component

726 For these spectra, we import the PPPC with Electroweak (EW) corrections [44]. The spectrum
 727 is implemented as a model script in astromodels for 3ML. The EW corrections were previously not
 728 considered for HAWC and are significant for DM annihilating to EW coupled SM particles such
 729 as all leptons, and the γ , Z , and W bosons [46]. Figure 6.2 demonstrates the significance of EW
 730 corrections for W boson annihilation. Across EW SM channels, the gamma-ray spectra become
 731 harder than spectra without EW corrections. Tables from the PPPC were reformatted into Python
 732 NumPy dictionaries for collaboration-wide use. A class in astromodels was developed to include
 733 the EW correction from the PPPC and is aptly named `PPPCSpectra` within `DM_models.py`.

734 6.3.2 J - Astrophysical Component

735 The J-factor profiles for each source are imported from Geringer-Sameth (referred to with \mathcal{GS})
 736 [45]. These were pulled from the publication as $J(\theta)$, where θ is the angular separation from the
 737 center of the source. HAWC requires maps in terms of $\frac{dJ}{d\Omega}$, so the conversion from the maps was
 738 done in the following way...

739 First, convert the angular distances to solid angles

$$\Omega = 2 \cdot \pi(1 - \cos(\theta)) \quad (6.3)$$

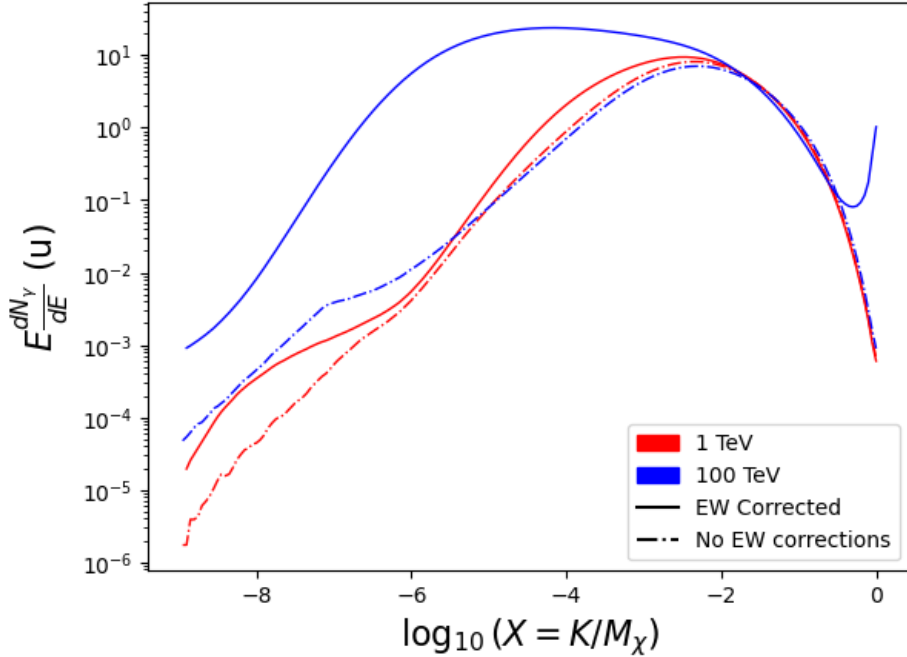


Figure 6.2 Effect of Electroweak (EW) corrections on expected DM annihilation spectrum for $\chi\chi \rightarrow W^-W^+$. Solid lines are spectral models that consider EW corrections. Dash-dot lines are spectral models without EW corrections. Red lines are models for $M_\chi = 1$ TeV. Blue lines represent models for $M_\chi = 100$ TeV. All models are sourced from the PPPC4DMID [44].

740 which reduces with a small angle approximation to $\pi\theta^2$. Next, the central difference for both the
 741 ΔJ and $\Delta\Omega$ value were calculated from the discretized $J(\theta)$ with the central difference stencil:

$$\Delta\phi_i = \phi_{i+1} - \phi_{i-1} \quad (6.4)$$

742 Where ϕ is either Ω or J . These were done separately in case the grid spacing in θ was not uniform.
 743 Finally, these lists are divided so that we are left with an approximation of the $dJ/d\Omega$ profile that
 744 is a function of θ . Admittedly, this is an approximation method for the map which introduces small
 745 errors compared to the true profile estimate. This was checked as a systematic against the author's
 746 profiling of the spatial distribution and is documented in Section 6.8.1.

747 With $\frac{dJ}{d\Omega}(\theta)$, a map is generated, first by filling in the north-east quadrant of the map. This
 748 quadrant is then reflected twice, vertically then horizontally, to fill the full map. Maps are then
 749 normalized by dividing the discrete 2D integral of the map. The 2D integral was a simple height

750 of bins, Newton's integral:

$$p^2 \cdot \sum_{i,j=0}^{N,M} \frac{dJ}{d\Omega}(\theta_{i,j}, \phi_{i,j}) \quad (6.5)$$

751 These maps are HEALpix maps with NSIDE 16384 and saved in the `.fits` format.

752 Another DM spatial distribution model from Bonnivard (\mathcal{B}) [47] was used for the Glory Duck
753 study. However, to save computational time, limits from \mathcal{GS} were scaled to \mathcal{B} instead of each
754 experiment performing a full study a second time. How these models compare is demonstrated
755 for each dSph in Figure 6.16 and Figure 6.17 Plots of these maps are provided for each source
756 in chapter A Examples of the two most impactful dSphs derived from \mathcal{GS} , Segue1 and Coma
757 Berenices are featured in Figure 6.3

758 6.3.3 Source Selection and Annihilation Channels

759 We use many of the dSphs presented in HAWC's previous dSph DM search [46]. HAWC's
760 sources for Glory Duck include Boötes I, Coma Berenices, Canes Venatici I + II, Draco, Hercules,
761 Leo I, II, + IV, Segue 1, Sextans, and Ursa Major I + II. A full description of all sources used
762 in Glory Duck is found in Table 6.1. Triangulum II was excluded from the Glory Duck analysis
763 because of large uncertainties in its J factor. Ursa Minor was excluded from HAWC's contribution
764 to the combination because the source extension model extended Ursa Minor beyond HAWC's field
765 of view. Ursa Minor was not expected to contribute significantly to the combined limit, so work
766 was not invested in a solution to include Ursa Minor.

767 This analysis improves on the previous HAWC dSph paper [46] in the following ways. Pre-
768 viously, the dSphs were treated and implemented as point sources. For this analysis, dSphs are
769 modeled and treated as extended source. The impact of this change with respect to the upper limit
770 is source dependent and is explored in Section 6.7.2. Previously, the particle physics model used for
771 gamma-ray spectra from DM annihilation did not have EW corrections where the PPPC includes
772 them. Finally, the gamma-ray ray dataset is much larger. The study performed here analyzes over
773 1000 days of data compared to 507.

774 The SM annihilation channels probed for the Glory Duck combination include $b\bar{b}$, $e\bar{e}$, $\mu\bar{\mu}$, $\tau\bar{\tau}$,
775 $t\bar{t}$, W^+W^- , and ZZ . A summary of all sources, with a description of each experiments' sensitivity

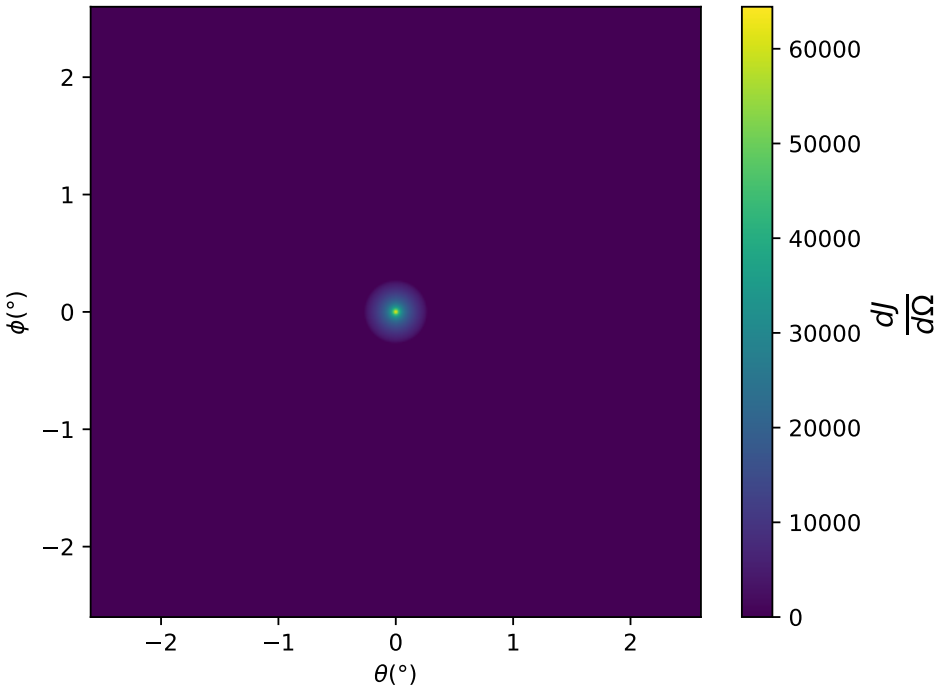
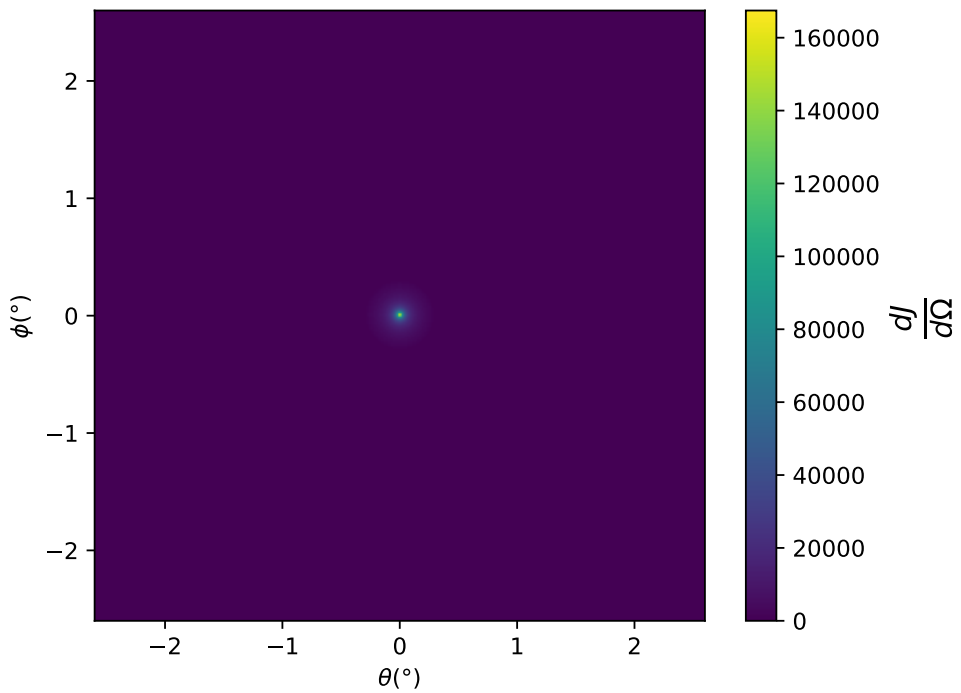


Figure 6.3 $\frac{dJ}{d\Omega}$ maps for Segue1 (top) and Coma Berenices (bottom). Origin is centered on the specific dwarf spheroidal galaxies (dSph). X and Y axes are the angular separation from the center of the dwarf. Plots of the remaining 11 dSph HAWC studied are linked in Fig. A.1.

Table 6.1 Summary of the relevant properties of the dSphs used in the present work. Column 1 lists the dSphs. Columns 2 and 3 present their heliocentric distance and galactic coordinates, respectively. Columns 4 and 5 report the J -factors of each source given from the \mathcal{GS} and \mathcal{B} independent studies and their estimated $\pm 1\sigma$ uncertainties. The values $\log_{10} J$ (\mathcal{GS} set) [45] correspond to the mean J -factor values for a source extension truncated at the outermost observed star. The values $\log_{10} J$ (\mathcal{B} set) [47] are provided for a source extension at the tidal radius of each dSph. **Bolded sources are within HAWC's field of view and provided to the Glory Duck analysis.**

Name	Distance (kpc)	l, b ($^{\circ}$)	$\log_{10} J$ (\mathcal{GS} set) $\log_{10}(\text{GeV}^2 \text{cm}^{-5} \text{sr})$	$\log_{10} J$ (\mathcal{B} set) $\log_{10}(\text{GeV}^2 \text{cm}^{-5} \text{sr})$
Boötes I	66	358.08, 69.62	$18.24^{+0.40}_{-0.37}$	$18.85^{+1.10}_{-0.61}$
Canes Venatici I	218	74.31, 79.82	$17.44^{+0.37}_{-0.28}$	$17.63^{+0.50}_{-0.20}$
Canes Venatici II	160	113.58, 82.70	$17.65^{+0.45}_{-0.43}$	$18.67^{+1.54}_{-0.97}$
Carina	105	260.11, -22.22	$17.92^{+0.19}_{-0.11}$	$18.02^{+0.36}_{-0.15}$
Coma Berenices	44	241.89, 83.61	$19.02^{+0.37}_{-0.41}$	$20.13^{+1.56}_{-1.08}$
Draco	76	86.37, 34.72	$19.05^{+0.22}_{-0.21}$	$19.42^{+0.92}_{-0.47}$
Fornax	147	237.10, -65.65	$17.84^{+0.11}_{-0.06}$	$17.85^{+0.11}_{-0.08}$
Hercules	132	28.73, 36.87	$16.86^{+0.74}_{-0.68}$	$17.70^{+1.08}_{-0.73}$
Leo I	254	225.99, 49.11	$17.84^{+0.20}_{-0.16}$	$17.93^{+0.65}_{-0.25}$
Leo II	233	220.17, 67.23	$17.97^{+0.20}_{-0.18}$	$18.11^{+0.71}_{-0.25}$
Leo IV	154	265.44, 56.51	$16.32^{+1.06}_{-1.70}$	$16.36^{+1.44}_{-1.65}$
Leo V	178	261.86, 58.54	$16.37^{+0.94}_{-0.87}$	$16.30^{+1.33}_{-1.16}$
Leo T	417	214.85, 43.66	$17.11^{+0.44}_{-0.39}$	$17.67^{+1.01}_{-0.56}$
Sculptor	86	287.53, -83.16	$18.57^{+0.07}_{-0.05}$	$18.63^{+0.14}_{-0.08}$
Segue I	23	220.48, 50.43	$19.36^{+0.32}_{-0.35}$	$17.52^{+2.54}_{-2.65}$
Segue II	35	149.43, -38.14	$16.21^{+1.06}_{-0.98}$	$19.50^{+1.82}_{-1.48}$
Sextans	86	243.50, 42.27	$17.92^{+0.35}_{-0.29}$	$18.04^{+0.50}_{-0.28}$
Ursa Major I	97	159.43, 54.41	$17.87^{+0.56}_{-0.33}$	$18.84^{+0.97}_{-0.43}$
Ursa Major II	32	152.46, 37.44	$19.42^{+0.44}_{-0.42}$	$20.60^{+1.46}_{-0.95}$
Ursa Minor	76	104.97, 44.80	$18.95^{+0.26}_{-0.18}$	$19.08^{+0.21}_{-0.13}$

776 to the source, is provided in Table 6.2.

777 6.4 Likelihood Methods

778 6.4.1 HAWC Likelihoods

779 For every analysis bin in energy, f_{hit} bins (1-9), and location, we can expect N signal events and
 780 B background events. The expected number of excess signal events from dark matter annihilation,

Table 6.2 Summary of dSph observations by each experiment used in this work. A ‘-’ indicates the experiment did not observe the dSph for this study. For Fermi-LAT, the exposure at 1 GeV is given. For HAWC, $|\Delta\theta|$ is the absolute difference between the source declination and HAWC latitude. HAWC is more sensitive to sources with smaller $|\Delta\theta|$. For IACTs, we show the zenith angle range, the total exposure, the energy range, the angular radius θ of the signal or ON region, the ratio of exposures between the background-control (OFF) and signal (ON) regions (τ), and the significance of gamma-ray excess in standard deviations, σ .

Source name	Fermi-LAT	HAWC	H.E.S.S, MAGIC, VERITAS						
	Exposure (10^{11} s m 2)	$ \Delta\theta $ ($^\circ$)	IACT	Zenith ($^\circ$)	Exposure (h)	Energy range (GeV)	θ ($^\circ$)	τ	S (σ)
Boötes I	2.6	4.5	VERITAS	15 – 30	14.0	100–41000	0.10	8.6	-1.0
Canes Venatici I	2.9	14.6	–	–	–	–	–	–	–
Canes Venatici II	2.9	15.3	–	–	–	–	–	–	–
Carina	3.1	–	H.E.S.S.	27 – 46	23.7	310 – 70000	0.10	18.0	-0.3
Coma Berenices	2.7	4.9	H.E.S.S.	47 – 49	11.4	550 – 70000	0.10	14.4	-0.4
Draco	3.8	38.1	MAGIC	5 – 37	49.5	60 – 10000	0.17	1.0	–
			MAGIC	29 – 45	52.1	70 – 10000	0.22	1.0	–
			VERITAS	25 – 40	49.8	120 – 70000	0.10	9.0	-1.0
Fornax	2.7	–	H.E.S.S.	11 – 25	6.8	230 – 70000	0.10	45.5	-1.5
Hercules	2.8	6.3	–	–	–	–	–	–	–
Leo I	2.5	6.7	–	–	–	–	–	–	–
Leo II	2.6	3.1	–	–	–	–	–	–	–
Leo IV	2.4	19.5	–	–	–	–	–	–	–
Leo V	2.4	–	–	–	–	–	–	–	–
Leo T	2.6	–	–	–	–	–	–	–	–
Sculptor	2.7	–	H.E.S.S.	10 – 46	11.8	200 – 70000	0.10	19.8	-2.2
Segue I	2.5	2.9	MAGIC	13 – 37	158.0	60 – 10000	0.12	1.0	-0.5
			VERITAS	15 – 35	92.0	80 – 50000	0.10	7.6	0.7
Segue II	2.7	–	–	–	–	–	–	–	–
Sextans	2.4	20.6	–	–	–	–	–	–	–
Ursa Major I	3.4	32.9	–	–	–	–	–	–	–
Ursa Major II	4.0	44.1	MAGIC	35 – 45	94.8	120 – 10000	0.30	1.0	-2.1
Ursa Minor	4.1	–	VERITAS	35 – 45	60.4	160 – 93000	0.10	8.4	-0.1

781 S , is estimated by convolving Equation (6.1) with HAWC's energy response and pixel point spread
 782 functions. I then compute the test statistic (TS) with the log-likelihood ratio test,

$$\text{TS} = -2 \ln \left(\frac{\mathcal{L}_0}{\mathcal{L}^{\max}} \right) \quad (6.6)$$

784 where \mathcal{L}_0 is the null hypothesis, or no DM emission, likelihood. \mathcal{L}^{\max} is the best fit signal
 785 hypothesis where $\langle \sigma v \rangle$ maximizes the likelihood. We calculate the likelihood of each source and
 786 model, assuming events are Poisson distributed, with

$$\mathcal{L} = \prod_i \frac{(B_i + S_i)^{N_i} e^{-(B_i + S_i)}}{N_i!} \quad (6.7)$$

787 where S_i is the sum of expected number of signal counts. B_i is the number of background counts
 788 observed. N_i is the total number of counts.

789 I also calculate an upper limit on $\langle \sigma v \rangle$ by calculating the 95% confidence level (CL). For the
 790 CL, we define a parameter, TS_{95} , as

$$\text{TS}_{95} \equiv \sum_{\text{bins}} \left[2N \ln \left(1 + \frac{\epsilon S_{\text{ref}}}{B} \right) - 2\epsilon S_{\text{ref}} \right] \quad (6.8)$$

791 where the expected signal counts from a dSph is scaled by ϵ . S_{ref} is the expected number of excess
 792 counts in a bin from DM emission from a dSph with a corresponding annihilation cross-section,
 793 $\langle \sigma v \rangle$. We scan ϵ such that

$$2.71 = \text{TS}_{\max} - \text{TS}_{95} \quad (6.9)$$

794 6.4.2 Glory Duck Joint Likelihood

795 The joint likelihood for the 5-experiment combination was done similarly as Section 6.4.1. We
 796 calculate upper limits on $\langle \sigma v \rangle$ from the TS, Eq. (6.6), and define the likelihood ratio more generally

$$\lambda(\langle \sigma v \rangle | \mathcal{D}_{\text{dSphs}}) = \frac{\mathcal{L}(\langle \sigma v \rangle; \hat{\nu} | \mathcal{D}_{\text{dSphs}})}{\mathcal{L}(\widehat{\langle \sigma v \rangle}; \hat{\nu} | \mathcal{D}_{\text{dSphs}})} \quad (6.10)$$

797 $\mathcal{D}_{\text{dSphs}}$ is the totality of observations across experiments and dSphs. ν are the nuisance parameters
 798 which are the J factors in this study. $\widehat{\langle \sigma v \rangle}$ and $\hat{\nu}$ are the respective estimate that maximize \mathcal{L}
 799 globally. Finally, $\hat{\nu}$ is the set of nuisance parameters that maximize \mathcal{L} for a fixed value of $\langle \sigma v \rangle$.

800 The *complete* joint likelihood, \mathcal{L} that encompasses all observations from all instruments and
 801 dSphs can be factorized into *partial* functions for each dSph l (with $\mathcal{L}_{\text{dSph},l}$) and its J factor (\mathcal{J}_l):

$$\mathcal{L} (\langle \sigma v \rangle; \nu | \mathcal{D}_{\text{dSphs}}) = \prod_{l=1}^{N_{\text{dSphs}}} \mathcal{L}_{\text{dSph},l} (\langle \sigma v \rangle; J_l, \nu_l | \mathcal{D}_l) \times \mathcal{J}_l (J_l | J_{l,\text{obs}}, \sigma_{\log J_l}). \quad (6.11)$$

802 For this study, $N_{\text{dSphs}} = 20$ is the number of dSphs studied. \mathcal{D}_l are the gamma-ray observations
 803 of dSph, l . ν_l are the nuisance parameters modifying the gamma-ray observations of dSph, l ,
 804 but excludes \mathcal{J}_l . \mathcal{J}_l is the J factor for dSph, l , as defined in Equation (6.2), and it is a nuisance
 805 parameter whose value is unknown. $\log_{10} J_{l,\text{obs}}$ and $\sigma_{\log J_l}$ are obtained from fitting a log-normal
 806 function of $J_{l,\text{obs}}$ to the posterior distribution of J_l [48]. $\log_{10} J_{l,\text{obs}}$ and $\sigma_{\log J_l}$ values are provided
 807 in Table 6.1. The term \mathcal{J}_l constraining J_l is written as:

$$\mathcal{J}_l (J_l | J_{l,\text{obs}}, \sigma_{\log J_l}) = \frac{1}{\ln(10) J_{l,\text{obs}} \sqrt{2\pi} \sigma_{\log J_l}} \exp\left(-\frac{(\log_{10} J_l - \log_{10} J_{l,\text{obs}})^2}{2\sigma_{\log J_l}^2}\right). \quad (6.12)$$

808 Both the \mathcal{GS} and \mathcal{B} , displayed in Table 6.1, sets of J factors are used in this analysis. Equation (6.12)
 809 is also normalized, so it can also be interpreted as a probability density function (PDF) for $J_{l,\text{obs}}$.
 810 From Equation (6.1), we can also see that $\langle \sigma v \rangle$ and J_l are degenerate when computing $\mathcal{L}_{\text{dSph},l}$.
 811 Therefore, as noted in [49], it is sufficient to compute $\mathcal{L}_{\text{dSph},l}$ versus $\langle \sigma v \rangle$ for a fixed value of J_l .
 812 We used $J_{l,\text{obs}}(\mathcal{GS})$ reported in Tab. 6.1, in order to perform the profile of \mathcal{L} with respect to J_l .
 813 The degeneracy implies that for any $J'_l \neq J_{l,\text{obs}}$ (in practice in our case we used $J'_l = J_{l,\text{obs}}(\mathcal{B})$ to
 814 compute results from a different set of J factors):

$$\mathcal{L}_{\text{dSph},l} (\langle \sigma v \rangle; J'_l, \nu_l | \mathcal{D}_l) = \mathcal{L}_{\text{dSph},l} \left(\frac{J'_l}{J_{l,\text{obs}}} \langle \sigma v \rangle; J_{l,\text{obs}}, \nu_l | \mathcal{D}_l \right), \quad (6.13)$$

815 which is a straightforward rescaling operation that reduces the computational needs of the profiling
 816 operation since:

$$\mathcal{L} (\langle \sigma v \rangle; \hat{\nu} | \mathcal{D}_{\text{dSphs}}) = \prod_{l=1}^{N_{\text{dSphs}}} \max_{J_l} \left[\mathcal{L}_{\text{dSph},l} (\langle \sigma v \rangle; J_l, \hat{\nu}_l | \mathcal{D}_l) \times \mathcal{J}_l (J_l | J_{l,\text{obs}}, \sigma_{\log J_l}) \right]. \quad (6.14)$$

817 In addition, Eq. (6.13) enables the combination of data from different gamma-ray instruments and
 818 observed dSphs via tabulated values of $\mathcal{L}_{\text{dSph},l}$, or equivalently of λ from Eq. (6.10) as was done in

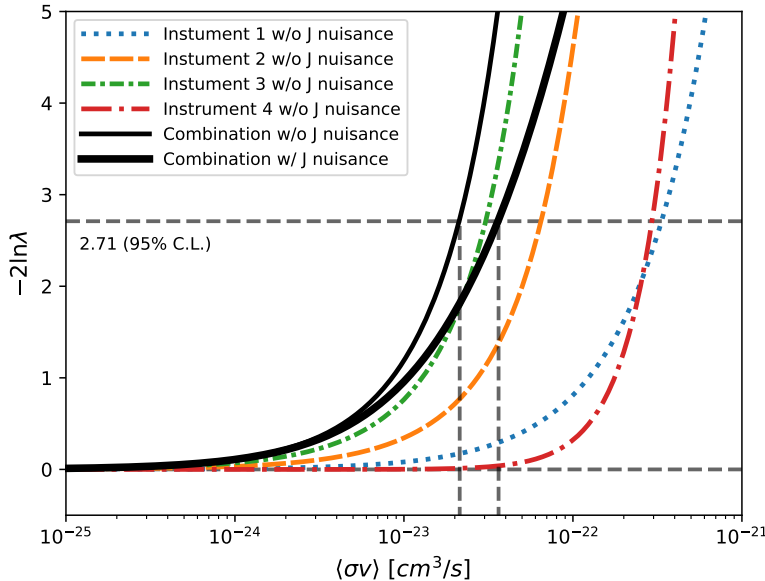


Figure 6.4 Illustration of the combination technique showing a comparison between $-2 \ln \lambda$ provided by four instruments (colored lines) from the observation of the same dSph without any J nuisance and their sum, *i.e.* the resulting combined likelihood (thin black line). According to the test statistics of Equation (6.6), the intersection of the likelihood profiles with the line $-2 \ln \lambda = 2.71$ indicates the 95% C.L. upper limit on $\langle \sigma v \rangle$. The combined likelihood (thin black line) shows a smaller value of upper limit on $\langle \sigma v \rangle$ than those derived by individual instruments. We also show how the uncertainties on the J factor effects the combined likelihood and degrade the upper limit on $\langle \sigma v \rangle$ (thick black line). All likelihood profiles are normalized so that the global minimum $\widehat{\langle \sigma v \rangle}$ is 0. We note that each profile depends on the observational conditions in which a target object was observed. The sensitivity of a given instrument can be degraded and the upper limits less constraining if the observations are performed in non-optimal conditions such as a high zenith angle or a short exposure time.

819 this work, versus $\langle \sigma v \rangle$. $\mathcal{L}_{\text{dSph},l}$ is computed for a fixed value of J_l and profiled with respect to all
 820 instrumental nuisance parameters ν_l , these nuisance parameters are discussed in more detail below.
 821 These values are produced by each detector independently and therefore there is no need to share
 822 sensitive low-level information used to produce them, such as event lists. Figure 6.4 illustrates the
 823 multi-instrument combination technique used in this study with a comparison of the upper limit
 824 on $\langle \sigma v \rangle$ obtained from the combination of the observations of four experiments towards one dSph
 825 versus the upper limit from individual instruments. It also shows graphically the effect of the
 826 J -factor uncertainty on the combined observations.

827 The *partial* joint likelihood function for gamma-ray observations of each dSph ($\mathcal{L}_{\text{dSph},l}$) is

written as the product of the likelihood terms describing the $N_{\text{exp},l}$ observations performed with any of our observatories:

$$\mathcal{L}_{\text{dSph},l} (\langle \sigma v \rangle; J_l, \nu_l | \mathcal{D}_l) = \prod_{k=1}^{N_{\text{exp},l}} \mathcal{L}_{lk} (\langle \sigma v \rangle; J_l, \nu_{lk} | \mathcal{D}_{lk}), \quad (6.15)$$

where each \mathcal{L}_{lk} term refers to an observation of the l -th dSph with associated k -th instrument responses. $N_{\text{exp},l}$ varies from dSph to dSph and can be inferred from Table 6.2.

Each collaboration separately analyzes their data for \mathcal{D}_{lk} corresponding to dSph l and gamma-ray detector k , using as many common assumptions as possible in the analysis. HAWC’s treatment was described earlier in Section 6.4.1 whereas the specifics of the remaining experiments is left to the publication. We compute the values for the likelihood functions \mathcal{L}_{lk} (see Eq. (6.15)) for a fixed value of J_l and profile over the rest of the nuisance parameters ν_{lk} . Then, values of λ from Eq. (6.10) are computed as a function of $\langle \sigma v \rangle$, and shared using a common format. Results are computed for seven annihilation channels, W^+W^- , ZZ , $b\bar{b}$, $t\bar{t}$, e^+e^- , $\mu^+\mu^-$, and $\tau^+\tau^-$ over 62 m_χ values between 5 GeV and 100 TeV provided in [44]. The $\langle \sigma v \rangle$ range is defined between 10^{-28} and $10^{-18} \text{cm}^3 \cdot \text{s}^{-1}$, with 1001 logarithmically spaced values. The likelihood combination, i.e. Equation (6.11), and profile over the J -factor to compute the profile likelihood ratio λ , Equation (6.10), are carried out with two different public analysis software packages, namely `gLike` [50] and `LklCom` [51], that provide the same results [52].

As mentioned previously, each experiment computes the \mathcal{L}_{lk} from Equation (6.10) differently. The remainder of this section highlights the differences in this calculation across the experiments. Four experiments, namely *Fermi*-LAT, H.E.S.S., HAWC and MAGIC, use a binned likelihood to compute the \mathcal{L}_{lk} . For these experiments, for each observation \mathcal{D}_{lk} of a given dSph l carried out using a given gamma-ray detector k , the binned likelihood function is:

$$\mathcal{L}_{lk} (\langle \sigma v \rangle; J_l, \nu_{lk} | \mathcal{D}_{lk}) = \prod_{i=1}^{N_E} \prod_{j=1}^{N_P} \left[\mathcal{P}(s_{lk,ij}(\langle \sigma v \rangle, J_l, \nu_{lk}) + b_{lk,ij}(\nu_{lk}) | N_{lk,ij}) \right] \times \mathcal{L}_{lk,\nu} (\nu_{lk} | \mathcal{D}_{\nu_{lk}}) \quad (6.16)$$

where N_E and N_P are the number of considered bins in reconstructed energy and arrival direction, respectively; \mathcal{P} represents a Poisson PDF for the number of gamma-ray candidate events $N_{lk,ij}$

851 observed in the i -th bin in energy and j -th bin in arrival direction, when the expected number is
 852 the sum of the expected mean number of signal events s_{ij} (produced by DM annihilation) and of
 853 background events b_{ij} ; $\mathcal{L}_{lk,\nu}$ is the likelihood term for the extra ν_{lk} nuisance parameters that vary
 854 from one instrument k to another. The expected counts for signal events s_{ij} for a given dSph l and
 855 detector k is given by:

$$s_{ij}(\langle\sigma\nu\rangle, J) = \int_{E'_{\min,i}}^{E'_{\max,i}} dE' \int_{P'_{\min,j}}^{P'_{\max,j}} d\Omega' \int_0^\infty dE \int_{\Delta\Omega_{tot}} d\Omega \int_0^{T_{\text{obs}}} dt \frac{d^2\Phi(\langle\sigma\nu\rangle, J)}{dEd\Omega} \text{IRF}(E', P' | E, P, t) \quad (6.17)$$

856 where E' and E are the reconstructed and true energies, P' and P the reconstructed and true
 857 arrival directions; $E'_{\min,i}$, $P'_{\min,j}$, $E'_{\max,i}$, and $P'_{\max,j}$ are their lower and upper limits of the i -th
 858 energy bin and the j -th arrival direction bin; T_{obs} is the (dead-time corrected) total observation
 859 time; t is the time along the observations; $d^2\Phi/dEd\Omega$ is the DM flux in the source region (see
 860 Equation (6.1)); and $\text{IRF}(E', P' | E, P, t)$ is the IRF, which can be factorized as the product of the
 861 effective collection area of the detector $A_{\text{eff}}(E, P, t)$, the PDFs for the energy estimator $f_E(E' | E, t)$,
 862 and arrival direction $f_P(P' | E, P, t)$ estimators. Note that for Fermi-LAT, HAWC, MAGIC, and
 863 VERITAS the effect of the finite angular resolution is taken into account through the convolution
 864 of $d\Phi/dEd\Omega$ with f_P in Equation (6.17), whereas in the cases of H.E.S.S. f_P is approximated by a
 865 delta function. This approximation has been made in order to maintain compatibility of the result
 866 with what has been previously published. The difference introduced by this approximation is $< 5\%$
 867 for all considered dSphs. A more comprehensive review of the differences between the analyses of
 868 different instruments can be found in [25].

869 6.5 HAWC Results

870 13 of the 20 dSphs considered for the Glory Duck analysis are within HAWC's field of view.
 871 These dSph are analyzed for emission from DM annihilation according to the likelihood method
 872 described in Section 6.4. The 13 likelihood profiles are then stacked to synthesize a combined
 873 limit on the dark matter cross-section, $\langle\sigma\nu\rangle$. This combination is done for the 7 SM annihilation
 874 channels used in the Glory Duck analysis. Figure 6.5 shows the combined limit for all annihilation
 875 channels with HAWC only observations. We also perform 300 studies of Poisson trials on the

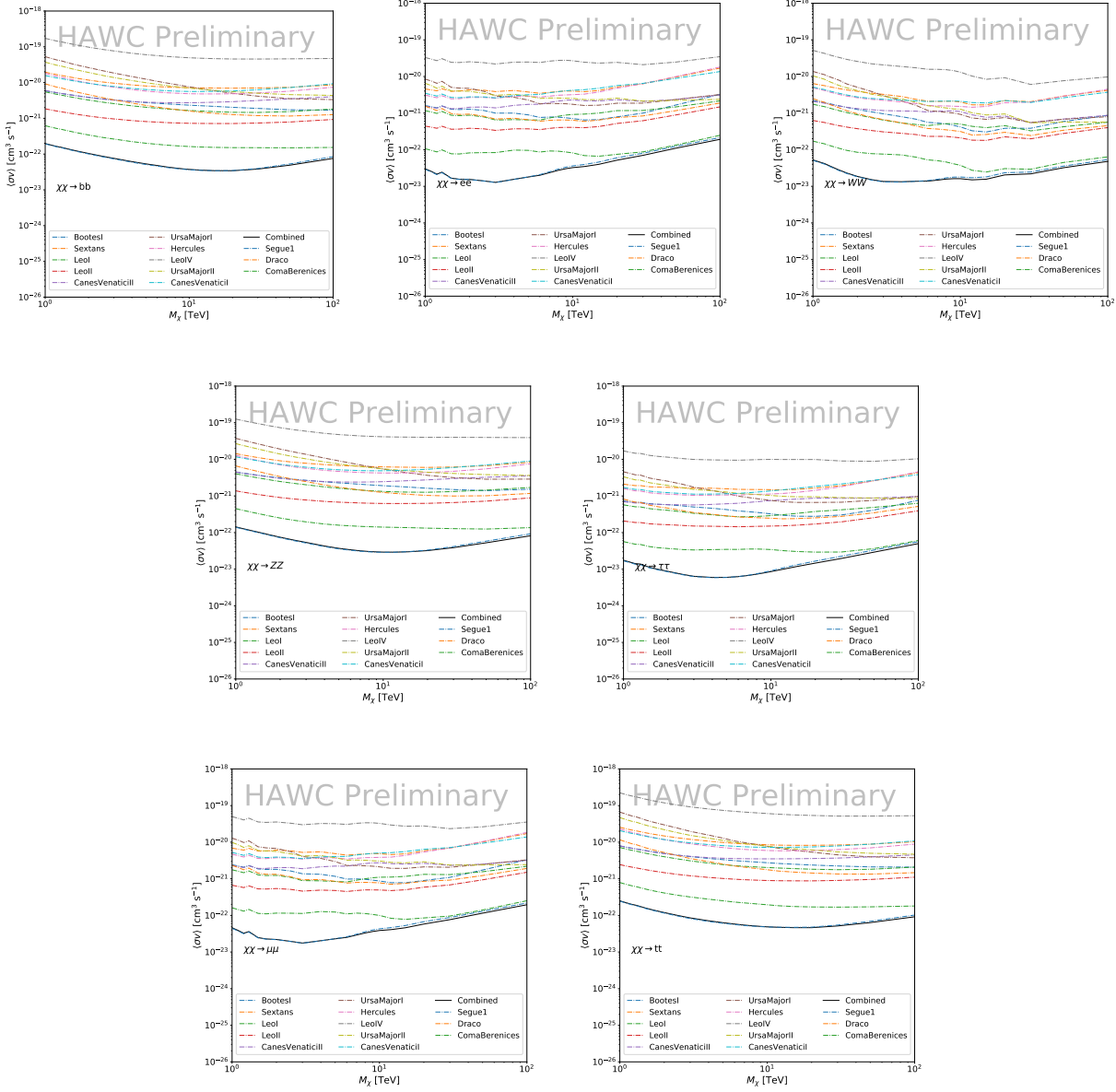


Figure 6.5 HAWC upper limits at 95% confidence level on $\langle\sigma v\rangle$ versus DM mass for seven annihilation channels, using the set of J -factors from Ref. [53]. The solid line represents the observed combined limit. Dashed lines represent limits from individual dSphs.

background. These trials are used to produce HAWC Brazil bands which were shared with the other collaborators for combined Brazil Bands. The results on fitting to HAWC's Poisson trials of the DM hypothesis is shown in Figure 6.7 for all the DM annihilation channels studied for Glory Duck.

No DM was found in HAWC observations. HAWC's limits are dominated by the dSphs Segue1

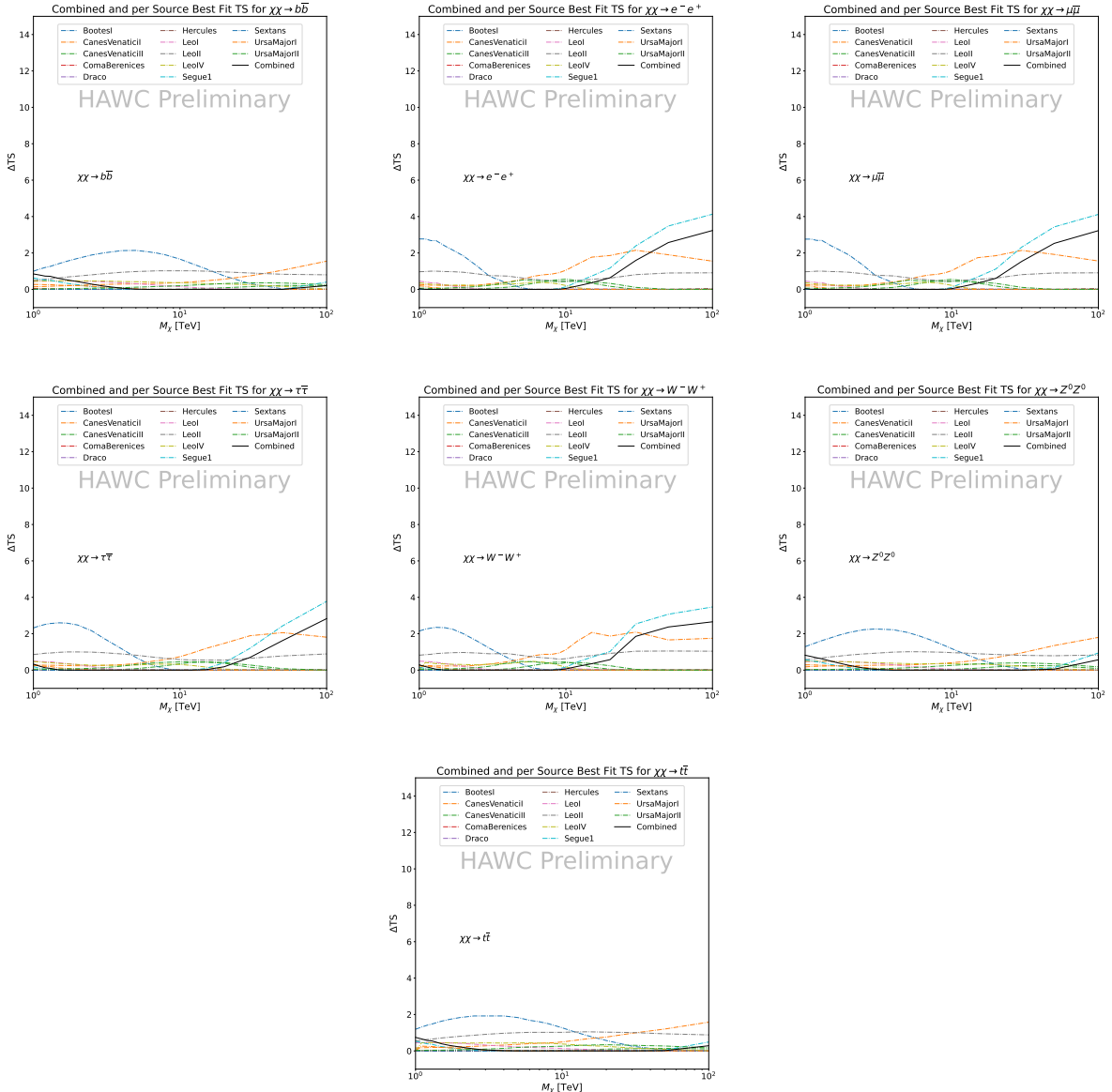


Figure 6.6 HAWC TS values for best fit $\langle \sigma v \rangle$ versus m_χ for seven SM annihilation channels with J factors from \mathcal{GS} . The solid black line shows the combined best fit TS values. The colored, dashed lines are the TS values for each of the 13 sources HAWC studied.

and Coma Berenices. The remaining 11 dSphs do not contribute significantly to the limit because they are at high zenith and/or have much smaller J factors. Even though some remaining dSphs have large J factors, they are towards the edge of HAWC's field of view where HAWC analysis is less sensitive.

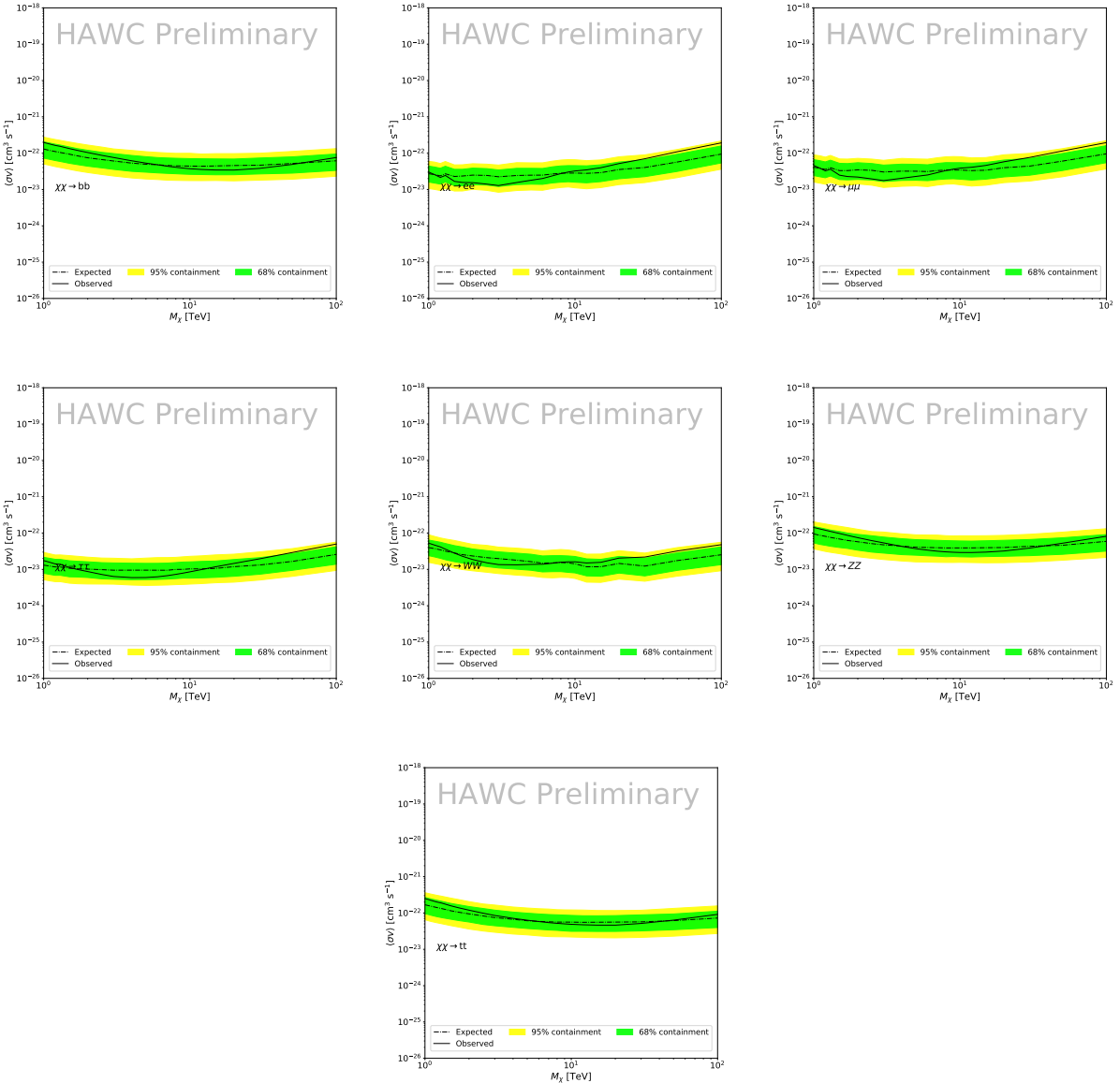


Figure 6.7 HAWC Brazil bands at 95% confidence level on $\langle\sigma v\rangle$ versus DM mass for seven annihilation channels with J -factors from \mathcal{GS} [53]. The solid line represents the combined limit from 13 dSphs. The dashed line is the expected limit. The green band is the 68% containment. The yellow band is the 95% containment.

885 6.6 Glory Duck Combined Results

886 The crux of this analysis is that HAWC's results are combined with 4 other gamma-ray observa-
 887 tories: Fermi-LAT, H.E.S.S., MAGIC, and VERITAS. No significant DM emission was observed
 888 by any of the five instruments. We present the upper limits on $\langle\sigma v\rangle$ assuming seven independent
 889 DM self annihilation channels, namely W^+W^- , Z^+Z^- , $b\bar{b}$, $t\bar{t}$, e^+e^- , $\mu^+\mu^-$, and $\tau^+\tau^-$. The 68%

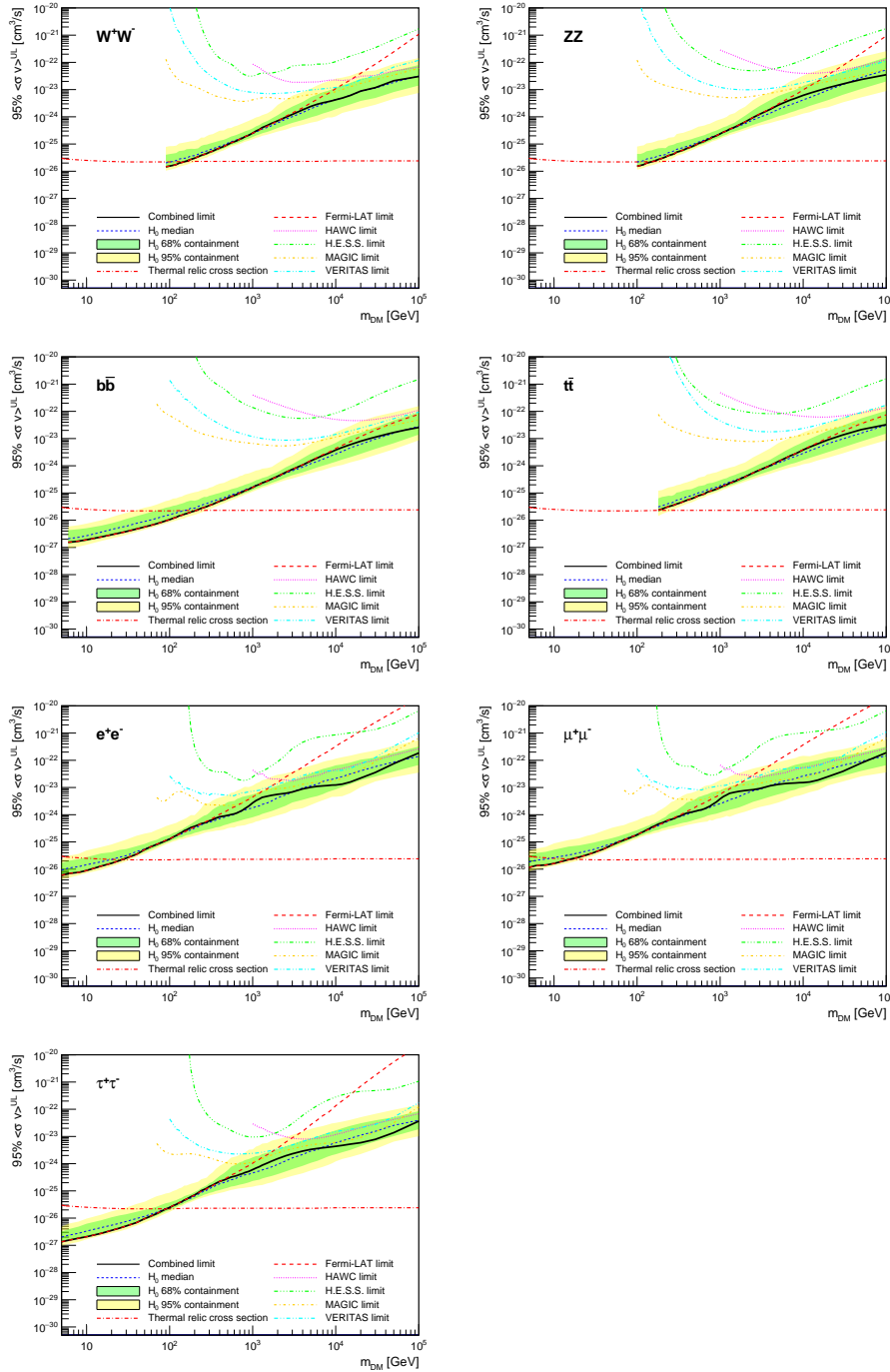


Figure 6.8 Upper limits at 95% confidence level on $\langle\sigma v\rangle$ in function of the DM mass for eight annihilation channels, using the set of J factors from Ref. [53] (\mathcal{GS} set in Table 6.1). The black solid line represents the observed combined limit, the black dashed line is the median of the null hypothesis corresponding to the expected limit, while the green and yellow bands show the 68% and 95% containment bands. Combined upper limits for each individual detector are also indicated as solid, colored lines. The value of the thermal relic cross-section in function of the DM mass is given as the red dotted-dashed line [54].

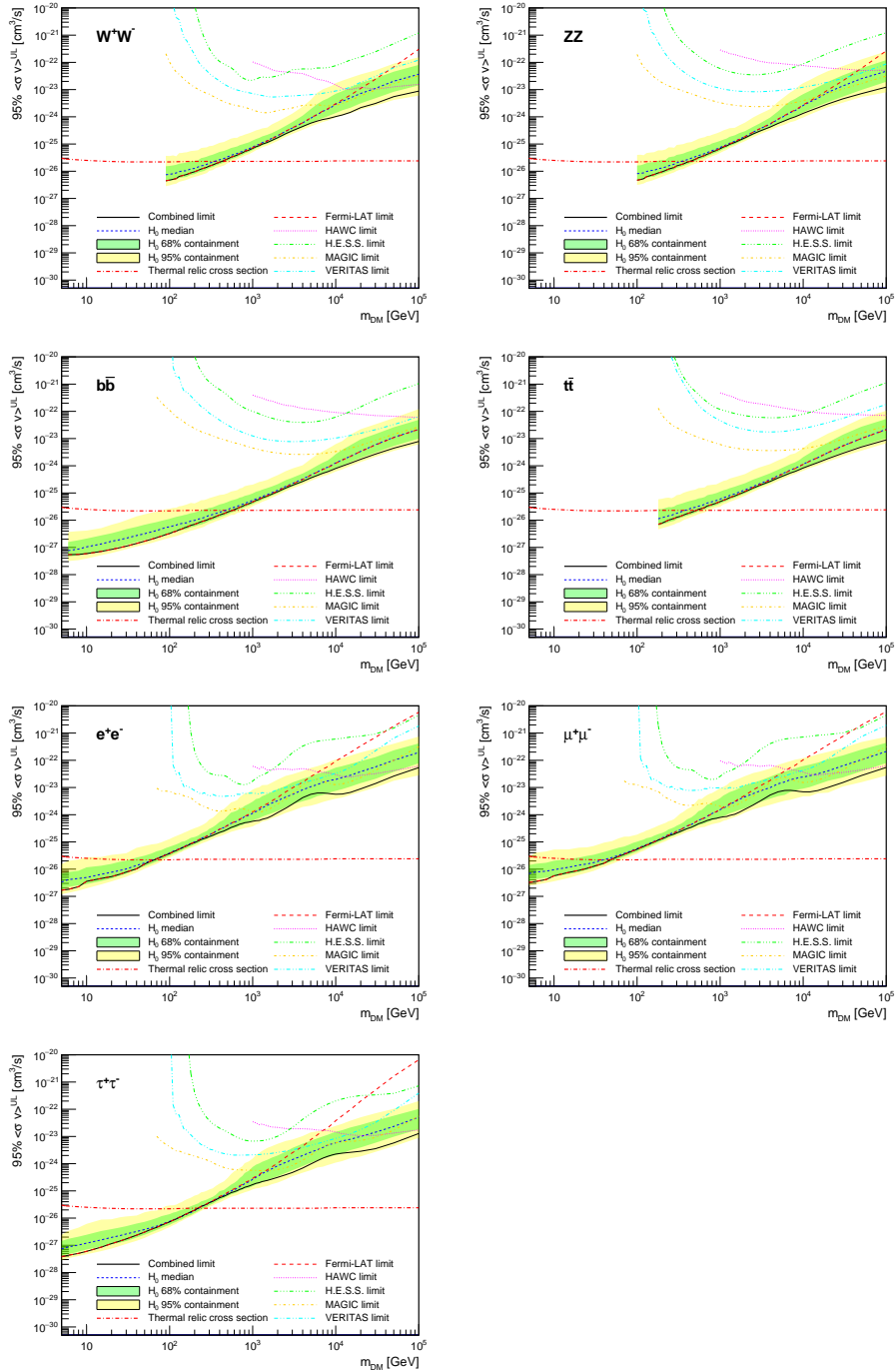


Figure 6.9 Same as Fig. 6.8, using the set of J factors from Ref. [47, 55] (\mathcal{B} set in Table 6.1).

and 95% containment bands are produced from 300 Poisson realizations of the null hypothesis corresponding to each of the combined datasets. These 300 realizations are combined identically to dSph observations. The containment bands and the median are extracted from the distribution of resulting limits on the null hypothesis. These 300 realizations are obtained either by fast simu-

894 lations of the OFF observations, for H.E.S.S., MAGIC, VERITAS, and HAWC, or taken from real
895 observations of empty fields of view in the case of Fermi-LAT [48, 56, 57].

896 The obtained limits are shown in Figure 6.8 for the $\mathcal{G}\mathcal{S}$ set of J -factors [53] and in Figure 6.9
897 for the \mathcal{B} set of J -factors [47, 55]. The combined limits are presented with their 68% and 95%
898 containment bands, and are expected to be close to the median limit when no signal is present.
899 We observe agreement with the null hypothesis for all channels, within 2σ standard deviations,
900 between the observed limits and the expectations given by the median limits. Limits obtained from
901 each detector are also indicated in the figures, where limits for all dSphs observed by the specific
902 instrument have been combined.

903 Below ~ 300 GeV, the *Fermi*-LAT dominates the DM limits for all annihilation channels. From
904 ~ 300 GeV to ~ 2 TeV, *Fermi*-LAT continues to dominate for the hadronic and bosonic DM channels,
905 yet the IACTs (H.E.S.S., MAGIC, and VERITAS) and *Fermi*-LAT all contribute to the limit for
906 leptonic DM channels. For DM masses between ~ 2 TeV to ~ 10 TeV, the IACTs dominate leptonic
907 DM annihilation channels, whereas both the *Fermi*-LAT and the IACTs dominate bosonic and
908 hadronic DM annihilation channels. From ~ 10 TeV to ~ 100 TeV, both the IACTs and HAWC
909 contribute significantly to the leptonic DM limit. For hadronic and bosonic DM, the IACTs and
910 *Fermi*-LAT both contribute strongly.

911 We notice that the limits computed using the \mathcal{B} set of J -factor are always better compared to the
912 ones calculated with the $\mathcal{G}\mathcal{S}$ set. For the W^+W^- , Z^+Z^- , $b\bar{b}$, and $t\bar{t}$ channels, the ratio between the
913 limits computed with the two sets of J -factor is varying between a factor of ~ 3 and ~ 5 depending
914 on the energy, with the largest ratio around 10 TeV. For the channels e^+e^- , $\mu^+\mu^-$, and $\tau^+\tau^-$, the
915 ratio lies between ~ 2 to ~ 6 , being maximum around 1 TeV. Examining Figure 6.16 and Figure 6.17
916 in Section 6.8, these differences are explained by the fact that the \mathcal{B} set provides higher J -factors
917 for the majority of the studied dSphs, with the notable exception of Segue I. The variation on the
918 ratio of the limits for the two sets is due to different dSph dominating the limits depending on the
919 energy. This pushes the range of thermal cross-section which can be excluded to higher mass. This
920 comparison demonstrates the magnitude of systematic uncertainties associated with the choice of

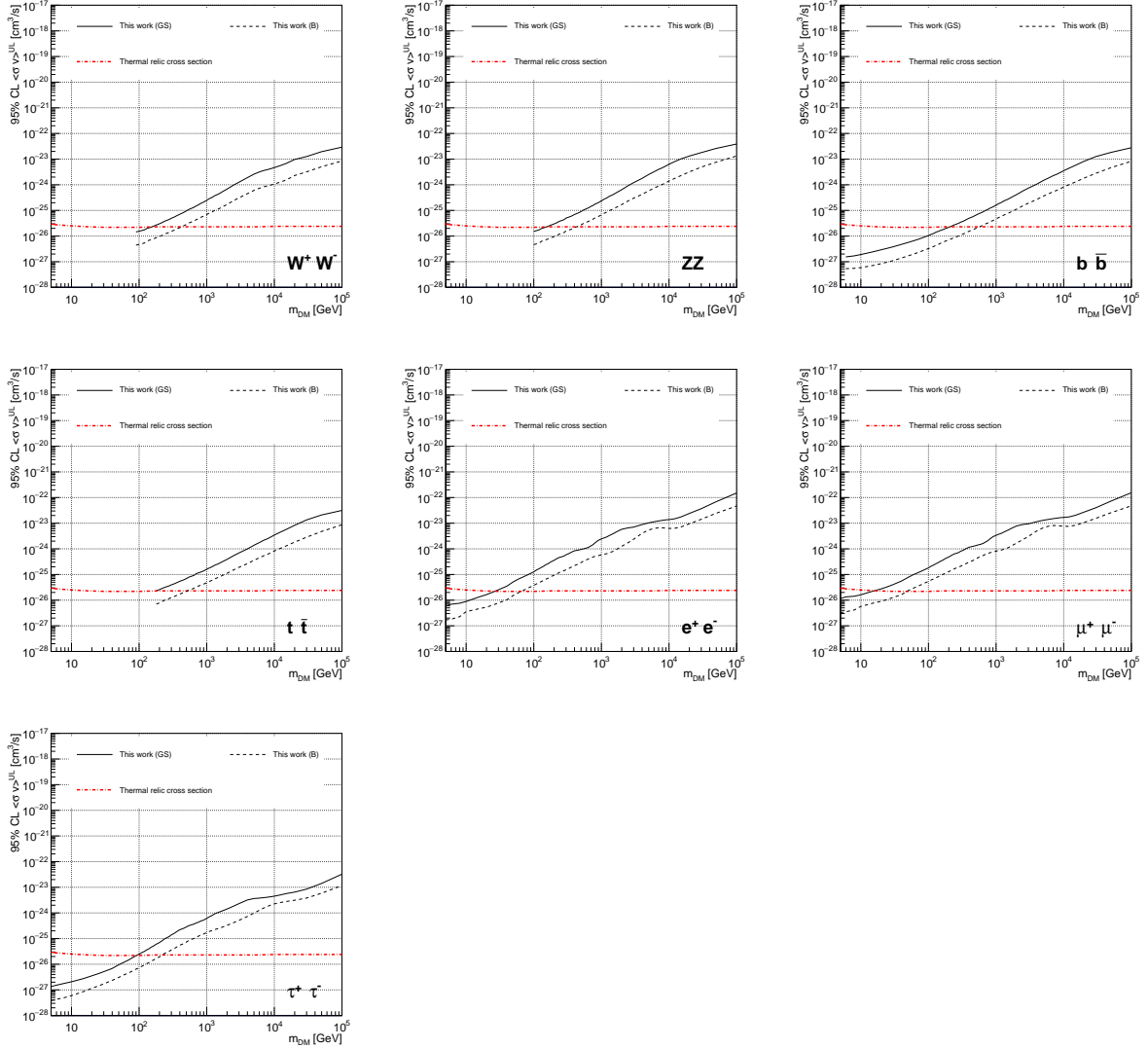


Figure 6.10 Comparisons of the combined limits at 95% confidence level for each of the eight annihilation channels when using the J factors from Ref. [53] (\mathcal{GS} set in Table 6.1), plain lines, and the J factor from Ref. [47, 55] (\mathcal{B} set in Table 6.1), dashed lines. The cross-section given by the thermal relic is also indicated [54].

921 the J -factor

922 This comparison demonstrates the magnitude of systematic uncertainties associated with the
923 choice of the J -factor calculation. The \mathcal{GS} and \mathcal{B} sets present a difference in the limits for all
924 channels of about This difference is explained, see Figure 6.16 and Figure 6.17 in Appendix, by the
925 fact that the \mathcal{B} set provides higher J factors for all dSph except for Segue I. This pushes the range
926 of thermal cross-section which can be excluded to higher mass.

927 **6.7 HAWC Systematics**

928 **6.7.1 Inverse Compton Scattering**

929 The DM-DM annihilation channels produce many high energy electrons regardless of the
930 primary annihilation channel. These high energy electrons can produce high energy gamma-rays
931 through Inverse Compton Scattering (ICS). If this effect is strong, it would change the morphology
932 of the source and increase the total expected gamma-ray counts from any source. The PPPC [44]
933 provides tools in Mathematica for calculating the impact of ICS for an arbitrary location in the
934 sky for a specified annihilation channel. We calculated the change in gamma-ray counts for DM
935 annihilation to primary $e\bar{e}$ for RA and Dec corresponding to Segue1 and Coma Berenices. These
936 dSphs were chosen because they are the strongest contributors to the limit. $e\bar{e}$ was selected because
937 it would have the largest number of high energy electrons. The effect was found to be on the order
938 of 10^{-7} on the gamma-ray spectrum. As a result, this systematic is not considered in our analysis.

939 **6.7.2 Point Source Versus Extended Source Limits**

940 The previous DM search toward dSph approximated the dSphs as point sources [46]. In
941 this analysis, the dSphs are implemented as extended with J-factor distributions following those
942 produced by [53]. The resolution of the cited map is much finer than HAWC's angular resolution.
943 The vast majority of the J-factor distribution is represented on the central HAWC pixel of the dSph
944 spatial map. However, the neighboring 8 pixels are not negligible and contribute to our limit.

945 Figure 6.11 shows a substantial improvement to the limit for Segue1. Fig. 6.12 however showed
946 identical limits. These disparities are best explained by the relative difference in their J-Factors.
947 Both dSphs pass almost overhead the HAWC detector, however Segue1 has the larger J-Factor
948 between the two. Adjacent pixels to the central pixel will therefore contribute to the limits. This is
949 the case for other dSph that are closer to overhead the HAWC detector.

950 Comparison plots for all sources and the combined limit can be found in the sandbox for the
951 Glory Duck project.

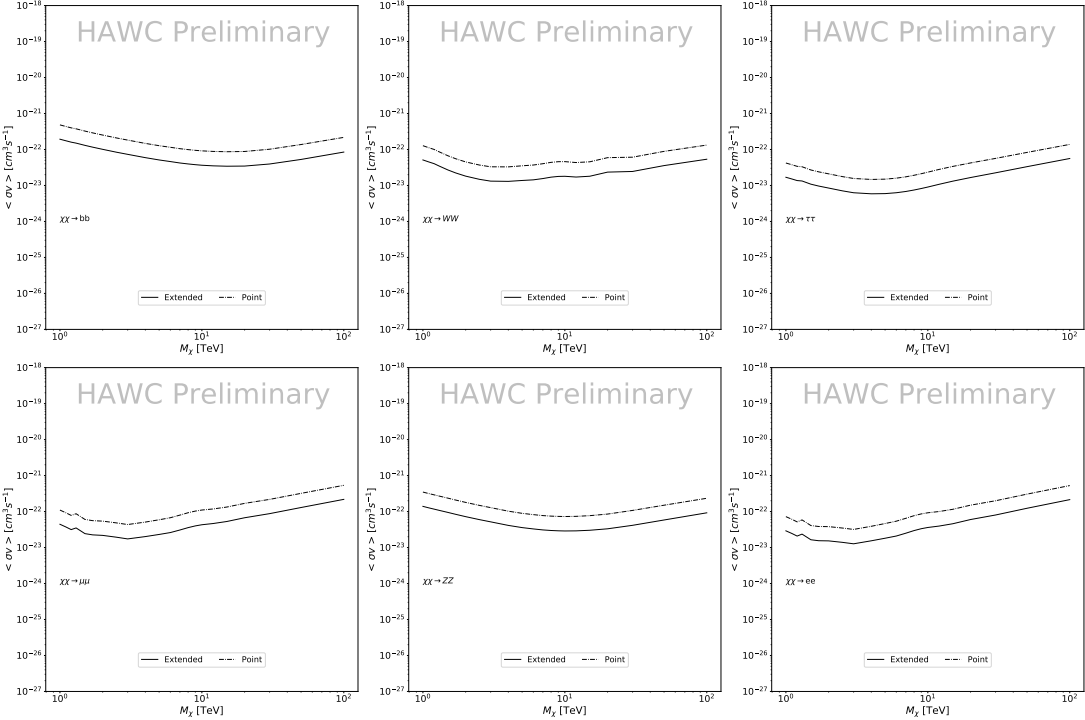


Figure 6.11 Comparisons of the combined limits at 95% confidence level for a point source analysis and extended source using [53] \mathcal{GS} J-factor distributions and PPPC [44] annihilation spectra. Shown are the limits for Segue1 which will have the most significant impact on the combined limit. 6 of the 7 DM annihilation channels are shown. Solid lines are extended source studies. Dashed lines are point source studies. Overall, the extended source analysis improves the limit by a factor of 2.

6.7.3 Impact of Pointing Systematic

During the analysis it was discovered that reconstruction of gamma-rays. Slides describing this systematic can be found [here](#). Shown on the presentation is dependence on the pointing systematic on declination. New spatial profiles were generated for every dSph and limits were computed for the adjusted declination.

Section 6.7.3 demonstrates the impact of this systematic for all DM annihilation channels studied by HAWC. The impact is a tiny improvement, yet mostly identical, to the combined limits.

6.8 J-factor distributions

6.8.1 Numerical integration of \mathcal{GS} maps

It was discovered well after the HAWC analysis was completed that the published tables from \mathcal{GS} [45] quoted median J-factors were computed in a non-trivial manner. The assumption myself

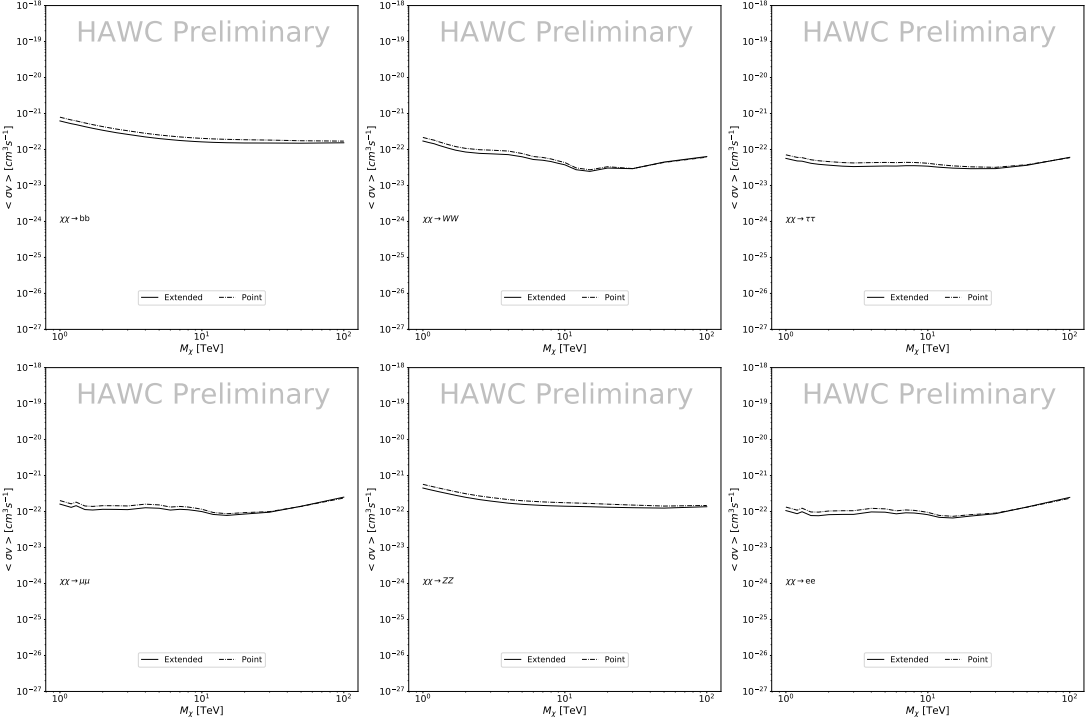


Figure 6.12 Same as Fig. 6.11 on Coma Berenices. This dSph also contributes significantly to the limit. The limits are identical in this case.

and collaborators had been that the published tables represented the J -factor as a function of θ for the best global fit model on a per-source basis. However, this is not the case. Instead, what is published are the best fit model for each dwarf that only considers stars up to the angular separation θ . Therefore, the model is changing for each value of θ for each dwarf. Yet, the introduced features from unique models at each θ are much smaller than the angular resolution of HAWC. It is not expected for these effects to impact the limits and TS greatly as a result.

Median J -factor model profiles were provided by the authors. New maps were generated and analyzed for Segue1 and Coma Berenices. Figure 6.14 shows the differential between maps generated with the method from Section 6.8.1 and from the authors of [45]. These maps were reanalyzed for all SM DM annihilation channels. Upper limits for these channels are shown in Figure 6.15

From Figure 6.15, we can see that the impact of these model difference was no substantial. The observed impact was a fractional effect which is much smaller than the impact from selecting another DM spatial distribution model as was shown in Figure 6.10.

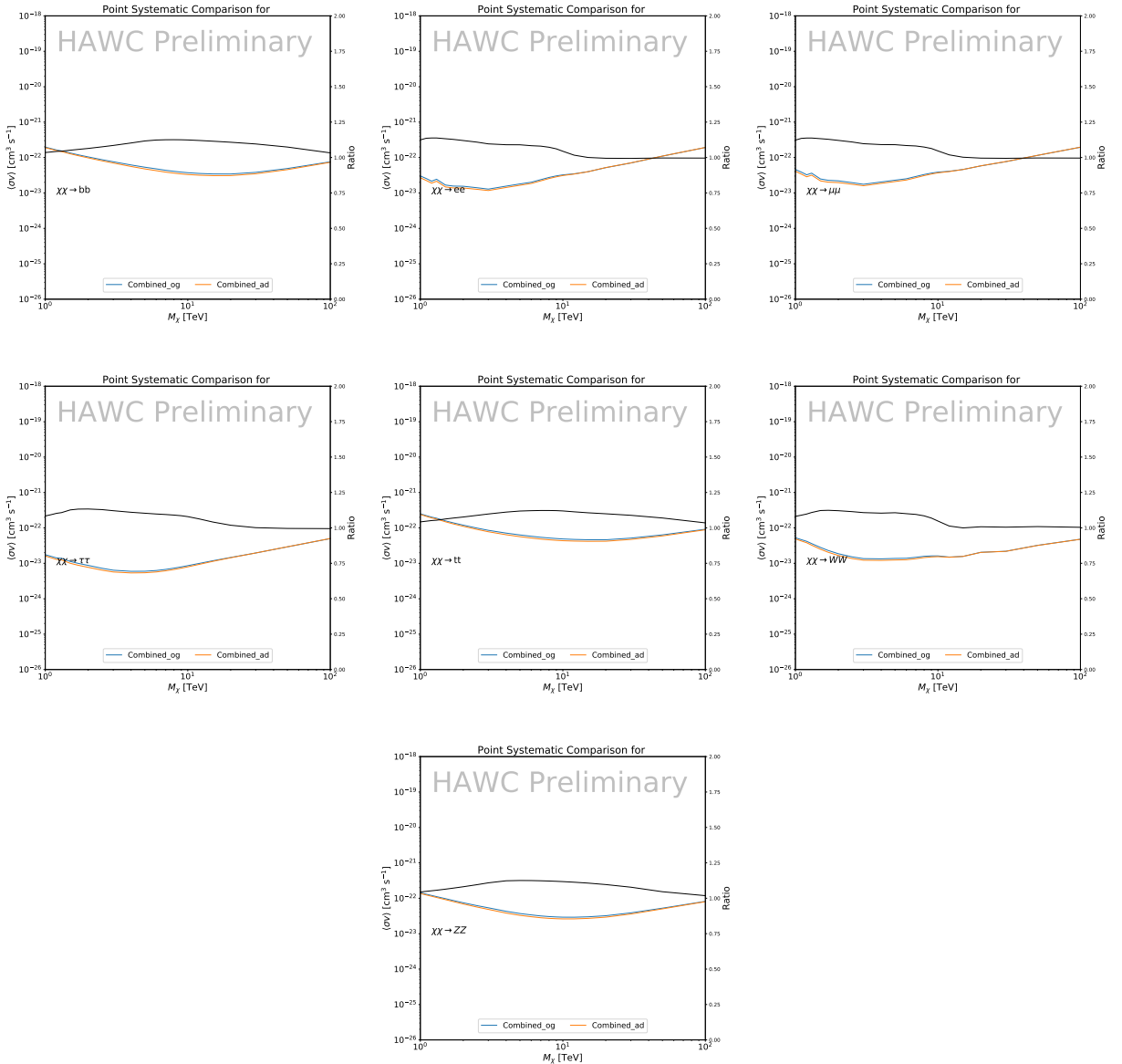


Figure 6.13 Comparison of combined limits when correcting for HAWC's pointing systematic. All DM annihilation channels are shown. The solid black line is the ratio between published limit to the declination corrected limit. The blue solid line or "Combined_og" represented the limits computed for Glory Duck. The solid orange line or "Combined_ad" represented the limits computed after correcting for the pointing systematic.

977 6.8.2 $\mathcal{G}\mathcal{S}$ Versus \mathcal{B} spatial models

978 We show in this appendix a comparison between the J -factors computed by Geringer-Sameth
 979 *et al.* [53] (the $\mathcal{G}\mathcal{S}$ set) and the ones computed by Bonnivard *et al.* [47, 55] (the \mathcal{B} set). The
 980 $\mathcal{G}\mathcal{S}$ J -factors are computed through a Jeans analysis of the kinematic stellar data of the selected

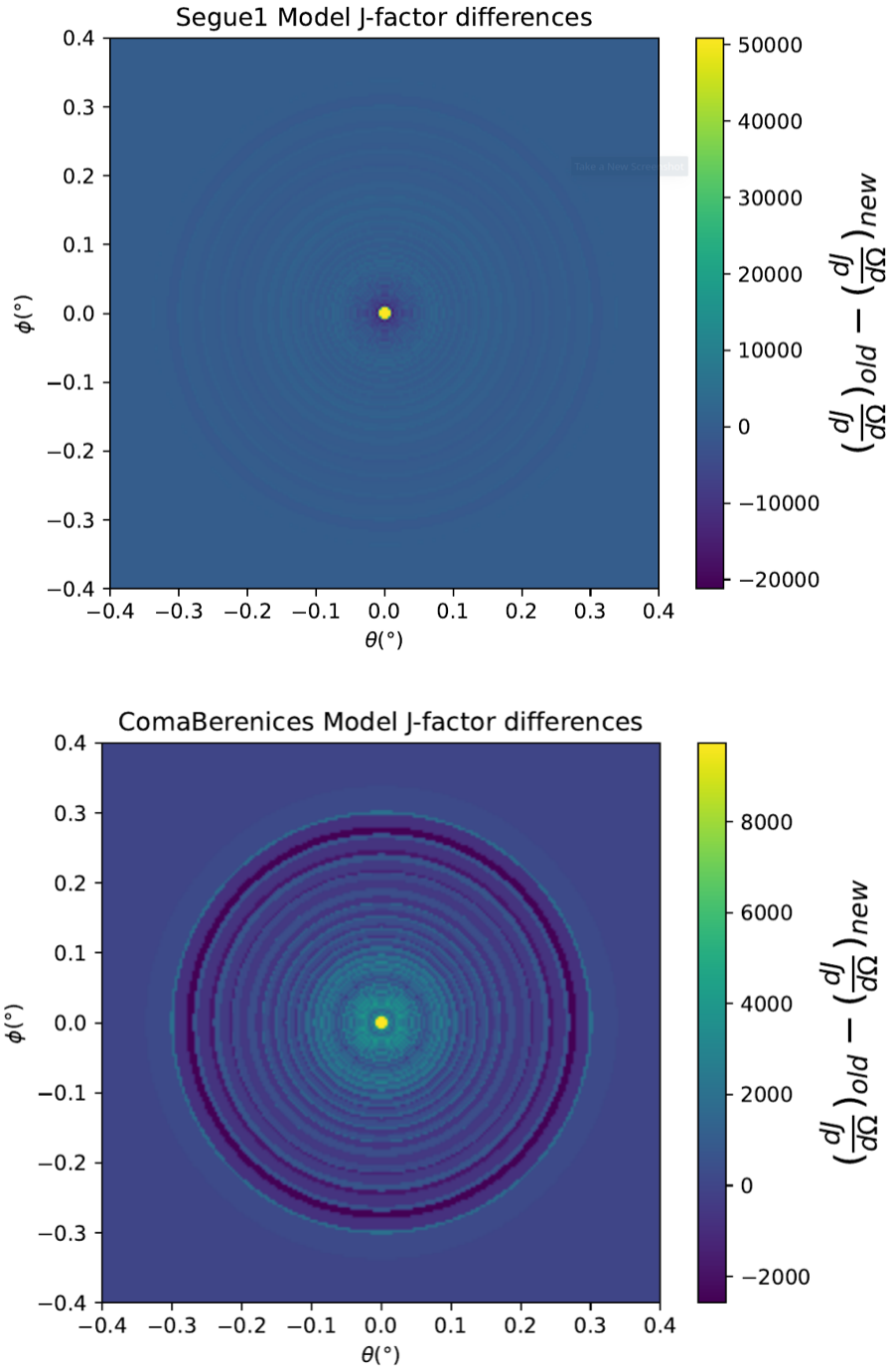


Figure 6.14 Differential map of dJ/Ω from model built in Section 6.8.1 and profiles provided directly from authors. (Top) Differential from Segue1. (bottom) Differential from Coma Berenices. Note that their scales are not the same. Segue1 shows the deepest discrepancies which is congruent with its large uncertainties. Both models show anuli where unique models become apparent.

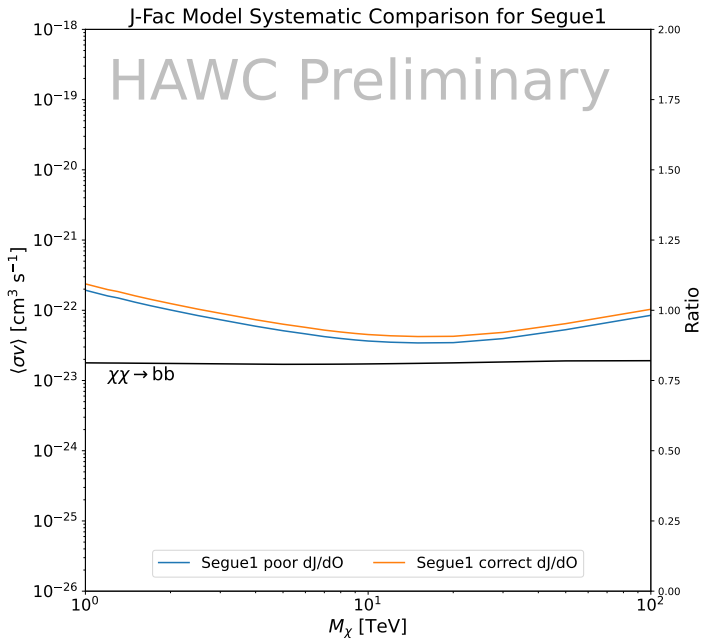
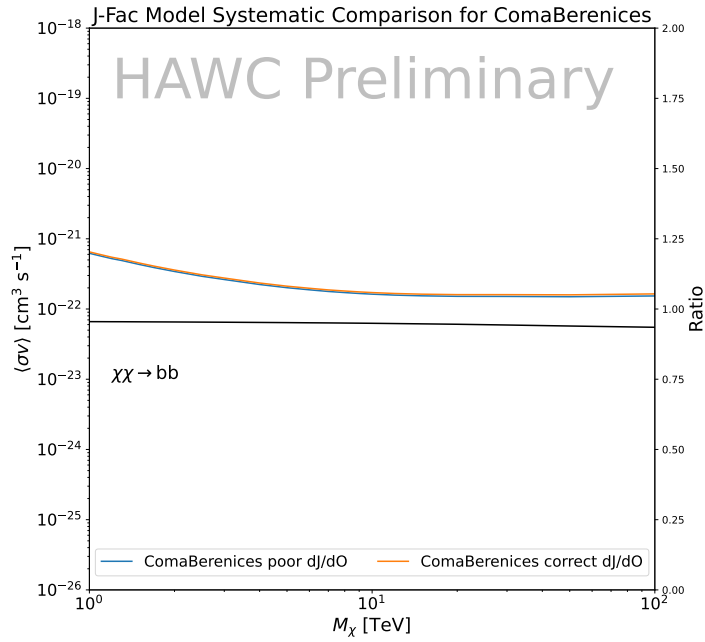


Figure 6.15 HAWC limits for Coma Berenices (top) and Segue1 (bottom) for two different map sets. Blue lines are limits calculated on maps with poor model representation. Orange lines are limits calculated on spatial profiles provided by the authors of [45]. Black line is the ratio of the poor spatial model limits to the corrected spatial models. The left y-axis measures $\langle \sigma v \rangle$ for the blue and orange lines. The right y-axis measures the ratio and is unitless.

981 dSphs, assuming a dynamic equilibrium and a spherical symmetry for the dSphs. They adopted
982 the generalized DM density distribution, known as Zhao-Hernquist, introduced by [58], carrying
983 three additional index parameters to describe the inner and outer slopes, and the break of the
984 density profile. Such a profile parametrization allows the reduction of the theoretical bias from
985 the choice of a specific radial dependency on the kinematic data. In other words, the increase of
986 free parameters with the use of the Zhao-Hernquist profile allows a better description of the mass
987 density distribution of dark matter.

988 In addition, a constant velocity anisotropy profile and a Plummer light profile [59] for the stellar
989 distribution were assumed. The velocity anisotropy profile depends on the radial and tangential
990 velocity dispersion. However, its determination remains challenging since only the line-of-sight
991 velocity dispersion can be derived from velocity measurements. Therefore, the parametrization of
992 the anisotropy profile is obtained from simulated halos (see [60] for more details). They provide the
993 values of the J -factors of regions extending to various angular radius up to the outermost member
994 star.

995 The \mathcal{B} J -factors were computed through a Jeans analysis taking into account the systematic
996 uncertainties induced by the DM profile parametrization, the radial velocity anisotropy profile, and
997 the triaxiality of the halo of the dwarf galaxies. They performed a more complete study of the dSph
998 kinematics and dynamics than \mathcal{GS} for the determination of the J -factor. Conservative values of the
999 J -factors where obtained using an Einasto DM density profile [61], a realistic anisotropy profile
1000 known as the Baes & Van Hese profile [62] which takes into account that the inner regions can be
1001 significantly non-isotropic, and a Zhao-Hernquist light profile [58].

1002 For both sets, J -factor values are provided for all dSphs as a function of the radius of the
1003 integration region [53, 47, 55]. Table 6.1 shows the heliocentric distance and Galactic coordinates
1004 of the twenty dSphs, together with the two sets of J -factor values integrated up to the outermost
1005 observed star for \mathcal{GS} and the tidal radius for \mathcal{B} . Both J -factor sets were derived through a Jeans
1006 analysis based on the same kinematic data, except for Draco where the measurements of [63] have
1007 been adopted in the computation of the \mathcal{B} value. The computations for producing the \mathcal{GS} and \mathcal{B}

1008 samples differ in the choice of the DM density, velocity anisotropy, and light profiles, for which the
1009 set \mathcal{B} takes into account some sources of systematic uncertainties.

1010 Figure 6.16 and Figure 6.17 show the comparisons for the J -factor versus the angular radius
1011 for each of the 20 dSphs used in this study. The uncertainties provided by the authors are also
1012 indicated in the figures. For the \mathcal{GS} set, the computation stops at the angular radius corresponding
1013 to the outermost observed star, while for the \mathcal{B} set, the computation stops at the angular radius
1014 corresponding to the tidal radius.

1015 6.9 Discussion and Conclusions

1016 In this multi-instrument analysis, we have used observations of 20 dSphs from the gamma-ray
1017 telescopes Fermi-LAT, H.E.S.S., MAGIC, VERITAS, and HAWC to perform a collective DM
1018 search annihilation signals. The data were combined across sources and detectors to significantly
1019 increase the sensitivity of the search. We have observed no significant deviation from the null, no
1020 DM hypothesis, and so present our results in terms of upper limits on the annihilation cross-section
1021 for seven potential DM annihilation channels.

1022 Fermi-LAT brings the most stringent constraints for continuum channels below approximately
1023 1 TeV. The remaining detectors dominate at higher energies. Overall, for multi-TeV DM mass,
1024 the combined DM constraints from all five telescopes are 2-3 times stronger than any individual
1025 telescope for multi-TeV DM.

1026 Derived from observations of many dSphs, our results produce robust limits given the DM
1027 content of the dSphs is relatively well constrained. The obtained limits span the largest mass
1028 range of any WIMP DM search. Our combined analysis improves the sensitivity over previously
1029 published results from each detector which produces the most stringent limits on DM annihilation
1030 from dSphs. These results are based on deep exposures of the most promising known dSphs with
1031 the currently most sensitive gamma-ray instruments. Therefore, our results constitute a legacy of
1032 a generation of gamma-ray instruments on WIMP DM searches towards dSphs. Our results will
1033 remain the reference in the field until a new generation of more sensitive gamma-ray instruments
1034 begin operations, or until new dSphs with higher J -factors are discovered.

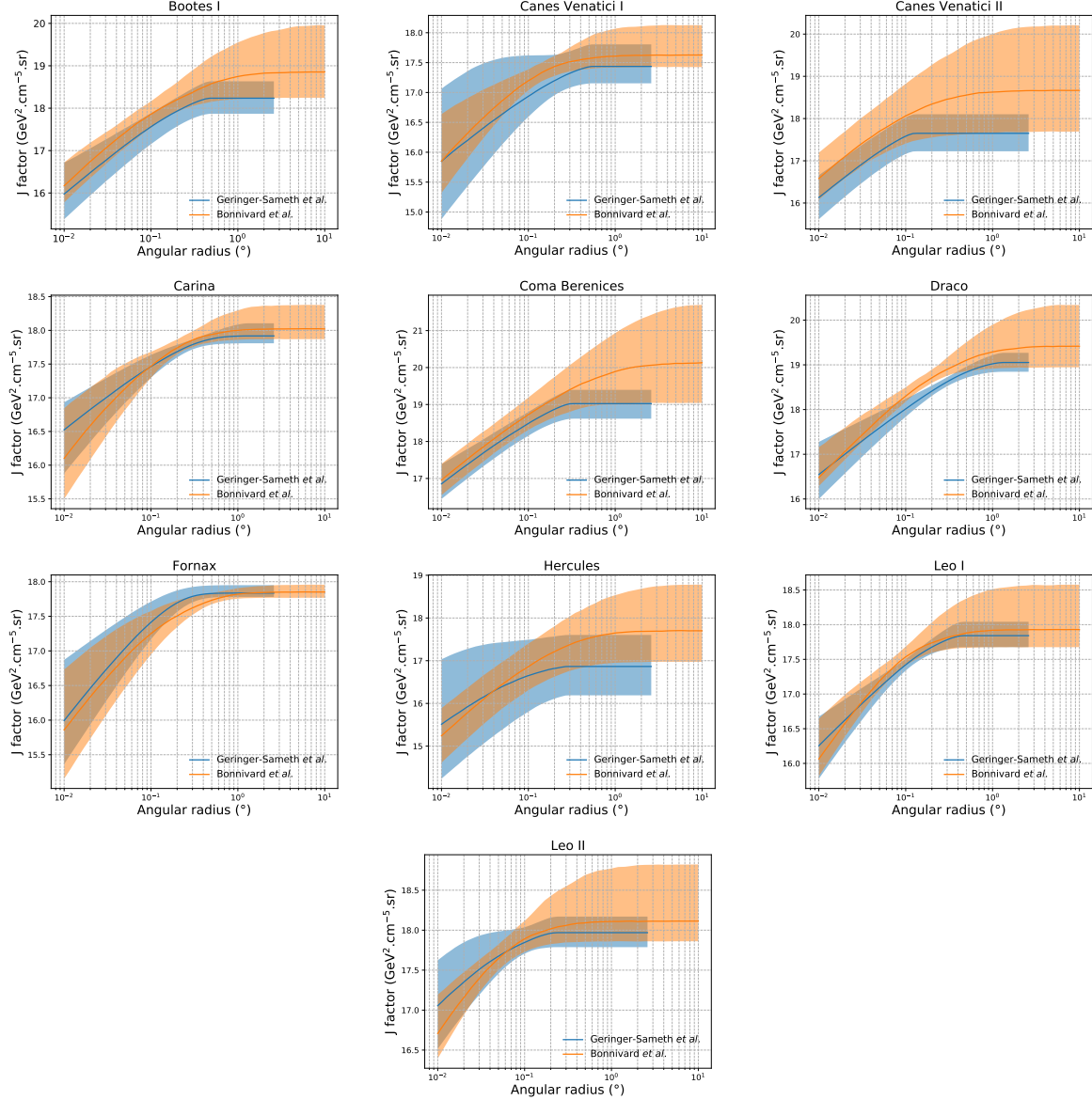


Figure 6.16 Comparisons between the J -factors versus the angular radius for the computation of J factors from Ref. [53] (\mathcal{GS} set in Table 6.1) in blue and for the computation from Ref. [47, 55] (\mathcal{B} set in Tab. 6.1) in orange. The solid lines represent the central value of the J -factors while the shaded regions correspond to the 1σ standard deviation.

1035 This analysis serves as a proof of concept for future multi-instrument and multi-messenger
 1036 combination analyses. With this collaborative effort, we have managed to sample over four orders
 1037 in magnitude in gamma-ray energies with distinct observational techniques. Determining the nature
 1038 of DM continues to be an elusive and difficult problem. Larger datasets with diverse measurement
 1039 techniques could be essential to tackling the DM problem. A future collaboration using similar

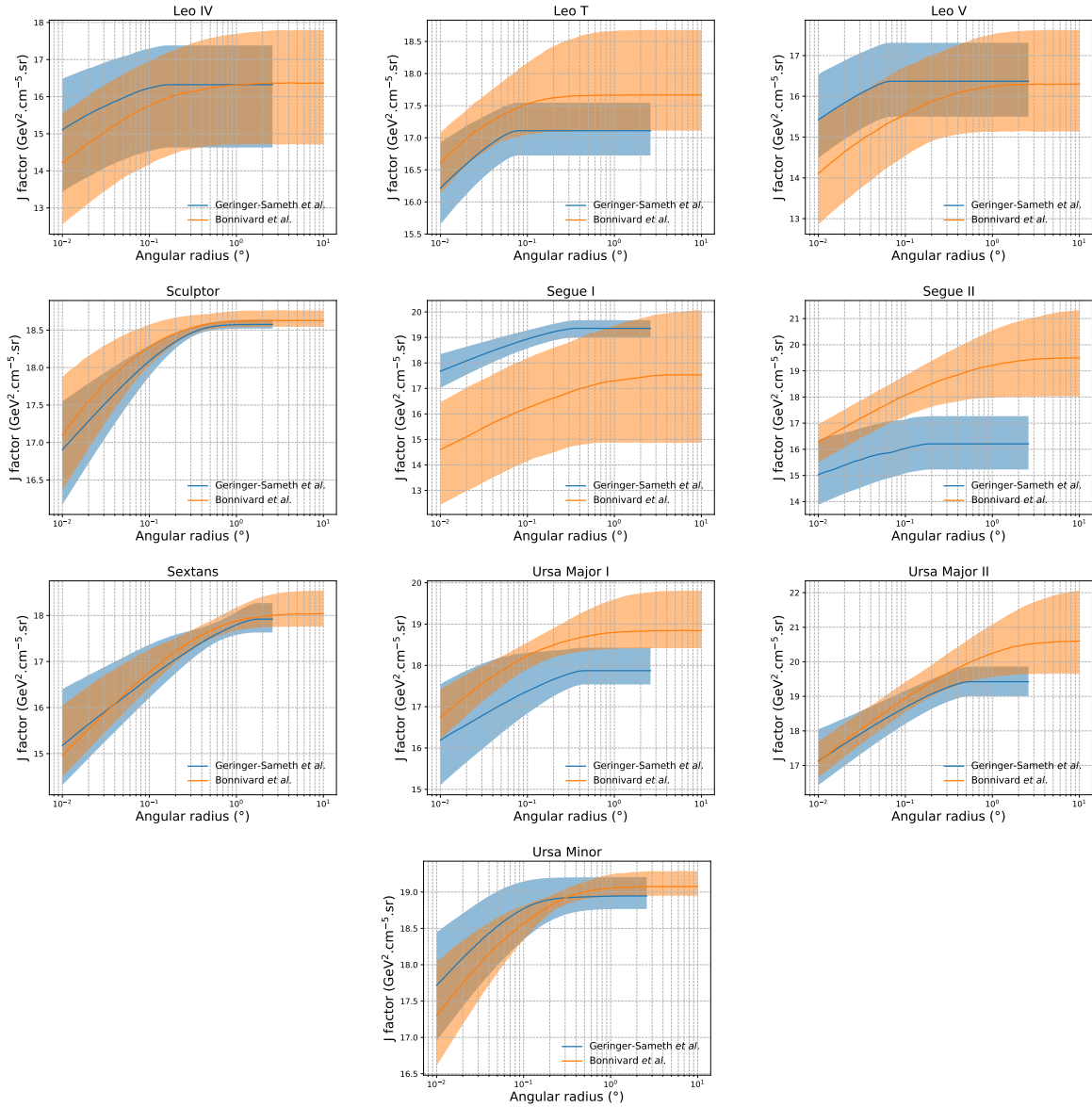


Figure 6.17 Comparisons between the J -factors versus the angular radius for the computation of J factors from Ref. [53] (\mathcal{GS} set in Tab. 6.1) in blue and for the computation from Ref. [47, 55] (\mathcal{B} set in Tab. 6.1) in orange. The solid lines represent the central value of the J -factors while the shaded regions correspond to the 1σ standard deviation.

1040 techniques as the ones described in this paper could grow even beyond gamma rays. The models we
 1041 used for this study include annihilation channels with neutrinos in the final state. Advanced studies
 1042 could aim to merge our results with those from neutrino observatories with large data sets. Efforts
 1043 are already underway to add data from the IceCube, ANTARES, and KM3NeT observatories to
 1044 these gamma-ray results.

1045 From this work, a selection of the best candidates for observations, according to the latest
1046 knowledge on stellar dynamics and modelling techniques for the derivation of the J -factors on
1047 the potential dSphs targets, is highly desirable at the time that new experiments are starting their
1048 dark matter programs using dSphs. Given the systematic uncertainty inherent to the derivation of
1049 the J -factors, an informed observational strategy would be to select both objects with the highest
1050 J -factors that could lead to DM signal detection, and objects with robust J -factor predictions, i.e.
1051 with kinematic measurements on many bright stars, which would strengthen the DM interpretation
1052 reliability of the observation outcome.

1053 This analysis combines data from multiple telescopes to produce strong constraints on astro-
1054 physical objects. From this perspective, these methods can be applied beyond just DM searches.
1055 Almost every astrophysical study can benefit from multi-telescope, multi-wavelength gamma-ray
1056 studies. We have enabled these telescopes to study the cosmos with greater precision and detail.
1057 Many astrophysical searches can benefit from multi-instrument gamma-ray studies, for which our
1058 analysis lays the foundation.

CHAPTER 7

MULTITHREADING HAWC ANALYSES FOR DARK MATTER SEARCHES

7.1 Introduction

HAWC's current software suite, plugins to 3ML, does not fully utilize computational advancements of recent decades. Said advancements include the proliferation of Graphical Processing Units (GPUs), and multithreading on multi-core processors. The analysis described in chapter 6 took up to 3 months of human time waiting for the full gambit of data analysis and simulation of background to run. Additionally, with the addition of a 2D binning scheme, f_{hit} and NN, the expected compute time is expected to grow further. Although excessive computing time was, in part, from an intense use of a shared computing cluster, it was evident that there was room for improvement. In HAWC's next generation dSph DM search, I decided to develop codes that would utilize the multi-core processors on modern high performance computing clusters. The results of this work are featured in this chapter and brought a human timing improvement to computation that scales as $1/N$ where N is the number of threads.

7.2 Dataset and Background

This section enumerates the data and background methods used for HAWC's multi-threaded study of dSphs. Section 7.2.1 and Section 7.2.2 are most useful for fellow HAWC collaborators looking to replicate a multithreaded dSph DM search.

7.2.1 Itemized HAWC files

- Detector Resolution: `refit-Pass5-Final-NN-detRes-zenith-dependent.root`
- Data Map: `Pass5-Final-NN-maptree-ch103-ch1349-zenith-dependent.root`
- Spectral Dictionary: `HDMspectra_dict_gamma.npy`

7.2.2 Software Tools and Development

This analysis was performed using HAL and 3ML [42, 43] in Python version 3. I built software in collaboration with Michael Martin and Letrell Harris to implement the *Dark Matter Spectra from*

1083 *the Electroweak to the Planck Scale* (HDM) [64] and dSphs spatial model from [65] for HAWC
1084 analysis. A NumPy dictionary of HDM was made for Py3. The corresponding Python3 file is
1085 `HDMspectra_dict_gamma.npy`. These files can also be used for decay channels and tools are
1086 provided in HDM’s [git repository](#) [64]. The analysis was performed using the Neural Network
1087 energy estimator for Pass 5.F. A description of this estimator was provided in chapter 4. **TODO:**
1088 **define a subsection when it’s written** All other software used for data analysis, DM profile generation,
1089 and job submission to SLURM are also kept in my sandbox in the [Dark Matter HAWC](#) project.
1090 The above repository also incorporates the model inputs used previously in Glory Duck, described
1091 in chapter 6

1092 7.2.3 Data Set and Background Description

1093 The HAWC data maps used for this analysis contain 2565 days of data between runs 2104 (1094 **TODO: Day start**) and 7476 (**TODO: day end**). They were generated from pass 4.0 reconstruction.
1095 The analysis is performed using the NN energy estimator with bin list:

1096 B1C0Ea, B1C0Eb, B1C0Ec, B1C0Ed, B1C0Ee, B2C0Ea, B2C0Eb, B2C0Ec, B2C0Ed, B2C0Ee,
1097 B3C0Ea, B3C0Eb, B3C0Ec, B3C0Ed, B3C0Ee, B3C0Ef, B4C0Eb, B4C0Ec, B4C0Ed, B4C0Ee,
1098 B4C0Ef, B5C0Ec, B5C0Ed, B5C0Ee, B5C0Ef, B5C0Eg, B6C0Ed, B6C0Ee, B6C0Ef, B6C0Eg,
1099 B6C0Eh, B7C0Ee, B7C0Ef, B7C0Eg, B7C0Eh, B7C0Ei, B8C0Ee, B8C0Ef, B8C0Eg, B8C0Eh,
1100 B8C0Ei, B8C0Ej, B9C0Ef, B9C0Eg, B9C0Eh, B9C0Ei, B9C0Ej, B10C0Eg, B10C0Eh,
1101 B10C0Ei, B10C0Ej, B10C0Ek, B10C0El

1102 Bin 0 was excluded as it has substantial hadronic contamination and poor angular resolution.

1103 Background considerations and source selection was identical to Section 6.2, and no additional
1104 arguments are provided here. Many of the HAWC systematics explored in Section 6.7 also apply
1105 for this DM search and are not added upon here.

1106 7.3 Analysis

1107 The analysis and its systematics are almost identical to Section 6.3. Importantly, we use the
1108 same Equation (6.1) and Equation (6.2) for estimating the gamma-ray flux at HAWC from our

sources. We add on to the previous study with a search for DM decay. The flux equations for DM decay are

$$\frac{d\Phi_\gamma}{dE_\gamma} = \frac{1}{4\pi\tau m_\chi} \frac{dN_\gamma}{dE_\gamma} \times \int_{\text{source}} d\Omega \int_{l.o.s} dl \rho_\chi dl(r, \theta') \quad (7.1)$$

with a new quantity, the D factor, defined as

$$D = \int d\Omega \int_{l.o.s} dl \rho_\chi(r, \theta') \quad (7.2)$$

Software was written to accomodate DM decay from dSphs, however decay profiles were not received from $\mathcal{L}\mathcal{S}$ by the time of writing this tehsis.

7.3.1 $\frac{dN_\gamma}{dE_\gamma}$ - Particle Physics Component

For these spectra, we import HDM with Electroweak (EW) corrections and additional corrections for neutrinos above the EW scale [64]. The spectrum is implemented as a model script in astromodels for 3ML. A comprehensive description of EW corrections and neutrino considerations are provided later in [TODO: refeance MM nu duck](#).

Figure 7.1 demonstrates the impact of changes from HDM on DM annihilation to W bosons. A class in astromodels was developed to include HDM and is aptly named `HDMspectra` within `DM_models.py`. The SM DM annihilation channels studied here are $\chi\chi \rightarrow:$

$$e^+e^-, \mu^+\mu^-, \tau^+\tau^-, b\bar{b}, t\bar{t}, gg, W^+W^-, ZZ, c\bar{c}, u\bar{u}, d\bar{d}, s\bar{s}, \nu_e\bar{\nu}_e, \nu_\mu\bar{\nu}_\mu, \nu_\tau\bar{\nu}_\tau, \gamma\gamma, hh.$$

For $\gamma\gamma$ and ZZ , a substantial fraction of the signal photons are expected to have total energy equal m_χ [64]. This introduces a δ -function that is much narrower than the energy resolution of the HAWC detector. To ensure that this feature is not lost in the likelihood fits, the 'line' feature is convolved with a gaussian kernel with a 1σ width of $0.05 \cdot m_\chi$ and total kernel window of $\pm 4\sigma$. This differs from HAWC's previous line study where 30% of HAWC's energy resolution was used for the kernel [66]. The NN energy estimator's strength compared to f_{hit} at low gamma-ray energy enables smaller resolutions in addition to low energy tails in the spectral models [64]. $\chi\chi \rightarrow \gamma\gamma$ and ZZ spectral hypotheses are shown in Figure 7.2. Spectral models for the remaining annihilation channels are plotted for each m_χ in Figure B.1.

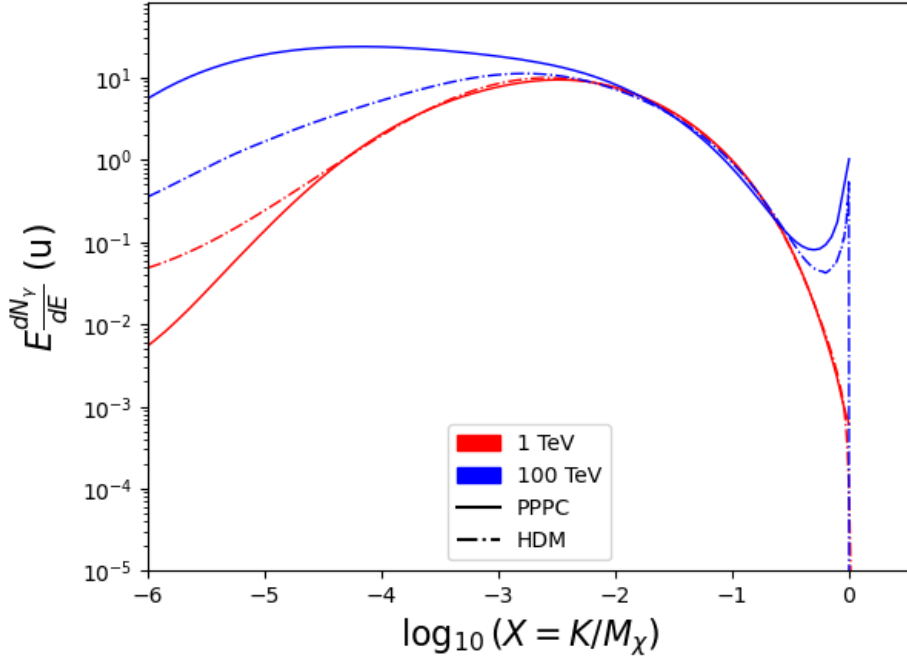


Figure 7.1 Difference between spectral hypotheses from PPPC [44] and HDM [64]. Shown is the expected DM annihilation spectrum for $\chi\chi \rightarrow W^-W^+$. Solid lines are spectral models with EW corrections from the PPPC. Dash-dot lines are spectral models from HDM. Red lines are models for $M_\chi = 1$ TeV. Blue lines represent models for $M_\chi = 100$ TeV.

1132 7.3.2 *J* and *D*- Astrophysical Components

1133 The J-factor profiles for each source are imported from Louis Strigari et al. (referred to with
 1134 $\mathcal{L}S$) [65]. Profiles in $\frac{dJ}{d\Omega}(\theta)$ and $\frac{dD}{d\Omega}(\theta)$ up to $\theta = 0.5^\circ$ were provided directly from the authors.
 1135 Map generation from these profiles were almost identical to Section 6.3.2 except that a higher order
 1136 trapezoidal integral was used for the normalization of the square, uniformly-spaced map:

$$p^2 \cdot \sum_{i=0}^N \sum_{j=0}^M w_{i,j} \frac{d\mathcal{K}}{d\Omega}(\theta_{i,j}, \phi_{i,j}) \quad (7.3)$$

1137 \mathcal{K} is either J or D for the spatial distributions of annihilation or decay respectively. p is the angular
 1138 side of one pixel in the map. $w_{i,j}$ is a weight assigned the following ways:

1139 $w_{i,j} = 1$ if $(\theta_{i,j}, \phi_{i,j})$ is fully within the region of integration

1140 $w_{i,j} = 1/2$ if $(\theta_{i,j}, \phi_{i,j})$ is on an edge of the region of integration

1141 $w_{i,j} = 1/4$ if $(\theta_{i,j}, \phi_{i,j})$ is on a corner of the region of integration

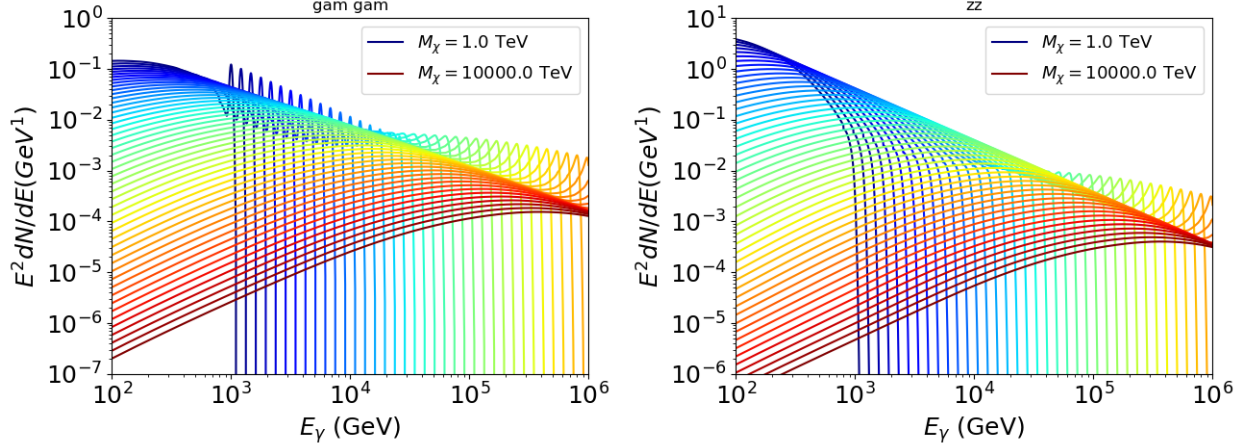


Figure 7.2 Photon spectra for $\chi\chi \rightarrow \gamma\gamma$ (left) and $\chi\chi \rightarrow ZZ$ (right) after gaussian convolution of line features. Both spectra have δ -features at photon energies equal to the DM mass. Bluer lines are annihilation spectra with lower DM mass. Redder lines are spectra from larger DM mass. All Spectral models are sourced from the Heavy Dark Matter models [64].

1142 Figure 7.3 shows the median and $\pm 1\sigma$ maps used as input for DM annihilation studied by \mathcal{LS} .

1143 7.3.3 Source Selection and Annihilation Channels

1144 HAWC's sources for this multithreaded analysis include Coma Berenices, Draco, Segue 1, and

1145 Sextans \mathcal{LS} observes up to 43 sources in its publication, however the best fit profiles were not

1146 provided at the time this thesis was written. A full description of each source used in this analysis

1147 is found in Table 7.1.

1148 This analysis improves on chapter 6 in the following ways. Previously, the particle physics model

Name	Distance (kpc)	l, b ($^\circ$)	$\log_{10} J$ (\mathcal{LS} set) $\log_{10}(\text{GeV}^2\text{cm}^{-5}\text{sr})$
Coma Berenices	44	241.89, 83.61	$19.00^{+0.36}_{-0.35}$
Draco	76	86.37, 34.72	$18.83^{+0.12}_{-0.12}$
Segue I	23	220.48, 50.43	$19.12^{+0.49}_{-0.58}$
Sextans	86	243.50, 42.27	$17.73^{+0.13}_{-0.12}$

Table 7.1 Summary of the relevant properties of the dSphs used in the present work. Column 1 lists the dSphs. Columns 2 and 3 present their heliocentric distance and galactic coordinates, respectively. Columns 4 reports the J -factors of each source given from the \mathcal{LS} studies and estimated $\pm 1\sigma$ uncertainties. The values $\log_{10} J$ (\mathcal{LS} set) [65] correspond to the mean J -factor values for a source extension truncated at 0.5° .

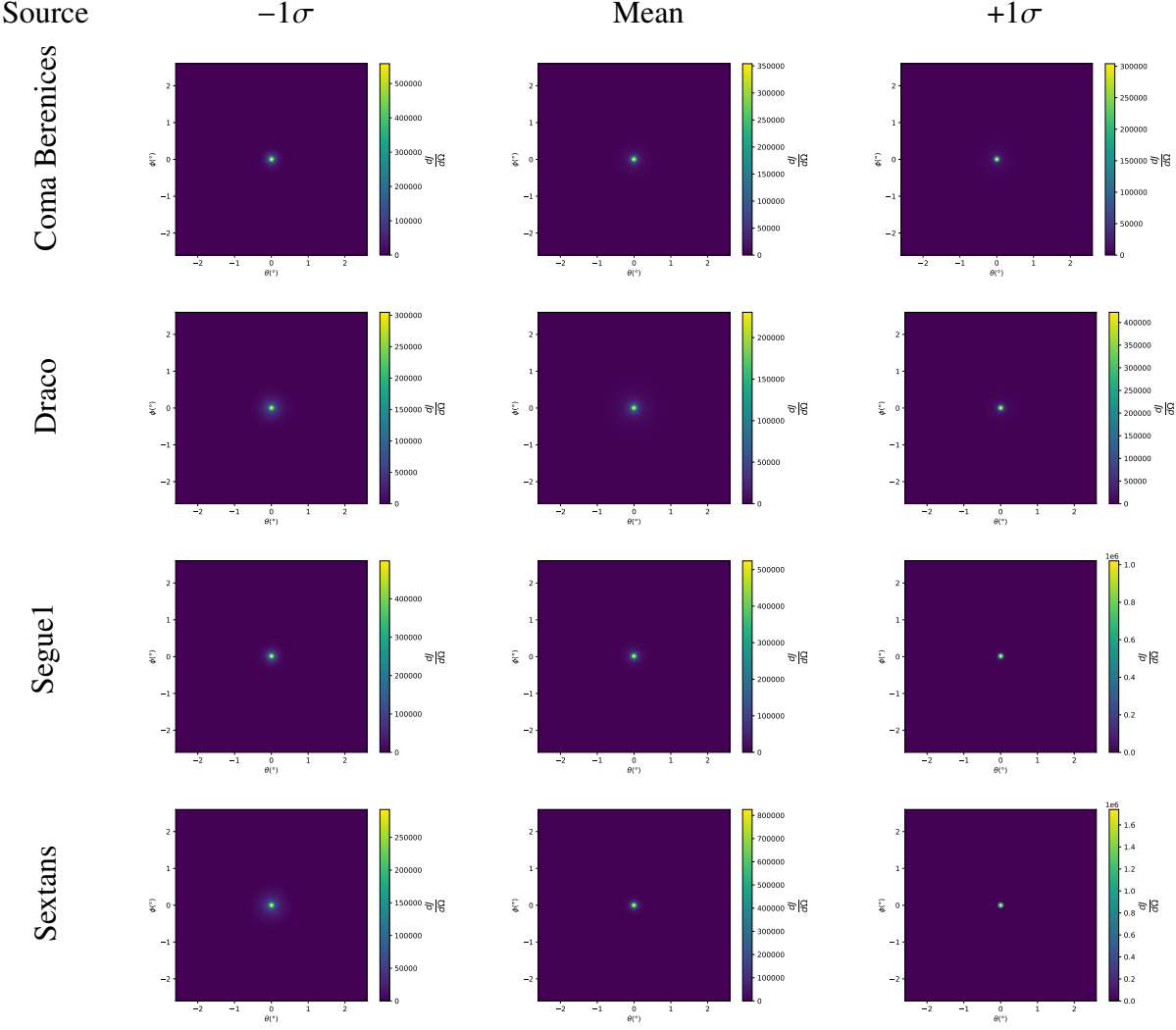


Figure 7.3 $\frac{dJ}{d\Omega}$ maps for Coma Berenices, Draco, Segue1, and Sextans. Columns are divided for the $\pm 1\sigma$ uncertainties in $dJ/d\Omega$ around the median value from \mathcal{LS} [65]. Origin is centered on the specific dwarf spheroidal galaxies (dSph). θ and ϕ axes are the angular separation from the center of the dwarf. Axes are drawn roughly according to the energy sensitivity of HAWC.

1149 used for gamma-ray spectra from DM annihilation was from the PPPC [44] which missed important
 1150 considerations relevant for the neutrino sector. HDM is used to account for this shortfall [64]. A
 1151 larger source catalog is used that uses a Navarro–Frenk–White (NFW) spatial DM distribution from
 1152 \mathcal{LS} [65]. Because NFW has fewer parameters than what is used for \mathcal{GS} , \mathcal{LS} is able to fit ultra-faint
 1153 dwarves, expanding the number of sources available for DM searches. Finally, the gamma-ray ray
 1154 dataset is much larger. The study performed here analyzes 2565 days of data compared to 1017
 1155 days analyzed in chapter 6.

1157 **HEAVY DARK MATTER ANNIHILATION SEARCH WITH ICECUBE'S NORTH SKY**
1158 **TRACK DATA**

CHAPTER 8

CHAPTER 9

NU DUCK

MULTI-EXPERIMENT SUPPLEMENTARY FIGURES

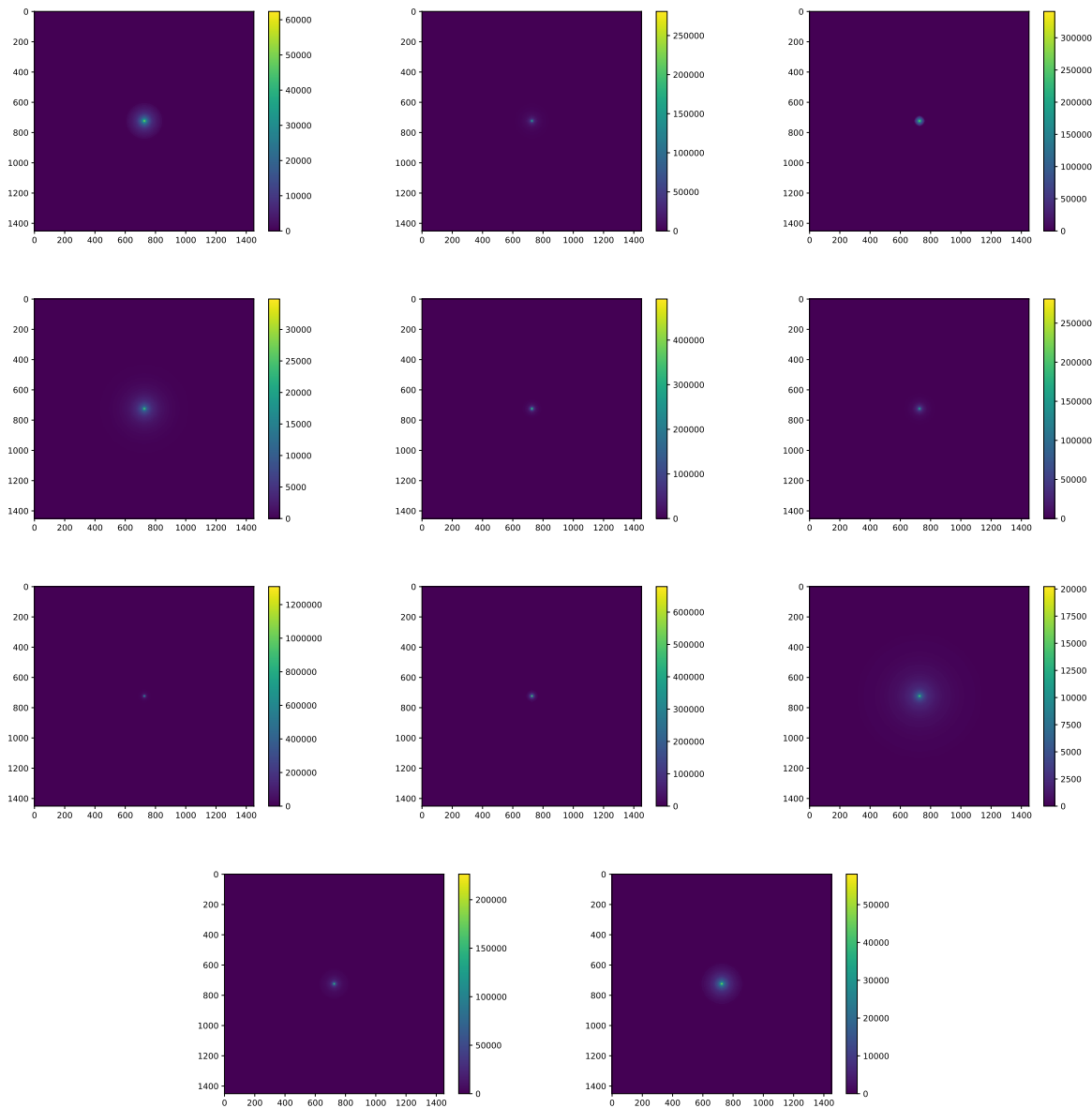


Figure A.1 Sister figure to Figure 6.3. Sources in the first row from left to right: Bootes I, Canes Venatici I, II. In second row: Draco, Hercules, Leo I. In the first row: Leo II, Leo IV, Sextans. In the final row: Ursa Major I, Ursa Major II.

APPENDIX B

1161

MULTITHREADING SUPPLEMENTARY FIGURES

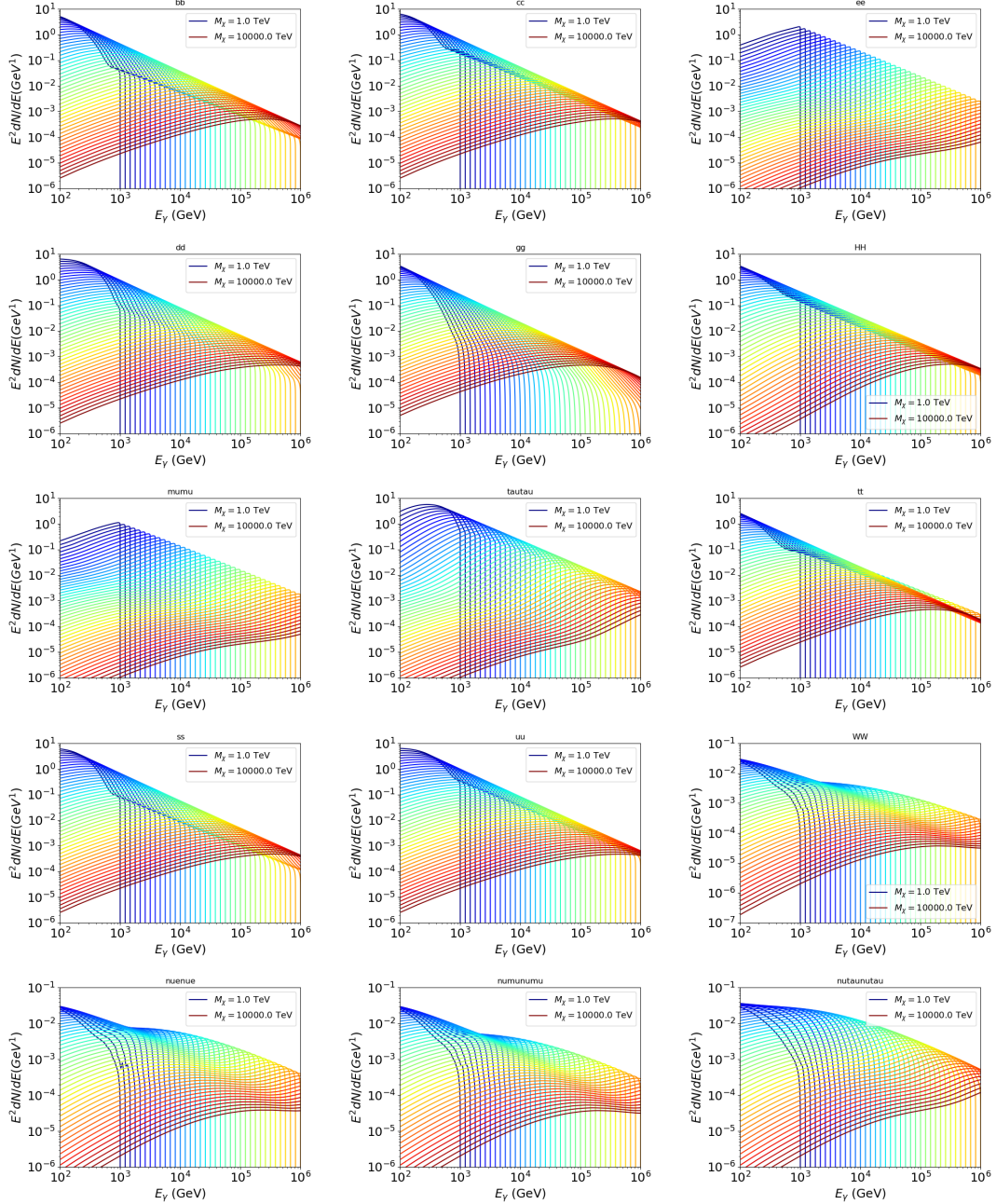


Figure B.1 Sister figure to Figure 7.2 for remaining SM primary annihilation channels studied for this thesis. These did not require any post generation smoothing and so are directly pulled from [64] with a binning scheme most helpful for a HAWC analysis.

BIBLIOGRAPHY

- 1163 [1] Anne M. Green. “Dark matter in astrophysics/cosmology”. In: *SciPost Phys. Lect.*
 1164 *Notes* (2022), p. 37. doi: [10.21468/SciPostPhysLectNotes.37](https://doi.org/10.21468/SciPostPhysLectNotes.37). URL: <https://scipost.org/10.21468/SciPostPhysLectNotes.37>.
- 1166 [2] Bing-Lin Young. “A survey of dark matter and related topics in cosmology”. In: *Frontiers*
 1167 *of Physics* 12 (Oct. 2016). doi: <https://doi.org/10.1007/s11467-016-0583-4>.
 1168 URL: <https://doi.org/10.1007/s11467-016-0583-4>.
- 1169 [3] Gianfranco Bertone, Dan Hooper, and Joseph Silk. “Particle dark matter: evidence,
 1170 candidates and constraints”. In: *Physics Reports* 405.5 (2005), pp. 279–390. ISSN:
 1171 0370-1573. doi: <https://doi.org/10.1016/j.physrep.2004.08.031>. URL:
 1172 <https://www.sciencedirect.com/science/article/pii/S0370157304003515>.
- 1173 [4] Gianfranco Bertone and Dan Hooper. “History of dark matter”. In: *Rev. Mod. Phys.*
 1174 90 (4 Aug. 2018), p. 045002. doi: [10.1103/RevModPhys.90.045002](https://doi.org/10.1103/RevModPhys.90.045002). URL: <https://link.aps.org/doi/10.1103/RevModPhys.90.045002>.
- 1176 [5] Fritz Zwicky. “The Redshift of Extragalactic Nebulae”. In: *Helvetica Physica Acta* 6.
 1177 (1933), pp. 110–127. doi: [10.5169/seals-110267](https://doi.org/10.5169/seals-110267).
- 1178 [6] Vera C. Rubin and Jr. Ford W. Kent. “Rotation of the Andromeda Nebula from a
 1179 Spectroscopic Survey of Emission Regions”. In: *ApJ* 159 (Feb. 1970), p. 379. doi:
 1180 [10.1086/150317](https://doi.org/10.1086/150317).
- 1181 [7] K. G. Begeman, A. H. Broeils, and R. H. Sanders. “Extended rotation curves of spiral galax-
 1182 ies: dark haloes and modified dynamics”. In: *Monthly Notices of the Royal Astronomical So-*
 1183 *ciety* 249.3 (Apr. 1991), pp. 523–537. ISSN: 0035-8711. doi: [10.1093/mnras/249.3.523](https://doi.org/10.1093/mnras/249.3.523).
 1184 eprint: <https://academic.oup.com/mnras/article-pdf/249/3/523/18160929/mnras249-0523.pdf>. URL: <https://doi.org/10.1093/mnras/249.3.523>.
- 1186 [8] *Different types of gravitational lenses*. website. Feb. 2004. URL: <https://esahubble.org/images/heic0404b/>.
- 1188 [9] Douglas Clowe et al. “A Direct Empirical Proof of the Existence of Dark Matter”. In: *apjl*
 1189 648.2 (Sept. 2006), pp. L109–L113. doi: [10.1086/508162](https://doi.org/10.1086/508162). arXiv: [astro-ph/0608407](https://arxiv.org/abs/astro-ph/0608407)
 1190 [[astro-ph](#)].
- 1191 [10] Planck Collaboration and N. et. al. Aghanim. “Planck 2018 results I. Overview and the
 1192 cosmological legacy of Planck”. In: *A&A* 641 (2020). doi: [10.1051/0004-6361/201833880](https://doi.org/10.1051/0004-6361/201833880). URL: <https://doi.org/10.1051/0004-6361/201833880>.
- 1194 [11] Wayne Hu. *Matter Density Animation*. web. 2024. URL: <http://background.uchicago.edu/~whu/animbut/anim2.html>.

- 1196 [12] Wenlong Yuan et al. “A First Look at Cepheids in a Type Ia Supernova Host with JWST”. in:
1197 *The Astrophysical Journal Letters* 940.1 (Nov. 2022). doi: [10.3847/2041-8213/ac9b27](https://doi.org/10.3847/2041-8213/ac9b27).
1198 URL: <https://dx.doi.org/10.3847/2041-8213/ac9b27>.
- 1199 [13] Wendy L. Freedman. “Measurements of the Hubble Constant: Tensions in Perspective”. In:
1200 *The Astrophysical Journal* 919.1 (Sept. 2021), p. 16. doi: [10.3847/1538-4357/ac0e95](https://doi.org/10.3847/1538-4357/ac0e95).
1201 URL: <https://dx.doi.org/10.3847/1538-4357/ac0e95>.
- 1202 [14] Jodi Cooley. “Dark Matter direct detection of classical WIMPs”. In: *SciPost Phys. Lect.
1203 Notes* (2022), p. 55. doi: [10.21468/SciPostPhysLectNotes.55](https://doi.org/10.21468/SciPostPhysLectNotes.55). URL: <https://scipost.org/10.21468/SciPostPhysLectNotes.55>.
- 1204
1205 [15] “Search for new phenomena in events with an energetic jet and missing transverse momentum
1206 in pp collisions at $\sqrt{s} = 13$ TeV with the ATLAS detector”. In: *Phys. Rev. D* 103
1207 (11 July 2021), p. 112006. doi: [10.1103/PhysRevD.103.112006](https://doi.org/10.1103/PhysRevD.103.112006). URL: <https://link.aps.org/doi/10.1103/PhysRevD.103.112006>.
- 1208
1209 [16] *Jetting into the dark side: a precision search for dark matter*. website. July 2020. URL:
1210 <https://atlas.cern/updates/briefing/precision-search-dark-matter>.
- 1211
1212 [17] Celine Armand et. al. “Combined dark matter searches towards dwarf spheroidal galaxies
1213 with Fermi-LAT, HAWC, H.E.S.S., MAGIC, and VERITAS”. in: *Proceedings of Science*.
Vol. 395. Mar. 2022. doi: <https://doi.org/10.22323/1.395.0528>.
- 1214
1215 [18] Tracy R. Slatyer. “Les Houches Lectures on Indirect Detection of Dark Matter”. In: *SciPost
1216 Phys. Lect. Notes* (2022), p. 53. doi: [10.21468/SciPostPhysLectNotes.53](https://doi.org/10.21468/SciPostPhysLectNotes.53). URL:
<https://scipost.org/10.21468/SciPostPhysLectNotes.53>.
- 1217
1218 [19] Christian W Bauer, Nicholas L. Rodd, and Bryan R. Webber. “Dark matter spectra from
1219 the electroweak to the Planck scale”. In: *Journal of High Energy Physics* 2021.1029-8479
(June 2021). doi: [https://doi.org/10.1007/JHEP06\(2021\)121](https://doi.org/10.1007/JHEP06(2021)121).
- 1220
1221 [20] Riccardo Catena and Piero Ullio. “A novel determination of the local dark matter density”.
In: *Journal of Cosmology and Astroparticle Physics* 2010.08 (Aug. 2010), p. 004. doi:
1222 [10.1088/1475-7516/2010/08/004](https://doi.org/10.1088/1475-7516/2010/08/004). URL: <https://dx.doi.org/10.1088/1475-7516/2010/08/004>.
- 1223
1224 [21] B. P. Abbott et al. “Observation of Gravitational Waves from a Binary Black Hole Merger”.
In: *Phys. Rev. Lett.* 116 (6 Feb. 2016), p. 061102. doi: [10.1103/PhysRevLett.116.061102](https://doi.org/10.1103/PhysRevLett.116.061102). URL: <https://link.aps.org/doi/10.1103/PhysRevLett.116.061102>.
- 1225
1226 [22] R. Abbasi et. al. “Observation of high-energy neutrinos from the Galactic plane”. In: *Science*
380.6652 (June 2023), pp. 1338–1343.
- 1227
1228 [23] NASA Goddard Space Flight Center. *Fermi’s 12-year view of the gamma-ray sky*. website.

- 1230 2022. URL: <https://svs.gsfc.nasa.gov/14090>.
- 1231 [24] Marco Cirelli et al. “PPPC 4 DM ID: a poor particle physicist cookbook for dark matter
1232 indirect detection”. In: *Journal of Cosmology and Astroparticle Physics* 2011.03 (Mar.
1233 2011), p. 051. doi: [10.1088/1475-7516/2011/03/051](https://doi.org/10.1088/1475-7516/2011/03/051). URL: <https://dx.doi.org/10.1088/1475-7516/2011/03/051>.
- 1235 [25] Javier Rico. “Gamma-Ray Dark Matter Searches in Milky Way Satellites—A Comparative
1236 Review of Data Analysis Methods and Current Results”. In: *Galaxies* 8.1 (Mar. 2020), p. 25.
1237 doi: [10.3390/galaxies8010025](https://doi.org/10.3390/galaxies8010025). arXiv: [2003.13482](https://arxiv.org/abs/2003.13482) [astro-ph.HE].
- 1238 [26] W. B. Atwood et al. “The Large Area Telescope on the Fermi Gamma-Ray Space Telescope
1239 Mission”. In: *apj* 697.2 (June 2009), pp. 1071–1102. doi: [10.1088/0004-637X/697/2/1071](https://doi.org/10.1088/0004-637X/697/2/1071). arXiv: [0902.1089](https://arxiv.org/abs/0902.1089) [astro-ph.IM].
- 1241 [27] M. Ackermann et al. “Searching for Dark Matter Annihilation from Milky Way Dwarf
1242 Spheroidal Galaxies with Six Years of Fermi Large Area Telescope Data”. In: *prl* 115.23,
1243 231301 (Dec. 2015), p. 231301. doi: [10.1103/PhysRevLett.115.231301](https://doi.org/10.1103/PhysRevLett.115.231301). arXiv:
1244 [1503.02641](https://arxiv.org/abs/1503.02641) [astro-ph.HE].
- 1245 [28] Mattia Di Mauro, Martin Stref, and Francesca Calore. “Investigating the effect of Milky
1246 Way dwarf spheroidal galaxies extension on dark matter searches with Fermi-LAT data”.
1247 In: *Phys. Rev. D* 106 (12 Dec. 2022), p. 123032. doi: [10.1103/PhysRevD.106.123032](https://doi.org/10.1103/PhysRevD.106.123032).
1248 URL: <https://link.aps.org/doi/10.1103/PhysRevD.106.123032>.
- 1249 [29] F. et al. Aharonian. “Observations of the Crab Nebula with H.E.S.S.”. In: *Astron. Astrophys.*
1250 457 (2006), pp. 899–915. doi: [10.1051/0004-6361:20065351](https://doi.org/10.1051/0004-6361:20065351). arXiv: [astro-ph/0607333](https://arxiv.org/abs/astro-ph/0607333).
- 1252 [30] J. Albert et al. “VHE γ -Ray Observation of the Crab Nebula and its Pulsar with the MAGIC
1253 Telescope”. In: *The Astrophysical Journal* 674.2 (Feb. 2008), p. 1037. doi: [10.1086/525270](https://doi.org/10.1086/525270). URL: <https://dx.doi.org/10.1086/525270>.
- 1255 [31] N. Park. “Performance of the VERITAS experiment”. In: *Proceedings, 34th International
1256 Cosmic Ray Conference (ICRC2015): The Hague, The Netherlands, July, 30th July - 6th
1257 August*. Vol. 34. 2015, p. 771. arXiv: [1508.07070](https://arxiv.org/abs/1508.07070) [astro-ph.IM].
- 1258 [32] A. Abramowski et al. “H.E.S.S. constraints on Dark Matter annihilations towards the Sculptor
1259 and Carina Dwarf Galaxies”. In: *Astropart. Phys.* 34 (2011), pp. 608–616. doi: [10.1016/j.astropartphys.2010.12.006](https://doi.org/10.1016/j.astropartphys.2010.12.006). arXiv: [1012.5602](https://arxiv.org/abs/1012.5602) [astro-ph.HE].
- 1261 [33] A. Abramowski et al. “Search for dark matter annihilation signatures in H.E.S.S. observations
1262 of Dwarf Spheroidal Galaxies”. In: *Phys. Rev. D* 90 (2014), p. 112012. doi: [10.1103/PhysRevD.90.112012](https://doi.org/10.1103/PhysRevD.90.112012). arXiv: [1410.2589](https://arxiv.org/abs/1410.2589) [astro-ph.HE].

- 1264 [34] H. Abdalla et al. “Searches for gamma-ray lines and ‘pure WIMP’ spectra from Dark
1265 Matter annihilations in dwarf galaxies with H.E.S.S”. in: *JCAP* 11 (2018), p. 037. doi:
1266 [10.1088/1475-7516/2018/11/037](https://doi.org/10.1088/1475-7516/2018/11/037). arXiv: [1810.00995 \[astro-ph.HE\]](https://arxiv.org/abs/1810.00995).
- 1267 [35] J. Aleksić et al. “Optimized dark matter searches in deep observations of Segue 1 with
1268 MAGIC”. in: *JCAP* 1402 (2014), p. 008. doi: [10.1088/1475-7516/2014/02/008](https://doi.org/10.1088/1475-7516/2014/02/008).
1269 arXiv: [1312.1535 \[hep-ph\]](https://arxiv.org/abs/1312.1535).
- 1270 [36] V.A. Acciari et al. “Combined searches for dark matter in dwarf spheroidal galaxies observed
1271 with the MAGIC telescopes, including new data from Coma Berenices and Draco”. In: *Physics of the Dark Universe* (2021), p. 100912. issn: 2212-6864. doi: <https://doi.org/10.1016/j.dark.2021.100912>. URL: <https://www.sciencedirect.com/science/article/pii/S2212686421001370>.
- 1275 [37] M. L. Ahnen et al. “Indirect dark matter searches in the dwarf satellite galaxy Ursa Major II
1276 with the MAGIC Telescopes”. In: *JCAP* 1803.03 (2018), p. 009. doi: [10.1088/1475-7516/2018/03/009](https://doi.org/10.1088/1475-7516/2018/03/009). arXiv: [1712.03095 \[astro-ph.HE\]](https://arxiv.org/abs/1712.03095).
- 1278 [38] S. et al. Archambault. “Dark matter constraints from a joint analysis of dwarf Spheroidal
1279 galaxy observations with VERITAS”. in: *prd* 95.8 (Apr. 2017). doi: [10.1103/PhysRevD.95.082001](https://doi.org/10.1103/PhysRevD.95.082001). arXiv: [1703.04937 \[astro-ph.HE\]](https://arxiv.org/abs/1703.04937).
- 1281 [39] Louise Oakes et al. “Combined Dark Matter searches towards dwarf spheroidal galaxies with
1282 Fermi-LAT, HAWC, HESS, MAGIC and VERITAS”. in: *Proceedings of Science*. 2019.
- 1283 [40] Celine Armand et al. on behalf of the Fermi-LAT, HAWC, HESS, MAGIC, VERITAS.
1284 “Combined Dark Matter searches towards dwarf spheroidal galaxies with Fermi-LAT,
1285 HAWC, HESS, MAGIC and VERITAS”. in: *Proceedings of Science*. 2021.
- 1286 [41] Daniel Kerszberg et al. on behalf of the Fermi-LAT, HAWC, HESS, MAGIC, and VER-
1287 TIAS collaborations. “Search for dark matter annihilation with a combined analysis of
1288 dwarf spheroidal galaxies from Fermi-LAT, HAWC, H.E.S.S., MAGIC and VERITAS”. in:
1289 *Proceedings of Science*. 2023.
- 1290 [42] A. U. Abeysekara et al. “Observation of the Crab Nebula with the HAWC Gamma-Ray
1291 Observatory”. In: *The Astrophysical Journal* 843.1 (June 2017), p. 39. doi: [10.3847/1538-4357/aa7555](https://doi.org/10.3847/1538-4357/aa7555). URL: <https://doi.org/10.3847/1538-4357/aa7555>.
- 1293 [43] Giacomo Vianello et al. *The Multi-Mission Maximum Likelihood framework (3ML)*. 2015.
1294 arXiv: [1507.08343 \[astro-ph.HE\]](https://arxiv.org/abs/1507.08343).
- 1295 [44] Marco Cirelli et al. “PPPC 4 DM ID: a poor particle physicist cookbook for dark matter
1296 indirect detection”. In: *Journal of Cosmology and Astroparticle Physics* 2011.03 (Mar.
1297 2011). issn: 1475-7516. doi: [10.1088/1475-7516/2011/03/051](https://doi.org/10.1088/1475-7516/2011/03/051). URL: <http://dx.doi.org/10.1088/1475-7516/2011/03/051>.

- 1299 [45] Alex Geringer-Sameth, Savvas M. Koushiappas, and Matthew Walker. “DWARF GALAXY
1300 ANNIHILATION AND DECAY EMISSION PROFILES FOR DARK MATTER EXPERI-
1301 MENTS”. in: *The Astrophysical Journal* 801.2 (Mar. 2015), p. 74. ISSN: 1538-4357. doi:
1302 [10.1088/0004-637X/801/2/74](https://doi.org/10.1088/0004-637X/801/2/74). URL: <http://dx.doi.org/10.1088/0004-637X/801/2/74>.
- 1304 [46] A. Albert et al. “Dark Matter Limits from Dwarf Spheroidal Galaxies with the HAWC
1305 Gamma-Ray Observatory”. In: *The Astrophysical Journal* 853.2 (Feb. 2018), p. 154. ISSN:
1306 1538-4357. doi: [10.3847/1538-4357/aaa6d8](https://doi.org/10.3847/1538-4357/aaa6d8). URL: <http://dx.doi.org/10.3847/1538-4357/aaa6d8>.
- 1308 [47] V. Bonnivard et al. “Spherical Jeans analysis for dark matter indirect detection in dwarf
1309 spheroidal galaxies - Impact of physical parameters and triaxiality”. In: *Mon. Not. Roy.
1310 Astron. Soc.* 446 (2015), pp. 3002–3021. doi: [10.1093/mnras/stu2296](https://doi.org/10.1093/mnras/stu2296). arXiv:
1311 [1407.7822 \[astro-ph.HE\]](https://arxiv.org/abs/1407.7822).
- 1312 [48] M. Ackermann et al. “Searching for Dark Matter Annihilation from Milky Way Dwarf
1313 Spheroidal Galaxies with Six Years of Fermi Large Area Telescope Data”. In: *prl* 115.23,
1314 231301 (Dec. 2015), p. 231301. doi: [10.1103/PhysRevLett.115.231301](https://doi.org/10.1103/PhysRevLett.115.231301). arXiv:
1315 [1503.02641 \[astro-ph.HE\]](https://arxiv.org/abs/1503.02641).
- 1316 [49] M. L. Ahnen et al. “Limits to Dark Matter Annihilation Cross-Section from a Combined
1317 Analysis of MAGIC and Fermi-LAT Observations of Dwarf Satellite Galaxies”. In: *JCAP*
1318 1602.02 (2016), p. 039. doi: [10.1088/1475-7516/2016/02/039](https://doi.org/10.1088/1475-7516/2016/02/039). arXiv: [1601.06590](https://arxiv.org/abs/1601.06590)
1319 [astro-ph.HE].
- 1320 [50] Javier Rico et al. *gLike: numerical maximization of heterogeneous joint
1321 likelihood functions of a common free parameter plus nuisance parameters*.
1322 <https://doi.org/10.5281/zenodo.4601451>. Version v0.09.03. Mar. 2021. doi: [10.5281/zenodo.4601451](https://doi.org/10.5281/zenodo.4601451). URL: <https://doi.org/10.5281/zenodo.4601451>.
- 1324 [51] Tjark Miener and Daniel Nieto. *LklCom: Combining likelihoods from different experiments*.
1325 <https://doi.org/10.5281/zenodo.4597500>. Version v0.5.3. Mar. 2021. doi: [10.5281/zenodo.4597500](https://doi.org/10.5281/zenodo.4597500). URL: <https://doi.org/10.5281/zenodo.4597500>.
- 1327 [52] T. Miener et al. “Open-source Analysis Tools for Multi-instrument Dark Matter Searches”.
1328 In: *arXiv e-prints*, arXiv:2112.01818 (Dec. 2021), arXiv:2112.01818. arXiv: [2112.01818](https://arxiv.org/abs/2112.01818)
1329 [astro-ph.IM].
- 1330 [53] Alex Geringer-Sameth and Matthew Koushiappas Savvas M. and Walker. “Dwarf galaxy
1331 annihilation and decay emission profiles for dark matter experiments”. In: *Astrophys.
1332 J.* 801.2 (2015), p. 74. doi: [10.1088/0004-637X/801/2/74](https://doi.org/10.1088/0004-637X/801/2/74). arXiv: [1408.0002](https://arxiv.org/abs/1408.0002)
1333 [astro-ph.CO].
- 1334 [54] Gianfranco Bertone, Dan Hooper, and Joseph Silk. “Particle dark matter: evidence, can-

- 1335 didates and constraints”. In: *Physics Reports* 405.5-6 (Jan. 2005), pp. 279–390. ISSN:
1336 0370-1573. doi: [10.1016/j.physrep.2004.08.031](https://doi.org/10.1016/j.physrep.2004.08.031). URL: <http://dx.doi.org/10.1016/j.physrep.2004.08.031>.
- 1338 [55] V. Bonnivard et al. “Dark matter annihilation and decay in dwarf spheroidal galaxies: The
1339 classical and ultrafaint dSphs”. In: *Mon. Not. Roy. Astron. Soc.* 453.1 (2015), pp. 849–867.
1340 doi: [10.1093/mnras/stv1601](https://doi.org/10.1093/mnras/stv1601). arXiv: [1504.02048 \[astro-ph.HE\]](https://arxiv.org/abs/1504.02048).
- 1341 [56] A. et al. Albert. “Searching for Dark Matter Annihilation in Recently Discovered Milky Way
1342 Satellites with Fermi-LAT”. in: *Astrophys. J.* 834.2 (2017), p. 110. doi: [10.3847/1538-4357/834/2/110](https://doi.org/10.3847/1538-4357/834/2/110). arXiv: [1611.03184 \[astro-ph.HE\]](https://arxiv.org/abs/1611.03184).
- 1344 [57] Mattia Di Mauro and Martin Wolfgang Winkler. “Multimessenger constraints on the dark
1345 matter interpretation of the Fermi-LAT Galactic Center excess”. In: *prd* 103.12, 123005
1346 (June 2021), p. 123005. doi: [10.1103/PhysRevD.103.123005](https://doi.org/10.1103/PhysRevD.103.123005). arXiv: [2101.11027 \[astro-ph.HE\]](https://arxiv.org/abs/2101.11027).
- 1348 [58] HongSheng Zhao. “Analytical models for galactic nuclei”. In: *Mon. Not. Roy. Astron. Soc.*
1349 278 (1996), pp. 488–496. doi: [10.1093/mnras/278.2.488](https://doi.org/10.1093/mnras/278.2.488). arXiv: [astro-ph/9509122 \[astro-ph\]](https://arxiv.org/abs/astro-ph/9509122).
- 1351 [59] H. C. Plummer. “On the Problem of Distribution in Globular Star Clusters: (Plate 8.)”
1352 In: *Monthly Notices of the Royal Astronomical Society* 71.5 (Mar. 1911), pp. 460–470.
1353 ISSN: 0035-8711. doi: [10.1093/mnras/71.5.460](https://doi.org/10.1093/mnras/71.5.460). eprint: <https://academic.oup.com/mnras/article-pdf/71/5/460/2937497/mnras71-0460.pdf>. URL:
1355 <https://doi.org/10.1093/mnras/71.5.460>.
- 1356 [60] Daniel R. Hunter. “Derivation of the anisotropy profile, constraints on the local velocity
1357 dispersion, and implications for direct detection”. In: *JCAP* 02 (2014), p. 023. doi:
1358 [10.1088/1475-7516/2014/02/023](https://doi.org/10.1088/1475-7516/2014/02/023). arXiv: [1311.0256 \[astro-ph.CO\]](https://arxiv.org/abs/1311.0256).
- 1359 [61] Barun Kumar Dhar and Liliya L. R. Williams. “Surface mass density of the Einasto family
1360 of dark matter haloes: are they Sersic-like?” In: *Mon. Not. Roy. Astron. Soc.* (2010). doi:
1361 [10.1111/j.1365-2966.2010.16446.x](https://doi.org/10.1111/j.1365-2966.2010.16446.x).
- 1362 [62] M. Baes and E. Van Hese. “Dynamical models with a general anisotropy profile”. In:
1363 *Astron. Astrophys.* 471 (2007), p. 419. doi: [10.1051/0004-6361:20077672](https://doi.org/10.1051/0004-6361:20077672). arXiv:
1364 [0705.4109 \[astro-ph\]](https://arxiv.org/abs/0705.4109).
- 1365 [63] Matthew G. Walker, Edward W. Olszewski, and Mario Mateo. “Bayesian analysis of re-
1366 solved stellar spectra: application to MMT/Hectochelle observations of the Draco dwarf
1367 spheroidal”. In: *mnras* 448.3 (Apr. 2015), pp. 2717–2732. doi: [10.1093/mnras/stv099](https://doi.org/10.1093/mnras/stv099).
1368 arXiv: [1503.02589 \[astro-ph.GA\]](https://arxiv.org/abs/1503.02589).
- 1369 [64] Nicholas L. Rodd et al. “Dark matter spectra from the electroweak to the Planck scale”. In:

- 1370 *J. High Energy Physics* 121.10.1007 (June 2021).
- 1371 [65] Pace, Andrew B and Strigari, Louis E. “Scaling relations for dark matter annihilation and
1372 decay profiles in dwarf spheroidal galaxies”. In: *Monthly Notices of the Royal Astronomical
1373 Society* 482.3 (Oct. 2018), pp. 3480–3496. ISSN: 0035-8711. doi: [10.1093/mnras/sty2839](https://doi.org/10.1093/mnras/sty2839).
- 1375 [66] Albert, A. et al. “Search for gamma-ray spectral lines from dark matter annihilation in
1376 dwarf galaxies with the High-Altitude Water Cherenkov observatory”. In: *Phys. Rev. D* 101 (10 May 2020), p. 103001. doi: [10.1103/PhysRevD.101.103001](https://doi.org/10.1103/PhysRevD.101.103001). URL:
1377 <https://link.aps.org/doi/10.1103/PhysRevD.101.103001>.
1378